**Exploring Nanoscale Energy Conversion and Biometabolism Using Custom Calorimetric Tools**

by

Rohith Mittapally

A dissertation submitted in partial fulfillment
of the requirements for the degree of
Doctorate of Philosophy
(Mechanical Engineering)
in the University of Michigan
2021

Doctoral Committee:

Professor Edgar Meyhofer, Co-Chair
Professor Pramod Reddy, Co-Chair
Professor Stephen R. Forrest
Professor Vikram Gavini

Rohith Mittapally

mrohith@umich.edu

ORCID iD:  0000-0002-0784-1369

## Dedication

To Mom, Dad and Sister.

**Acknowledgements**

It is needless to say that a PhD is not just ‘Ph’ilosophically ‘D’aunting, but physically and emotionally draining. I am happy to be one of those who made the choice to get a PhD for the love of science and curiosity. I have been fortunate to work in one of the best groups pushing the boundaries of human knowledge.

First of all, I am immensely grateful to my advisors Professors Pramod Reddy and Edgar Meyhofer for giving me the opportunity to learn and grow in their supervision. The curiosity-based work environment that they have fostered, helped me navigate these six years with a smile on my face. The time spent in this lab will remain one of the best phases of my life. At many stages of my career, they have taken an active role in advising, providing technical and moral support patiently. I wish to be the same mentor to those who may be at a similar stage in their lives as I was during my PhD.

Pramod’s conceptual understanding of everything always impressed me and is a thought process that I would want to master in my career. I would not be exaggerating to say that it is rare to meet a person who is extraordinarily smart and ambitious but also kind and humble at the same time. Everyone who knows Edgar knows that he knows everything about almost everything. I am always inspired by his continuing zeal to build things and even modify them according to evolving technology. I had the courage to try and test any new idea knowing that Edgar would come to the

rescue to fix it in case it fails. I am carrying a lot of learning gained over the years working with them both and wish to use it to do great things in the future.

Further, I would like to thank all the members in my lab whom I had interacted with and learnt from. I appreciate Dakotah Thompson for being a patient mentor, teaching me the basics of microfabrication and making me part of an amazing work. My acknowledgements would be empty without the mention of Sunghoon Hur, my friend and colleague for a greater part of my PhD. In his own words: 'We worked, cried, laughed and smiled together'. I would like to thank Anthony Fiorino and Linxiao Zhu for giving me the opportunity to be part of some incredible work. I thank Shen Yan and Yuxuan Luan for all the fun conversations outside of work and wish you all the best. I had a joyous time interacting with several others Charles Chang Jiang, Longji Cui, Ruijiao Miao, Andrej Lenert, Amin Reihani, Ju Won Lim, Audrey-Rose Guiterrez and the latest generation of students Ayan Majumder, Kanishka Panda and Jian Guan. I am grateful to all the seniors before me Seid Sadat, Bai Song and Yasher Ganjeh, who laid the foundations for most of my work.

I have been fortunate to work with Professor Stephen R. Forrest and learn from his experiences navigating the academia and the real-world. I like to thank Byungjun Lee, Dejiu Fan and Jihun Lim for helping with the fabrication of devices for near-field TPV work. I am also grateful to Professor Swathi Yadlapalli for the collaborations and discussions on my bio-calorimeter work. I would also like to thank Professor Vikram Gavini for being part of my dissertation committee. I have learnt a lot from observing his teaching and analysis style. A large part of my work away from lab involved fabricating devices at LNF. I am thankful to all the staff members for fostering a shared resource with state-of-the-art cleanroom facilities.

Finally, no level of appreciation can do justice to the sacrifices and the support of my family. My mom's unconditional love and my sister's encouragement kept me going through all this time. My work style, ethics and values have been shaped by my dad and my desire to impress him and be the son that he could be proud of. His teaching that is at the core of my decision-making is to work for the betterment of the humanity. I would like to thank my close friends Professor Raghu Bollapragada, for being a co-conspirator in doing something against what our families wanted us to do, Rajasekhar Pathlavath, for being there for me whenever I needed support and Isha Gupta with whom I had shared many professional and personal memories. My friends, especially RamPrasad Mohanan, Arsha and Abhilash have been a family far from home. I also had the fortune of being part of a large group of friends, travelling and exploring USA.

Living and making it through PhD, I have grown a sense of huge respect for everyone who makes this choice. My advice to all those who is still reading this: 'Hang in there! You will make it through the tunnel and come out shining'. Finally, in a Shakespearean style, while I regret all the lost quality time I could not spend with my family all these years, I could not have been happier with all the learning and joyous journey it had been. I will end with the cliché: 'Ph'inishe'D'.

## Table of Contents

## List of Figures

## Abstract

Radiative heat transfer (RHT) between two bodies separated by gaps larger than the thermal wavelength (10 μm at 300 K) occurs through modes that are propagating across the medium separating them, where the total RHT between them is bound by the blackbody limit. RHT beyond this limit is possible with contributions from surface modes, such as evanescent modes or surface phonon/plasmon polaritons. The principal goal of this thesis is to study emerging questions related to radiative heat transport in nanoscale gaps with implications on thermophotovoltaic power generation, thermal management of electronics and calorimetric techniques.

One important question in RHT is what the fundamental limits to near-field enhancements mediated by surface polaritons may be. Recent theoretical studies predicted materials with potential 5-fold enhancement over that of $SiO_2$, a state-of-the-art polar material for RHT. By leveraging high-resolution, micro-fabricated calorimeters in a custom-built nanopositioner, I show in chapter 2 of this thesis that RHT rates up to 3-times larger than $SiO_2$ can be obtained from $MgF_2$ and $Al_2O_3$ that have stronger phonon-polariton resonances than $SiO_2$. This represents the first experimental demonstration of enhanced RHT beyond that of $SiO_2$ using dielectric materials and thus, should enable future studies with potential enhancements up to the theoretical limit.

Next, in chapter 3 of this thesis I describe how near-field effects can be employed to achieve novel heat to electricity conversion technologies. Specifically, I explore how thermophotovoltaic technologies—where a hot emitter and a PV cell are employed to convert heat

to electricity—can be enhanced by employing near-field effects. I explored this possibility by developing doped-Si microdevices with an integrated platinum heater that could be heated to 400$^{o}$ C. By placing this hot object at a few tens of nanometers away from a commercial photodiode, we demonstrated—for the first time—that ~ 40-times larger power outputs as compared to the far-field can be obtained. Next, I describe how this previous work was extended to explore how the performance of a near-field TPV system can be further enhanced in terms of the power density and efficiency. In order to achieve this, I fabricated silicon microdevices that can endure temperatures up to ~1000 $^{o}$ C. Then, by leveraging the nanopositioner, we placed the silicon heater at known distances away from a thin-film InGaAs PV cell. When the distance was reduced to 100 nm, the total system demonstrated a record-high efficiency of ~6.7% at a power density of 5000 W/m$^2$. Additional improvements can enable several-fold gains in the performance and pave the way for realization of practical devices.

Finally, I describe in chapter 4 how I built a calorimetric tool with 270 pW heat resolution based on calorimetric techniques developed in my RHT studies. This was accomplished by minimizing the thermal conductance of a commercial glass capillary tube down to 27 μW/K and improving the thermometry to an unprecedented 10 μK resolution. Using this tool, we measured metabolic heat outputs from wild-type *C. elegans*, a biological model organism. Our measurements on *daf-2*, a variant with an increased lifespan, reveal interesting metabolic shifts as compared to wild-type variant. Thus, we demonstrated for the first time that metabolic rate measurements on living systems can be performed at sub-nanowatt resolution in real time with 270 pW resolution.

# Chapter 1 Introduction

## 1.1 Background

Heat is a flow of energy between two objects at different temperatures. Heat transfer occurs via conduction through energy carriers such as electrons, phonons etc., and convection that involves the flow of matter. The third form, radiation, is a form of heat transport mediated by photons that does not require any intervening material between the two systems and is a central focus of this work. To elaborate, two bodies at different temperatures interact through radiation, even in vacuum. In fact, radiative heat transfer plays a central role in numerous phenomena including global warming, photovoltaic energy conversion, radiative cooling to name a few. Thus, exploring and understanding radiative heat transfer (RHT) is essential for understanding both naturally occurring phenomena and for developing new technologies. In this thesis I have investigated thermal radiation in nanoscale gaps, called near-field radiative heat transfer, which I introduce below.

### *1.1.1 Near-field radiative heat transfer*

Radiation emitted by a hot body into its surroundings can be related to microscopic thermal oscillations of charges inside a body. Early descriptions of radiation from bodies involved the concept of a blackbody with the following properties[1]:

1) A blackbody absorbs all the electromagnetic radiation incident on its surface regardless of wavelength and direction.

2) For a prescribed temperature and wavelength, no other object can emit or absorb more radiation than a blackbody.
3) The intensity of the emitted radiation from a blackbody is independent of direction, implying that the blackbody is a diffuse emitter.

A blackbody, for theoretical purposes, was hypothesized as an isothermal cavity with a small hole. Any ray that enters the cavity undergoes multiple reflections and absorptions, eventually getting completely absorbed before being able to exit the cavity. The spectral intensity of blackbody radiation, i.e. radiation emanating from such a cavity, is described by Planck's law[2]:

$$E_{\nu,b}(\nu,T) = \frac{8\pi}{c^3}\frac{h\nu^3}{\exp\left(\frac{h\nu}{k_B T}\right)-1} \tag{1-1}$$

where $E_{\nu,b}(\nu,T)$ is the intensity of blackbody radiation per unit frequency $\nu$, $c$ is the speed of light, $h$ is the Planck's constant, $T$ is the temperature of the body and $k_B$ is the Boltzmann constant. This distribution has a maximum at a prescribed temperature, which is defined by the Wien's law as $\lambda_{max}T = 2898\ \mu m.K$, where $\lambda_{max}$ is the wavelength at which the spectral intensity peaks for a given temperature $T$. At room temperature, this maximum wavelength or thermal wavelength is 10 μm. Integrating the blackbody emissive power over all the frequencies results in the Stefan-Boltzmann law. The RHT between two objects at different temperatures is constrained by the blackbody limit derived from the Stefan-Boltzmann law[1].

In his seminal work[2], Planck acknowledged the limitations of his approach which cannot explain the thermal radiation when the characteristic dimensions of the involved objects are comparable to or much less than the thermal wavelength. Specifically, when the gap size is less than the thermal wavelength, the objects are said to be in the near-field of each other and Planck's

theory, which was developed for objects that are much farther away than the thermal wavelength (i.e. objects in the far-field of each other), cannot be applied. At these gap sizes, the ray picture of light is no longer valid and the framework of fluctuational electrodynamics (FED) was developed by Rytov et al.[3] and Polder and Van Hove[4], where the thermal radiation or heat transfer between objects is considered to result from thermal fluctuations in the material. The correlation function for these thermal fluctuations are based on fluctuation-dissipation theorem[5, 6]. The theoretical predictions based on these theoretical developments spearheaded the scientific exploration of near-field RHT.

Initial attempts to validate this theory (FED) were performed by Hargreaves[7] in 1969, where RHT between metallic parallel plates was measured down to few micrometers, and by Domoto et al.[8] in 1970 between metallic plates at liquid helium temperature. While these studies indicated enhanced RHT at micro-scale gaps, the true potential of near-field RHT was only realized in early 2000s, where several experiments[9-15] were performed in a sphere-plate configuration, owing to its simplicity in comparison with extended plate-plate configuration, and showed RHT enhancements at nanometric distances. A limitation to this approach is the use of proximity approximations to discretize the curved surfaces as planes to delineate the near-field signal from a large background noise. A clear demonstration of orders of magnitude enhancement in a plate-plate configuration down to tens of nanometers was only possible in the recent decade, aided by development of micro-devices, precise calorimetric techniques and precise alignment between the devices[16-24], which enabled the probing of near-field RHT between planar dielectric surfaces made of silica ($SiO_2$) that support surface phonon polaritons (SPhPs) and lead to large enhancement sin heat transfer. A more detailed and comprehensive review of the field can be found in the reviews[25-30].

These latest experiments in near-field RHT further boosted interest in the field, both theoretically and experimentally. However, as pointed out above, most of the recent experiments have been performed between $SiO_2$ and $SiO_2$ plates [19, 20, 31] and represent the system in which the largest enhancements of heat transfer have been experimentally observed. Other material systems explored were SiC[32, 33] that exploit the SPhPs, and doped-Si[22], metals[20, 33-35] that utilize surface plasmon polaritons (SPPs) but featured smaller heat transfer rates than $SiO_2$ surfaces. Therefore, a key question that is of fundamental interest is to understand the limits to enhancements in RHT that can be achieved. Past studies [36-38] have tried to address the question of achieving heat transfer rates larger than $SiO_2$ by optimizing the material parameters using Drude and Drude-Lorentz permittivity functions. In fact, a recent study[39] identified critical material properties to maximize RHT and predicted real bulk materials that can provide 5× higher RHT than that of $SiO_2$. They also predicted a theoretical maximum of 10× higher RHT as compared to that of $SiO_2$. While these studies focused on bulk materials, other studies explored RHT enhancements between metasurfaces[40-43], thin-films or multilayered structures[44-46]. In fact, a study[42] based on structuring doped-Si surfaces predicted wide range tuning of RHT and an enhancement of 3-times higher than that of $SiO_2$.

### *1.1.2 Near-field thermophotovoltaic energy conversion*

About 60% of the total energy generated in US, is wasted as heat to the environment due to inefficiencies at intermediate steps from raw source of energy to the final use. Global climate change necessitates (technological) solutions to tackle global warming. One essential step is to improve the efficiencies at every level of the energy conversion. Thus, it is important to convert this otherwise wasted heat into useful electricity. Thermophotovoltaic (TPV) energy conversion is

one such viable alternative that can handle different sources of energy without any moving parts and provides a portable and noiseless operation.

The history of TPV power generation dates back to 1960s, when a TPV[47] system was first conceptualized as an alternative to thermoelectric and thermionic energy conversion devices. The 1970s energy crisis led to an interest in non-renewable energy technologies, specifically solar power generation. Research in TPV slowed down in 1980s, but few researchers continued to work on developing IR band-gap cells using InGaAs[48]. Since the early 1990s, research driven by NASA and DARPA enabled development of different TPV systems: radio-isotope powered TPV[49], fossil fuel-powered TPV using GaSb cells[50], TPV for waste heat conversion[51] etc.

A typical TPV system consists of a thermal emitter and a photovoltaic (PV) cell for converting the energy of the emitted photons into electricity. Several research efforts tried to improve the overall efficiency by engineering the spectral transfer either through an intermediate spectral control device or by structuring the devices. In 2004, Wernsman *et al.*[51] reported 23.6% thermal-to-electricity conversion using a SiC emitter heated to 1039° C and an InGaAs-based monolithic interconnected module. This record-high efficiency was recently beaten by employing a back-surface reflector using a thin InGaAs film[52] leading to an efficiency of 29.1% at 1027° C. Fan et al.[53] developed air-gap thin-film InGaAs cells such that the sub-band gap photons are reflected due to total internal reflection. This innovation led to the current highest reported TPV efficiency[53] of 31.3% at 1182° C.

For TPV technology to compete with other solid-state technologies such as thermoelectric energy conversion, performance enhancements, especially in the power density, are essential. But, the total power density attainable from a hot body at a given temperature is limited by the blackbody radiation in the far-field. This can be overcome by reducing the gap size to tens of

nanometers. Pan et al.[54] showed that up to $n^2$ enhancement in the total spectral transfer can be obtained, where $n$ is the minimum of the refractive indices of the emitter and the PV cell, by reducing the gap size between the emitter and the PV cell. The potential of near-field TPV spurred a plethora of theoretical studies[55-63] that predicted large efficiencies and power densities. Zhao et al.[62] considered an ITO-based emitter at 900 K matched with an InAs PV cell and predicted an efficiency of 40 % at a power density of 110 kW/m$^2$. Papadakis et al.[63] considered broadening of the spectral transfer in the same system instead of a narrow-band transfer and predicted a conversion efficiency of 50% at 1300 K.

In early 2000s, DiMatteo et al.[64] showed a 5-fold increase in photocurrent generation in an InAs cell placed close to a silicon emitter. A clear and robust validation of this enhancement was shown recently by our group[65] in 2018. In this study, we used a heated micro-fabricated cantilever and placed it at 60 nm away from a commercial PV cell and demonstrated 40-fold enhancement in the power output. Subsequently, Inoue et al.[66] fabricated a device using Si and InGaAs PV cells and demonstrated power density of 120 W/m$^2$ with an efficiency of <0.98% at 1050 K. Bhatt et al.[67] reported an integrated platform using Si emitter and a Ge PV cell that enabled power outputs of 12.5 mW/m$^2$. All these demonstrations further strengthened the potential of near-field TPV and led to exploration of near-field TPV systems with improved performance.

In this thesis, I described in chapter 3 my recent work demonstrating a TPV system in the near-field using a Si emitter heated to 1300 K and a thin-film InGaAs PV cell at 300 K[68]. The power generated at a gap size of 100 nm was 5 kW/m$^2$ at an efficiency of 6.7%. Simultaneously, two other works also reported improved performance of near-field TPV systems. Lucchesi et al.[69] probed TPV enhancement in a sphere-plate configuration and demonstrated power densities of 7.5 kW/m$^2$ at an efficiency of 14%. This high efficiency was achieved by cooling the low band-

gap PV cell to liquid nitrogen temperature, thus reducing the dark current. Inoue et al.[70] also demonstrated an integrated TPV system with a power density of 2 $kW/m^2$ with an efficiency of 5.2% at 1162 K.

### 1.2 Structure of this dissertation

A major goal of my research involved exploring near-field radiative heat transfer. The results from this work are covered in chapters 2 & 3. The near-field radiative energy transfer is dominated either by evanescent waves or surface phonon/plasmon polaritons that are present on the interface between a material and vacuum. Chapter 2 deals with SPhP mediated enhancement in the near-field in the mid to far-infrared wavelength range: 8-30 μm. Chapter 3 deals with extracting enhanced electrical power output mediated by evanescent wave tunneling between a hot emitter and a cold photovoltaic cell. The useful energy extraction occurs above the band-gap of the photovoltaic cell, which is in the near-infrared range of < 3 μm. In chapter 4, I report my efforts in building a sub-nanowatt resolution calorimeter for metabolic heat rate measurements on small living systems. Finally, in chapter 5, I summarize the work achieved in this thesis and provide an outlook on the future work.

In chapter 2, I explore the limits to near-field RHT mediated by surface-phonon polaritons. I will describe experiments on polaritonic materials with near-field RHT enhancements exceeding that of a $SiO_2$-$SiO_2$ system. Specifically, I demonstrate that the polaritonic resonances in $MgF_2$ and $Al_2O_3$ can readily enhance RHT by 3 and 2-fold as compared to that of $SiO_2$. To systematically demonstrate this, I employed high-resolution calorimetric devices in a custom-built nanopositioner (as discussed in chapter 2) and carefully reduced the gap size from 8 μm down to 40 nm. By making such near-field measurements on devices coated with $MgF_2$ and $Al_2O_3$, I have demonstrated that the RHT can be enhanced up to 300-fold as compared to silicon devices and 3-

fold when compared to $SiO_2$. This study represents the first experimental verification of wide variety of polaritonic materials with potential RHT enhancements.

In chapter 3, I will describe the efforts to understand if near-field enhancement is possible in thermophotovoltaic power generation. In specific, I will start by describing the doped-Si microdevices with an integrated platinum heater that could be heated to ~700 K. By positioning this hot body close to a commercial photo-diode with a band-gap of ~0.303 eV, we were able to show that the electrical power output from the PV cell increases 40-fold by reducing the gap size from 10 μm to 60 nm. Subsequently, I will detail the devices and experimental techniques employed to demonstrate a near-field TPV device with improved power density and efficiency. I will explain the next generation of devices that are integrated with a doped-Si resistor allowing it be heated to 1300 K. I will then describe the experimental procedure employed to systematically parallelize and control the gap size between the devices with nanometric precision. Further, the power density and the efficiency as a function of temperatures and gap sizes are presented. The performance of the PV cell is compared with theoretical expectations in terms of the short-circuit current and open-circuit voltage. Finally, the physical reasons for this enhancement will be discussed, followed by a concluding section.

In chapter 4, I will discuss the development of a 270-pW resolution bio-calorimeter, built from commercially available components. I will describe how we monitored metabolic heat rates of individual *C. elegans* as a function of their age. Further, the effect of daf-2 mutation – a mutation that doubles the lifespan of *C.elegans* – on the metabolic heat rate is carefully studied. This study represents the highest reported heat resolution employed for measurement of metabolic heat rates from individual *C.elegans*. The techniques developed could enable further enhanced heat

resolutions with implications in exciting future metabolic studies on individual brown fat cells, cancer cells etc.

Finally, in chapter 5, I will summarize the work described in chapters 2,3 &4. Further, I will describe future work and strategies to further improve the systems discussed in this thesis and provide a broader outlook on each topic.

# Chapter 2 Enhanced Radiative Heat Transfer Using Polar Dielectric Materials in the Near-field

## 2.1 Abstract

Near-field radiative heat transfer that arises between objects separated by nanoscale gaps, i.e. gaps smaller than the thermal wavelength, can lead to dramatic enhancements in heat transfer rates compared to the far-field due to contributions from evanescent and surface modes. Recent experiments have provided first insights into the significant enhancement in radiative heat transfer that is possible in the near-field. In fact, recent studies using silica ($SiO_2$) surfaces which support surface phonon polaritons have shown over two orders of magnitude enhancement in radiative heat transfer compared to the far-field. However, so far experimental efforts to obtain near-field heat transfer rates exceeding that of $SiO_2$ have not been successful. Here, we experimentally demonstrate that heat transfer between plane-parallel surfaces of polaritonic materials like $MgF_2$ and $Al_2O_3$ can exceed that between $SiO_2$ surfaces by 2.5 times and 1.5 times, respectively. We also systematically vary the gap sizes between the parallel-plates and show that these larger radiative heat fluxes occur over a large range of gap sizes. Further, we theoretically analyze our systems and mechanistically explain the source of the observed enhancement. Finally, we discuss other materials that can lead to heat fluxes above that of $SiO_2$. The insights and materials discussed in this study should take us closer to understanding the ultimate limits to near-field based enhancement of heat transfer with potential applications in near-field thermal management, spectroscopy and thermophotovoltaics.

## 2.2 Introduction

Thermal radiative heat transfer (RHT) in the near-field has attracted significant interest due to its potential applications in thermo-photovoltaics[67-69, 71], thermal management[24, 72-74], spectroscopy[75], etc. RHT between two plates in the far-field, i.e. separated by gaps larger than the thermal wavelength has contributions only from the propagating waves and is bound by the blackbody limit[2]. In the near-field (NF), large enhancements in RHT can be obtained due to tunneling of evanescent waves or by coupling of surface phonon/plasmon polaritons (SPhP/SPP) on the surface (Fig. 2.1a). At the interface between vacuum and a material whose dielectric function is $\varepsilon(\omega)$, surface waves with parallel wavevector $k$ satisfying the condition $|\sqrt{\varepsilon}|\omega/c > k > \omega/c$, are evanescent in the vacuum and are propagating in the material while surface polaritons with exponentially decaying amplitude in both the vacuum and the dielectric material occur when $\mathrm{Re}(\varepsilon) = -1$. Surface polariton mediated RHT has progressively increasing contributions from large wavevectors, $k \gg |\sqrt{\varepsilon}|\omega/c$, as the gap size is reduced resulting in significantly enhanced heat transfer rates as has been observed in recent experiments with $SiO_2$ surfaces. Thus, it is of fundamental importance to explore limits to the RHT based on these surface resonances. Studies in the past[36-38] have tried to explore these limits by optimizing the parameters of the dielectric function using Drude and Drude-Lorentz permittivity functions that describe most materials. Quite recently, another study[39] identified critical material properties to maximize RHT predicted that bulk materials that can provide 5 fold higher RHT than $SiO_2$. While these studies focused on bulk materials, other studies explored RHT enhancements between metasurfaces[40-43], thin-films or multilayered structures[44-46]. In fact, a study[42] based on structuring doped-Si surfaces predicted wide range tuning of RHT and an enhancement that is 3 times higher than that of $SiO_2$.

Experimental validations of these predictions have been elusive due to challenging nano-fabrication requirements and stringent requirements on flatness and alignment between the devices at nanoscale gaps. In fact, the pioneering experiments in NFRHT have been limited to material systems involving bulk materials such as $SiO_2$ [19, 20, 31], SiC[32, 33] that exploit the SPhPs, and doped-Si[22], metals[20, 33-35] that utilize the SPPs. Among the experiments involving these material systems, the largest radiative heat conductance ($h_{RHT}$) has been for $SiO_2$, owing to its phonon resonance at ~10 μm. Thus, it is important to explore practical materials that could boost RHT beyond that of $SiO_2$. Here, we describe two such materials with interesting RHT enhancements that were rather unexplored, both experimentally and theoretically. Specifically, we show that dielectric materials such as magnesium fluoride ($MgF_2$) and aluminum oxide ($Al_2O_3$) can readily provide RHT enhancements of up to 2.5 times higher than that of $SiO_2$.

### 2.3 Devices and experimentation

In order to explore the NFRHT for different materials in the plane-plane configuration, we employed high-resolution and stiff calorimetric devices[24, 71, 72] and a custom-built nanopositioner[76] that allowed precise alignment and positioning of plates down to few tens of nanometers. The microdevices feature an 80-μm diameter circular mesa that extends 15 μm from rest of the device (Fig. 2.1b). The thin-film platinum line patterned in a serpentine pattern on the suspended island is used in a modulated thermometry scheme[77] resulting in a temperature resolution of ~50 μK. The island is suspended from the substrate by two thick beams (40 μm thick) resulting in a thermal conductance $G_{dev}$ of ~250 μW/K and leading to a heat flux resolution of ~2.5 $W/m^2$ (heat resolution normalized by the area of the mesa). A 1 μm-thick $SiO_2$ layer provides the electrical isolation between the platinum thermometer and the mesa, thus avoiding undesirable capacitive forces in the NF. The schematic in Fig. 2.1c shows the different layers of the micro-

fabricated emitter structure. The as-fabricated mesa surface is extremely flat and smooth with an RMS roughness of <1 nm (Fig. 2.1d). A polar dielectric of a known thickness is deposited on these microdevices using various deposition techniques. The RMS roughness of the deposited surface is ~3-5 nm and few particles ~20 nm in size were observed on the dielectric films (Fig. 2.1d). The cold receiver is a pristine large area (1 cm×cm) silicon substrate (Fig. 2.1c) coated with the corresponding dielectric ($MgF_2/Al_2O_3$) of suitable thickness (85/195 nm).

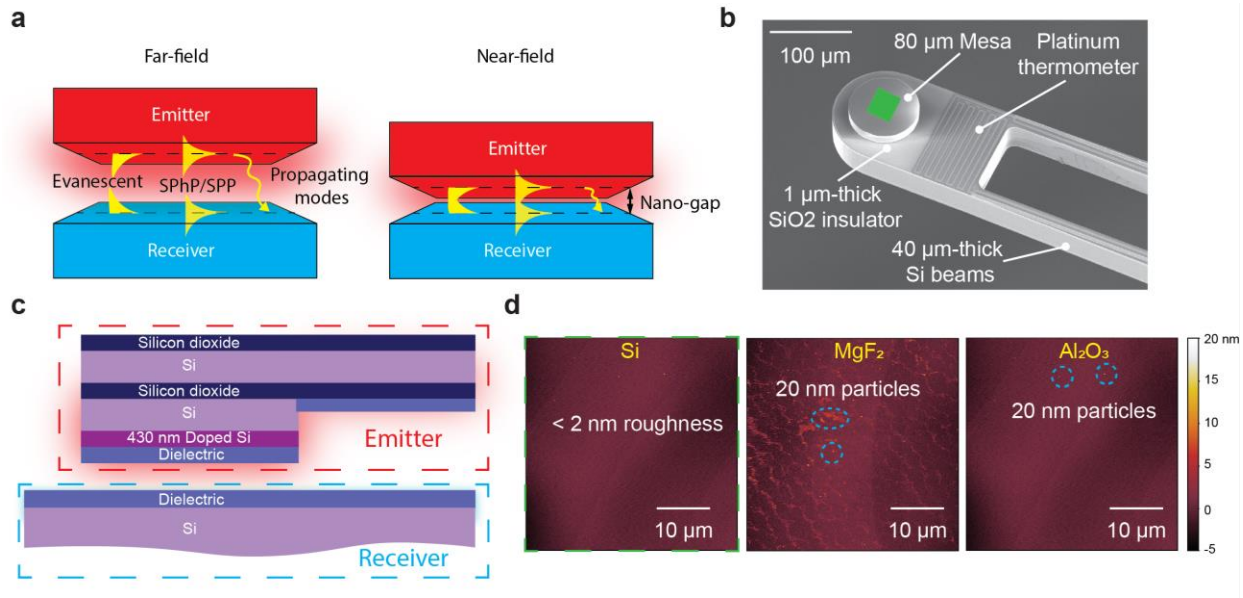


*Figure 2.1 Description of the devices.*

*(a) Schematic illustration of the different modes contributing to radiative heat transfer (RHT) between a hot emitter and a cold receiver (not drawn to scale). In the far-field, only the propagating modes lead to the RHT while in the near-field, evanescent waves and surface modes such as surface phonon/plasmon polaritons (SPhP/SPP) contribute to large RHT. (b) Scanning electron micrograph of the micro-fabricated calorimeter depicting the flat and smooth mesa and the island suspended by two thick silicon beams. The platinum thermometer, electrically isolated from the mesa acts as a heater and a thermometer. (c) Schematic of the emitter and the receiver employed in this study, showing the different layers with the corresponding materials. (d) Atomic force microscopy scans of the mesa surface. The first panel shows the scan on an as-fabricated mesa (40 × 40 μm2 area marked as green region in Fig. 2.1b), indicating RMS roughness < 2nm. The second panel shows the scans on a mesa surface coated with 85 nm-thick $MgF_2$ films. While the RMS roughness is < 5nm, few particles 20 nm in size are found. Similarly, the scans on $Al_2O_3$ coated device revealed few particles of ~20 nm size.*

Next, we describe the experimental approach followed in a typical RHT measurement in our setup. The emitter and the receiver devices coated with a dielectric, for example, $MgF_2$ (thickness of 85 nm), are assembled and precisely aligned in the nanopositioner. Next, the whole

assembly is maintained at a high vacuum of ~$5\times10^{-7}$ Torr, to minimize the contribution of convective heat transfer to the total RHT. An AC signal $I_{AC}$ = 70 μA is passed through the platinum thermometer to monitor the resistance change (TCR of Pt = $1.85\times10^{-3}$). The voltage change ($V_{meas}$) at this frequency is monitored via a lock-in detection scheme resulting in measurement of temperature changes in the mesa ($\Delta T_{NF}$). A suitably chosen DC current $I_{DC}$ is superimposed on $I_{AC}$ for heating the mesa to $T_{ref} + \Delta T_{ref}$, where $T_{ref}$ is the temperature of the substrate and the receiver (both at ~300 K). The gap size between the devices is maintained with a 2 nm resolution using a feedback-controlled piezoelectric actuator (Fig. 2.2a) that drives the receiver. Figure 2.2c shows the real-time data acquired as the gap size is systematically reduced from ~8 μm to 40 nm before contact is made. The emitter starts cooling down with reducing gap size due to the increasing radiative thermal conductance. The temperature signal remains relatively constant between gap sizes of 8 μm and 500 nm, whereas, large changes in the temperature signal are observed at smaller gaps that scale approximately as $1/d^2$, indicating a NF effect. In order to establish contact between the devices, we employ an optical detection scheme where a red laser is focused on the backside of the emitter and the reflected light is collected in a split photodiode. A small sinusoidal AC voltage at 3 kHz is applied to the piezoactuator causing the receiver to oscillate at an amplitude of ~2 nm. A sudden change in the detected optical signal unambigiously signals the formation of a contact between the emitter and the receiver as the emitter begins to oscillate at this frequency. This is also corroborated by a concurrent sudden change in the temperature signal.

The thermal resistance network with the corresponding thermal conductances and temperatures, is shown in Fig. 2.2b. The current $I_{DC}$ flowing through the platinum resistor results in a heat input, $Q_{in}$ which remains constant throughout the measurement. In far-field, $Q_{in} = Q_{FF} + G_{dev} \times (T_{em,i} - T_{ref})$, where $Q_{FF}$ is a far-field RHT component. As the gap size is reduced, emitter

temperature reduces by $\Delta T_{NF}$ to $T_{em,f}$. Thus, the gap-dependent heat flux change $Q_{NF}$ corresponding to this temperature change $\Delta T_{NF}$ is given by $Q_{NF} = G_{dev} \times \Delta T_{NF}$. The total radiative heat flux is then calculated as the sum of the measured heat change ($Q_{NF}$) and a calculated far-field heat transfer component $Q_{FF}$ which has contributions from the 'mesa' and the 'per' region of the emitter (Fig. 2.2a).

$$Q_{RHT} = Q_{NF} + Q_{FF} \tag{2-1}$$

Based on this radiative heat flux, we then define a radiative heat conductance, normalized by the absolute temperature difference between the emitter and the receiver as $h_{RHT} = Q_{RHT} / (\Delta T_{ref} - \Delta T_{NF})$, where $\Delta T_{ref}$ is calculated as $Q_{in}/ G_{dev}$.

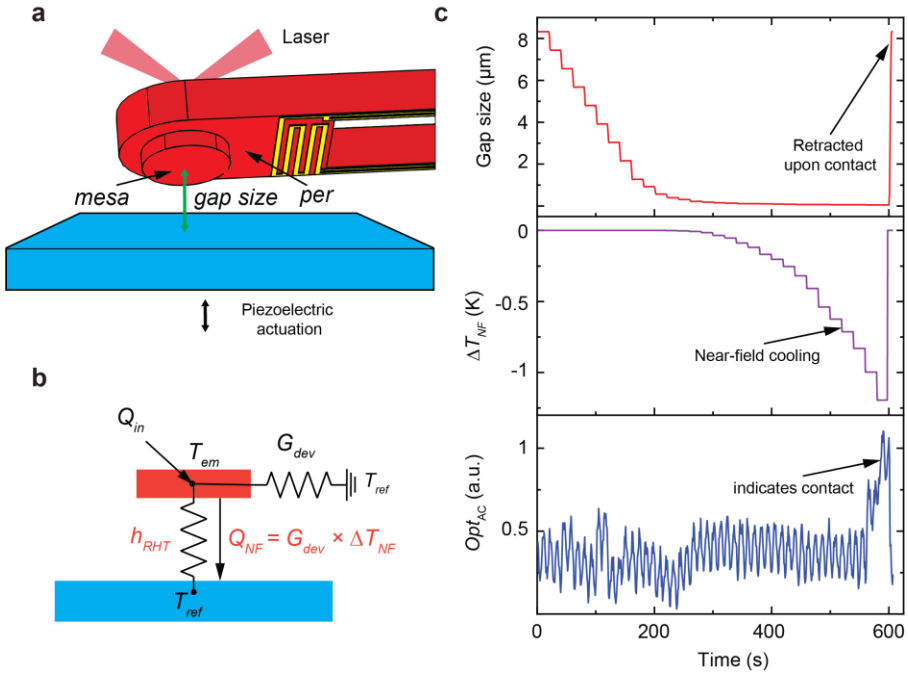


*Figure 2.2 Experimental approach.*

*(a) Schematic describing the experimental assembly of the devices in the nanopositioner. The gap size is controlled using a piezoelectric actuator on the receiver side. The emitter is heat by passing current through the platinum resistor. A red laser is focused on the backside of the emitter and the reflected light is collected in a photodiode to establish contact with the receiver. (b) Thermal model of our system, showing the temperatures at the three nodes. The corresponding thermal resistances/conductance along with the heat inputs is shown. (c) Real-time data acquired during a near-field approach between devices coated with $MgF_2$ and the emitter heated by 19.5 K. The first panel shows the gaps taken before making contact. Large steps are taken initially and smaller step sizes of ~2 nm are taken before contact. The second panel shows the corresponding temperature changes of the emitter. Clearly, large changes*

*are observed in the last few hundred nanometers, indicating near-field enhancement. The third panel is the optical signal which does not change until contact occurs between the two devices. A sudden change in this signal indicates contact.*

### 2.4 Results

Figure 2.3a shows the experimental results for devices that were coated with 85-nm thick $MgF_2$ using an evaporation technique. The $Q_{RHT}$ is plotted as a function of gap size for two different temperature rises of the emitter. In the far-field at a gap size of 7.5 μm, the $Q_{RHT}$ is 76 $W/m^2$ and 158 $W/m^2$ for $\Delta T_{ref}$ = 12 K and 19 K respectively resulting from propagating waves. At a gap size of 50 nm, the $Q_{RHT}$ increased to 33.5 $kW/m^2$ and 62 $kW/m^2$ respectively, a 400-fold enhancement in the near-field as compared to the far-field. The smallest gap size of ~45 nm achieved in this study is only limited by the unavoidable presence of few nano-particles added during the deposition process (Fig. 2.2d). It can be seen in Fig. 2.3a that a significant change in $Q_{RHT}$ occurs only below ~200 nm. This is due to the thickness of $MgF_2$ layer employed in this study. When the gap size is comparable to the thickness of the film, here ~100 nm, the thin-film RHT approaches that of a bulk RHT case[78]. This is also validated by our theoretical calculations between a thin-film and bulk case, where, due to the penetration depth of the SPhPs responsible for the NF enhancement, thin-film RHT approached that of a bulk case below 100 nm.

The radiative heat conductance $h_{RHT}$ as defined previously, is plotted in Fig. 2.3b as a function of gap size between 40 nm and 1 μm for the two cases. Clearly, both the trends (light and dark blue squares) agree quite well with each other. In order to affirm that the NF enhancement is due to the presence of the polar dielectric film, we also performed a control experiment between the emitter and a receiver without any dielectric deposition on Si surfaces (400 nm deep B-doping $1\times10^{21}$ $cm^{-3}$). This experimental data is presented as magenta triangles in Fig. 2.3b, which is in good agreement with the theoretical calculation (solid magenta line). A clear RHT enhancement

due to the presence of the $MgF_2$ film is noticed. In fact, at a gap size of 50 nm, the $h_{RHT}$ increased from 68 W/m$^2$ K to 3124 W/m$^2$ K due to the addition of $MgF_2$. While this measurement between DSi-DSi serves as a control for this study, we note that this is also the first NFRHT measurement between doped silicon ($1\times10^{21}$ cm$^{-3}$ B-doped) plates at gap sizes down to 25 nm.

Next, we calculated the $h_{RHT}$ between multilayer semi-infinite objects as a function of gap size for different material systems in using the framework of fluctuational electrodynamics. The total radiative conductance is calculated as the sum of the contributions from the 'mesa' which is directly in the NF, and 'per' – the region on the emitter that is always in the far-field. The 'mesa' structure is modelled as a 6-layer device (Fig. 2.1c), while the 'per' region is modelled as a 4-layer structure. The receiver is modelled as a 2-layer structure with the thin dielectric on silicon substrate. The dielectric functions of materials were acquired from different sources for intrinsic Si, $SiO_2$[79], Doped Si[80]. The published optical data on $MgF_2$ and $Al_2O_3$ films vary widely due to different deposition conditions and sample preparation. So, we measured the optical constants for $MgF_2$ and $Al_2O_3$ in a wavelength range of 1.7-33 μm using a spectroscopic ellipsometer. For comparison, we also used previously published data and calculated the radiative heat conductance[79].

In Figure 2.3b, the solid blue line is the calculated $h_{RHT}$ based on measured dielectric permittivity of our sample, whereas the dashed blue line corresponds to the calculations performed using dielectric permittivity tabulated in the literature. Our gap-dependent experimental data (blue squares) and the corresponding theoretical calculations (blue solid and dashed lines) are in good agreement, with the slight variations possibly due to the slightly different dielectric functions. Importantly, we contrast our results with the bulk $SiO_2$-$SiO_2$ case, shown as black solid line in Fig. 2.3b. Recent experiments in the plane-plane configuration have established the validity of FED

calculations to predict RHT between $SiO_2$ plates[19, 31]. At all gaps below 100 nm, the $h_{RHT}$ for MgF2 is ~2.5 times larger than that of $SiO_2$, for example, at 50 nm, the radiative heat conductance for $SiO_2$ system is 1075 W/m$^2$ K as opposed to 2500 W/m$^2$ K for $MgF_2$.

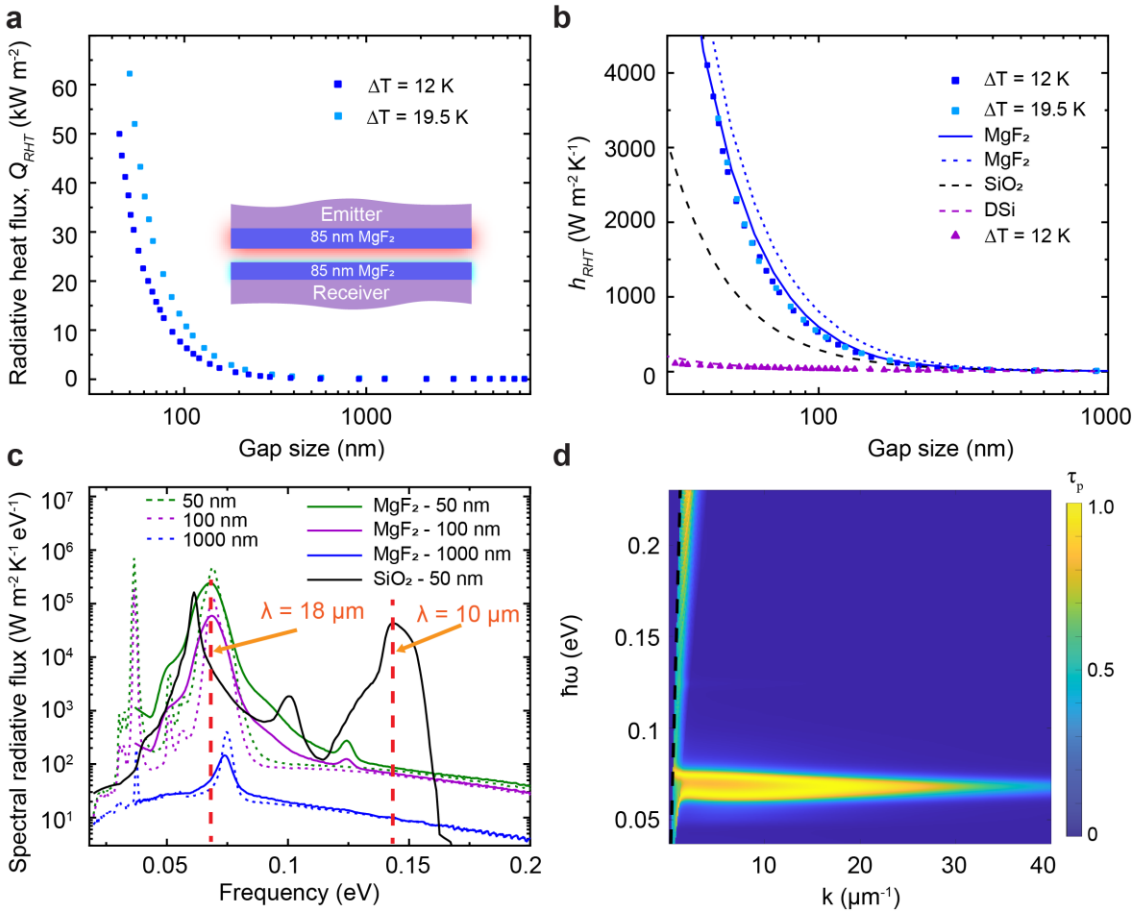


*Figure 2.3 Experimental results on devices coated with $MgF_2$.*

*(a) The total radiative heat $Q_{RHT}$ is plotted as a function of gap size, for two different temperature rises of the emitter. Both the experiments indicate large enhancements in the near-field as compared to the far-field. The inset shows the thickness of $MgF_2$ employed in these measurements. (b) The normalized radiative heat conductance $h_{RHT}$ for the two temperature rises (light and dark blue squares) presented in Fig. 2.3a, is plotted as a function of gap size. The magenta triangles represent the experimental results for $h_{RHT}$ between emitter and receiver without the dielectric coating. The dashed lines represent the theoretical calculations based on dielectric functions obtained from the literature. The solid blue line is obtained by using the measured optical data for our $MgF_2$ samples. Note the good agreement between the experimental data and blue solid line. (c) Calculated spectral radiative heat flux between 0.02-0.2 eV for gap sizes of 50, 100 and 1000 nm. Solid lines represent the calculations based on the measured dielectric function while the dashed lines represent calculations based on reported data. The black solid line is the spectral heat flux for $SiO_2$. (d) The transmission probability of TM modes at a gap size of 50 nm, plotted as a function of frequency and parallel wavevector.*

To gain further insights into the mechanism for this enhancement, we plot the spectral radiative flux of our system for three gap sizes of 50 nm, 100 nm and 1000 nm in Fig. 2.3c. A narrow-band NF enhancement predominantly occurs at 18 μm as the gap size is reduced from 1000 nm to 50 nm (solid lines calculated using measured dielectric function), due to the contribution from SPhP resonance in $MgF_2$. A clear distinction between the width of the peaks can be noticed when compared with the calculations using dielectric functions based on crystalline $MgF_2$ due to the amorphous nature of our films. In fact, the measured dielectric function showed significant inhomogenous broadening of the SPhP resonance around 18 μm. This is further supported by XRD characterization of the films which did not reveal any peaks other than that of the underlying silicon substrate, indicating the amorphous nature of the films. Due to the inherent broadband nature of RHT, such broadening of the resonances does not significantly affect $h_{\mathrm{RHT}}$, as substantiated by the good match with our experimental data. More importantly, the SPhP resonance at 18 μm (0.068 eV) as opposed to that of 10 μm (0.143 eV) for the silica case, results in a 3-times enhanced NFRHT. In Fig. 2.3d, we also plot the transmission probabilities for the p-polarized modes, as a function of frequency ($\omega$) and parallel wavevector ($k$) at a gap size of 50 nm. $Q_{\mathrm{RHT}}$ is dominated by the TM modes around $\omega$ = 0.068 eV with contribution ($\tau_p = 1$, shown in yellow band) from very large wavevectors.

In addition to the studies on $MgF_2$ films, we have also performed experiments using $Al_2O_3$ material system, where 195 nm-thick $Al_2O_3$ films were grown on the emitter and a pristine silicon sample using atomic layer deposition. The experimental data for two different temperature rises of the emitter is plotted in Fig. 2.4a. Clearly, a 300-fold enhancement in $Q_{\mathrm{RHT}}$ for $\Delta T_{\mathrm{ref}}$ =12 K, is observed as the gap size is reduced from 8 μm to 40 nm. In Fig. 2.4b, $h_{\mathrm{RHT}}$ for both the experiments (yellow and green circles) is plotted as a function of gap size along with the theoretical calculations

based on measured dielectric function (solid green) and those obtained from the literature (green dashed line). A clear enhancement in RHT above that of $SiO_2$ is observed below 50 nm, while the trend lies below the theoretical calculations.

The theoretical calculations indicate RHT enhancements of 1.5 times compared to that of $SiO_2$, in agreement with experimental data at a gap size of 40 nm with measured $h_{RHT}$ of 2,220 $W/m^2$ for $Al_2O_3$ as opposed to 1,500 $W/m^2$ for $SiO_2$. In fact, calculations based on crystalline $Al_2O_3$ indicate a 2× enhancement. Further, we plot the calculated spectral fluxes for gap sizes of 50, 100 and 1000 nm in Fig. 2.4c for both the cases of measured dielectric function (solid lines) and those obtained from literature (dashed lines). Clearly, the amorphous films show SPhP peaks with smaller amplitudes as compared to that obtained from published data, while also displaying a broader peak even larger than that observed in $MgF_2$ films. This can also be observed in the dispersion plot shown in Fig. 2.4d, indicating a broader resonance and contributions from relatively smaller wavevectors when compared to $MgF_2$ at the same gap size.

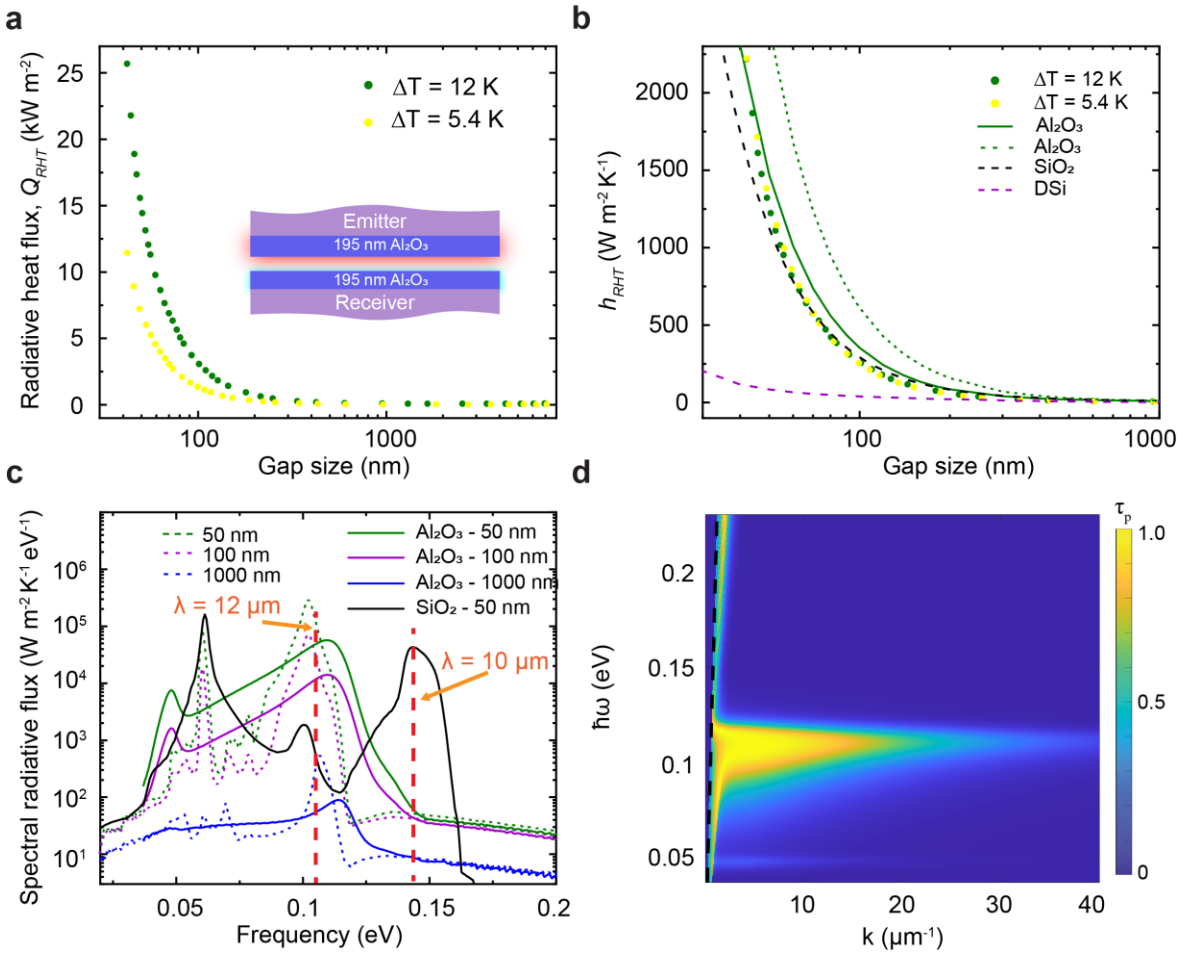


*Figure 2.4 Experimental results on devices coated with $Al_2O_3$.*

*(a) The total radiative heat $Q_{RHT}$ for two different temperature rises of the emitter. The inset shows the thickness of $Al_2O_3$ employed in these measurements. (b) The normalized radiative heat conductance $h_{RHT}$ for the two temperature rises (yellow and green circles) presented in Fig. 2.4a, is plotted as a function of gap size. The dashed lines represent the theoretical calculations based on dielectric functions obtained from the literature. The solid green line is calculated by using the measured optical data for our $Al_2O_3$ samples. (c) Calculated spectral radiative heat flux between 0.02-0.2 eV for gap sizes of 50, 100 and 1000 nm. Solid lines represent the calculations based on measured dielectric function while the dashed lines represent calculations based on reported data. The black solid line is the spectral heat flux for $SiO_2$. Resonance peaks can be observed at ~12 μm. (d) The transmission probability of TM modes at a gap size of 50 nm, plotted as a function of frequency and parallel wavevector.*

Finally, we also explored other common optical materials for enhanced RHT beyond that of $SiO_2$ and report the calculated $h_{RHT}$ in Fig. 2.5. For these calculations, we consider RHT between bulk materials instead of the multi-layered structure analyzed in our study. Among the common fluorides like NaF, $CaF_2$, $BaF_2$ etc., only $MgF_2$ comprises the strong phonon resonance at 18 μm while other fluorides possess resonances only at longer wavelengths leading to smaller radiative

heat fluxes. Materials including MgO, synthetic spinel systems like $MgAl_2O_4$ and AlON[79] show appreciable RHT enhancements over $SiO_2$. These materials can either be evaporated or sputtered to form smooth but amorphous films. Based on the experiments in this study, it should be possible to further tune the deposition and sample preparation of these class of materials to enable larger RHT.

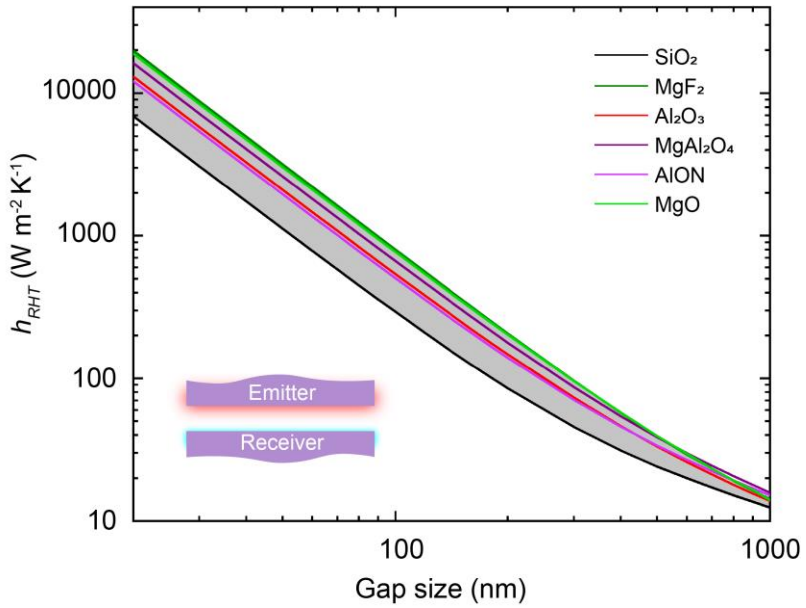


*Figure 2.5 Theoretical radiative heat conductance $h_{RHT}$ as a function of gap-sizes for different practical material systems.*

*The inset indicates that the calculations were performed on bulk materials. The grey region represents the space where RHT enhancements above that of $SiO_2$ can be achieved, bounded by $MgF_2$ on the top.*

## 2.5 Conclusion

To summarize, we deposited smooth films of $MgF_2$ and $Al_2O_3$ on micro-fabricated calorimeters and systematically measured RHT at varying gap sizes from ~8 μm down to 40 nm. While $MgF_2$ features a wide transparency window from 0.12 - 8 μm, it is nonetheless a good material for NFRHT due to the strong phonon resonance at 18 μm. At relevant gap sizes, these results represent a ~2.5 times higher radiative heat fluxes when compared to past experiments with $SiO_2$ surfaces. Next, we calculated the expected RHT using a fluctuational electrodynamics framework which showed good agreement with our experiments. While the measured dielectric

functions vary from that of the published data, the experimental data shows good agreement with the theoretical calculations based on measured optical data. Further, we also discuss the experimental data on $Al_2O_3$ material system at different gap sizes and its spectral characteristics. Finally, we presented theoretical predictions of NFRHT in other material systems with $h_{RHT}$ greater than that of $SiO_2$.

# Chapter 3 Near-field Thermophotovoltaics for Direct Conversion of Heat to Electricity

Reproduced with permission from references[65, 68]:

A. Fiorino*, L. Zhu*, D. Thompson, R. Mittapally, P. Reddy, E. Meyhofer, *Nature Nanotechnology*, 13, 806-811 (2018).

Rohith Mittapally*, B. Lee*, L. Zhu, A. Reihani, J. W. Lim, D. Fan, S.R. Forrest, P. Reddy, E. Meyhofer, *Nature Communications*, 12, 4364 (2021).

## 3.1 Abstract

Thermophotovoltaic approaches that take advantage of near-field evanescent modes are being actively explored due to their potential for high-power density and high-efficiency energy conversion. However, progress towards functional near-field thermophotovoltaic devices has been limited by challenges in creating thermally robust planar emitters and photovoltaic cells designed for near-field thermal radiation. Here, we demonstrate record power densities of ~5 kW/m$^2$ at an efficiency of 6.8%, where the efficiency of the system is defined as the ratio of the electrical power output of the PV cell to the radiative heat transfer from the emitter to the PV cell. This was accomplished by developing novel emitter devices that can sustain temperatures as high as 1270 K and positioning them into the near-field (<100 nm) of custom-fabricated InGaAs-based thin film photovoltaic cells. In addition to demonstrating efficient heat-to-electricity conversion at high power density, we report the performance of thermophotovoltaic devices across a range of emitter temperatures (~800 K – 1270 K) and gap sizes (70 nm – 7 μm). The methods and insights achieved

in this work represent a critical step towards understanding the fundamental principles of harvesting thermal energy in the near-field.

### 3.2 Introduction

Direct conversion of heat to electricity is expected to play a critical role in developing novel thermal energy storage and conversion[81] technologies. Thermophotovoltaic (TPV) devices that are composed of a hot thermal emitter and a photovoltaic (PV) cell are currently being actively explored for such energy conversion applications. In TPV devices electromagnetic radiation emitted by a hot body, when incident on a PV cell, generates electrical power via the photovoltaic effect (see reviews[82, 83]). The performance of a TPV system is characterized by two metrics: efficiency, which is defined as the ratio of electrical power output to the total radiative heat transfer from the hot emitter to the PV cell at room (or ambient) temperature, and the power density that is the electrical power output per unit area. Recently, efficiencies of up to 30% in the far-field have been reported[52, 53], where the emitter (at ~1450 K) and the PV cell are separated by distances larger than the characteristic thermal wavelength. However, the power densities of far-field TPV systems are constrained by the Stefan-Boltzmann limit, since only propagating modes contribute to energy transfer. This limit can be overcome by placing the hot emitter in close proximity (nanoscale gaps) to the PV cell, where, in addition to the propagating modes, evanescent modes also contribute and dominate the energy transfer. The enhancements in heat transfer via near-field (NF) effects have long been predicted[3, 4, 84] and directly demonstrated in recent work[15, 18, 19, 21, 32], paving the way for TPV applications. In fact, several computational studies[56-63, 85-90] have suggested that it is possible to achieve high-power, high-efficiency TPV energy conversion via NF effects.

In spite of these predictions, few experiments have probed NFTPV energy conversion. This limited progress is due to multiple challenges associated with creating thermal emitters that are robust at high temperatures, creating high-quality PV cells for selectively absorbing above-band gap NF thermal radiation and maintaining parallelization while precisely controlling the gap between the heated emitter and the PV cell. Recently, a NFTPV system developed by some of us demonstrated significant enhancements in power output compared to the far-field[65] (detailed description in the next section titled 'Preliminary work') but featured very low efficiencies (<0.1 %) and low power output (~6 $W/m^2$). Further, two other experiments also reported large enhancements in power output compared to the far-field by employing different experimental platforms[66, 67]. Nevertheless, all of these demonstrations show limited efficiency and power density, with the best-reported device[66] featuring a maximum efficiency of ~0.98% at a power density of ~120 $W/m^2$ when operated at a maximum temperature of 1040 K. More recently, another work[69] probed the principles of NFTPV energy conversion in a sphere–plane geometry using a spherical graphite emitter and InSb PV cells that were cryogenically cooled to obtain high cell efficiency. However, given the significant energy expenditure in cooling such devices, the overall efficiency is expected to be low. Thus, high-performance NFTPV demonstrations were limited due to emitters operating at relatively low temperatures and PV cells with poor performance.

### 3.3 Preliminary work

#### *3.3.1 Devices and experimentation*

To directly demonstrate the performance enhancement achievable by NFTPV, we leveraged microscale devices for the thermal emitter and the PV cell. We custom-fabricated (Fig.

3.1a) the emitter from Si with a 15 μm tall, 80 μm diameter circular mesa, seen in Fig. 3.2a. In our NFTPV devices, this extremely flat and clean mesa region is positioned into the near-field of the PV cell and a serpentine Pt heater, located next to the mesa, is used to elevate the emitter's temperature up to ~655 K. The emitter structure is suspended by a simply-supported, thermally isolating 550μm-long double-beam that effectively confines the temperature rise to the emitter island and eliminates buckling that may arise due to thermal expansion in fully-constrained structures as used in previous work[20]. The PV cell (Fig. 3.2b) is a commercially available photodiode (Electro Optical Components Lms36PD-03) with a 0.345 eV bandgap energy. This relatively narrow bandgap was chosen because of its suitability for harnessing power from low-quality waste heat ($T$ ~ 655 K). The cell roughness was determined to be ~5 nm peak-to-peak via atomic force microscopy.

**Fabrication of suspended emitter microdevice**

A schematic diagram of the fabrication process for the emitter device is shown in Fig. 3.1a. The device is fabricated from a double-bonded silicon-on-insulator (SOI) wafer with a 500 μm-thick Si handle layer, a 40 μm-thick middle Si device layer, a 15 μm-thick top Si device layer, and two 1 μm-thick buried oxide (BOX) layers (Step 1). All Si layers are initially lightly doped. The top device layer is first doped to a level of $2.7\times10^{20}$ $cm^{-3}$ via phosphorous diffusion at 975 ºC for 12 minutes (Step 2). A phosphosilicate glass (PSG) layer that forms on the top device layer during the diffusion process is subsequently stripped using a buffered hydrofluoric (BHF) acid solution (Step 3). The top device layer is then etched until the upper BOX layer is revealed using reactive ion etching (RIE) to form a 15 μm-tall mesa (Step 4). Then, a 30 nm-thick Pt heater and 100 nm-thick Pt electrical leads are patterned onto the upper BOX layer using successive liftoff processes (Step 5). The structure of the device is formed by RIE etching through the upper BOX layer, the

middle Si device layer, and the lower BOX layer using the same etch mask (Step 6). The Si handle layer is then etched from the backside via deep RIE (DRIE) to suspend the device (Step 7). A scanning electron microscope (SEM) image of the fabricated device is shown in Fig. 3.1b.

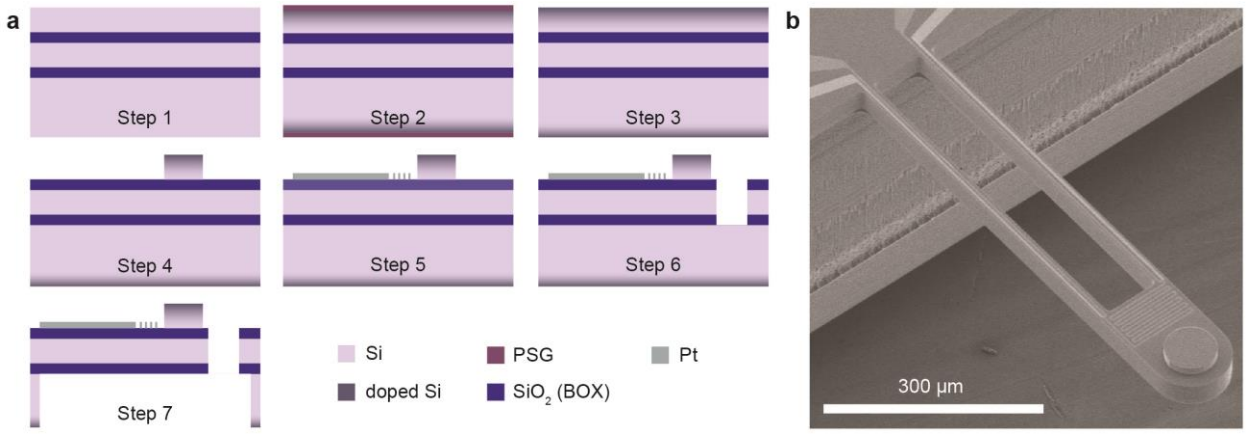


*Figure 3.1 Fabrication of the emitter microdevice.*

*a, Schematic of the seven-step emitter microdevice fabrication process. b, Scanning electron micrograph of the fabricated structure.*

We parallelized and laterally aligned the emitter and cell using our custom-built nanopositioner, which is described in detail elsewhere[20, 78, 91]. Briefly, our nanopositioner affords several degrees of freedom, as schematically illustrated in Fig. 3.2c. Both the emitter and cell can be translated in the *x* and *y* directions and rotated about the *x* and *y* axes, ($\theta_x$ and $\theta_y$) with ~6 μrad precision. Additionally, the cell can be translated along the vertical *z* direction via piezoelectric actuation, thus enabling control of the gap between emitter and PV cell to ~2 nm resolution. Parallelization of the emitter and the PV cell was carried out in two stages, first, using a high numerical aperture optical microscope and second, by optimizing the open circuit voltage (see Methods), achieving parallelism to within ~25 nm across the 80 μm mesa. Finally, the positioner along with the NFTPV device was located in a high vacuum (~$10^{-7}$ Torr) system and isolated from external vibrations via suspension on an optical table.

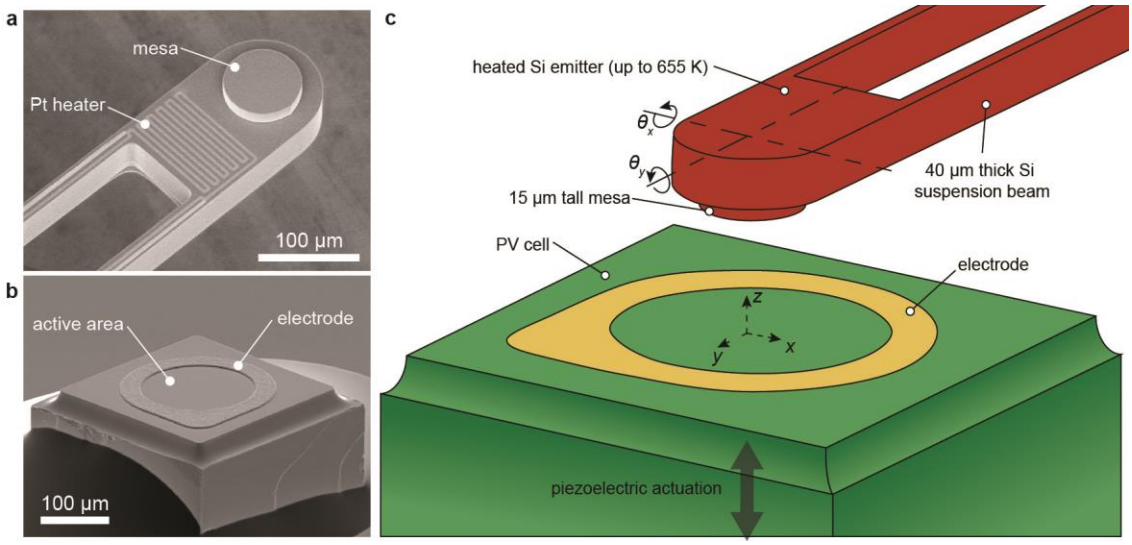


*Figure 3.2 Microscale devices for demonstration of near-field thermophotovoltaic energy conversion.*

*a, Scanning electron micrograph of the emitter device. The 15 µm tall, 80 µm diameter mesa can be heated to ~655 K via the integrated Pt heater. b, Scanning electron micrograph of the PV cell device which features a 300 µm × 300 µm active area which is partially obscured by the top electrode. In experiments, the top electrode is accessed via wire bonding (not shown). c, Schematic illustration of the TPV device orientation. Both devices can be translated in the x- and y-dimensions. Angular control of the emitter allows for parallelizing the devices and a piezoelectric actuator is used to precisely control the vacuum gap size.*

### *3.3.2 Results*

We first investigated the power output from a TPV system with a bandgap of 0.345 eV. Towards this aim, the emitter was positioned directly above the PV cell (Fig. 3.3a) and known amounts of heat were dissipated in the emitter via Joule heating to systematically raise the emitter temperature, $T_E$, from room temperature to values as high as 655 K. The temperature rise of the emitter was carefully characterized via independent measurements ensuring that the uncertainty in the temperature rise was small (±5 K). The temperature of the PV cell was not controlled but is estimated to remain near room temperature (temperature rises are ~0.1 K for the highest emitter temperature). Next, using a source measure unit (Keithley 2401), we swept the cell current and measured the corresponding cell voltage. This yielded *I-V* curves that shift further into the first quadrant as the emitter temperature is increased, as shown in Fig. 3.3b. The maximum power point,

$P_{MPP}$, was calculated by locating the point on the *I-V* curve for which $I \times V$ is maximized (graphically shown as the shaded area in the inset of Fig. 3.3c).

To study the effect of gap size on the power output of our TPV devices, we displaced the cell towards the emitter using piezoelectric actuation and acquired *I-V* sweeps, yielding a family of *I-V* curves and maximum power points for each gap size. Figure 3.3c shows data from an experiment where the gap size was systematically reduced from ~12 μm to contact, in discrete steps, where the smallest steps (~5 nm) were taken near contact. At each step, an *I-V* curve was taken as described previously. The curves shift further into the first quadrant as the gap size decreases (inset of Fig. 3.3c top panel), indicating a higher electrical output power $P_{MPP}$ when operating at smaller gaps. An optical detection method with a laser beam incident on the emitter and a split photo-diode, akin to approaches employed in atomic force microscopy, was adopted to detect contact between the emitter and PV cell (see Fig. 3.3a). Specifically, the deflection of the emitter was detected using two complementary approaches (see bottom panels of Fig. 3.3a), which sense the optical signal shift due to deflection of the emitter (called dc signal) and the signal due to modulation of the emitter deflection (called ac signal). Both ac and dc optical signals remain unchanged until contact occurs, at which point they undergo a step change. Additionally, a large temperature drop in the emitter is observed as radiative heat transfer gives way to conduction. Given the size of particles on the emitter (~55 nm), the PV cell roughness (~5 nm), and *z*-piezo resolution (~5 nm), we estimate that a minimum gap size of 60 ± 6 nm is achievable. The uncertainty of ±6 nm arises from summing the minimum piezo step size (4 nm), the piezo signal noise (1 nm), and effects from possible deviations from parallelism (1 nm). To reflect the minimum gap size of 60 nm, we offset the gap size at contact by 60 nm (Fig. 3.3c, top panel), consistent with previous work[20].

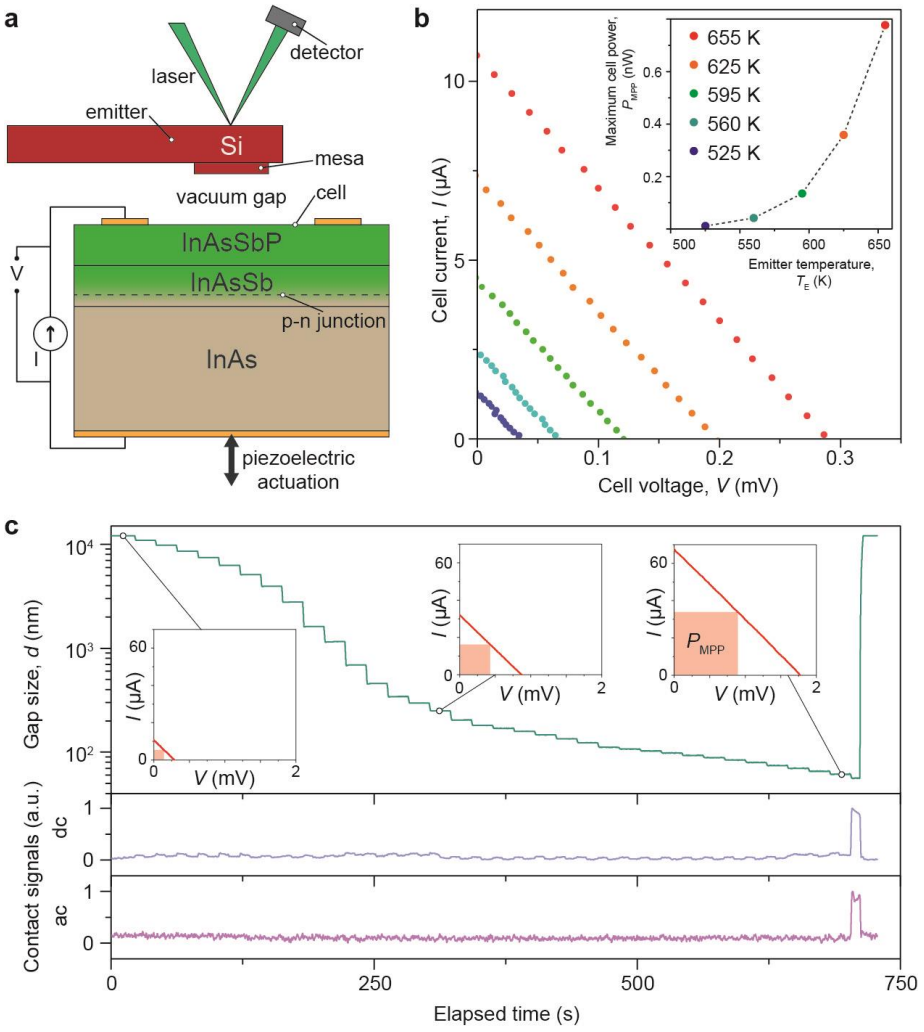


*Figure 3.3 Thermophotovoltaic measurement procedure.*

*a, Schematic side view depicting the device architecture and measurement scheme. Photons are emitted from the hot Si emitter and absorbed in the InAsSb active layer to generate electron-hole pairs. By sweeping the current I and measuring voltage V, the cell's I-V characteristic can be obtained as a function of gap size. Contact is detected via a laser deflection scheme. b, Cell I-V characteristic in the far-field for five different emitter temperatures ranging from 525 K to 655 K. As $T_E$ is increased, the curves shift further into the first quadrant. The inset shows the power output at the maximum power point $P_{MPP}$ for each choice of $T_E$. c, Time series data for $T_E$ = 655 K. Top panel: Evolution of the vacuum gap size over the course of a single experiment. PV cell I-V characteristics are taken during each step, and the inset shows three measured I-V curves at 12 μm, 215 nm, and 60 nm gap sizes (±6 nm). Middle panel: detection of contact based on dc change in the laser deflection. The sudden jump in the signal indicates a deflection of the emitter due to contact with the cell. Bottom panel: detection of contact based on locking-in to the 4 kHz component of the detector output.*

The measured *I-V* characteristic of our TPV system, at eight selected gap sizes, is reported in Fig. 3.4a. As the gap size was reduced from 12 μm to 60 ± 6 nm, the short circuit current $I_{sc}$ increased from 11 to 67 μA and the open circuit voltage $V_{oc}$ increased from 0.29 to 1.77 mV. $P_{MPP}$

is enhanced ~40 fold as the gap is reduced (Fig. 3.4b), from 0.77 nW in the far-field to 30.2 nW at the smallest gap size of 60 ± 6 nm. In addition, we repeated these measurements for a range of emitter temperatures ($T_E$ = 525, 560, 595, and 625 K in Fig. 3.4c), which clearly show, for example, that the power output for $T_E$ = 525 K and $d$ = 100 nm exceeds that for $T_E$ = 625 K and $d$ = 12 μm, further emphasizing that NFTPV operation across nanoscale gaps readily outperforms conventional TPV, even at significantly lower temperatures.

To compare our results to the theoretical expectation, we modelled our cell *I-V* characteristic by accounting for radiative and non-radiative contributions to the cell current,

$$I(V) = I_{\text{rad}}(V) - I_{\text{Auger}}(V) - I_{\text{SRH}}(V), \tag{3-1}$$

where $I_{\text{rad}}$ is the net current generated due to radiation, and $I_{\text{Auger}}$ and $I_{\text{SRH}}$ represent current lost to Auger and Shockley-Read-Hall (SRH) recombination, respectively. Because calculating $I_{\text{rad}}$ requires knowledge of the above-bandgap photon flux, we modelled our system using fluctuational electrodynamics with a numerically-stable scattering matrix formalism (S-matrix)[92, 93] which enables computation of the radiative heat transfer between any pair of layers in a 1D system[94-96]. In our model we assume that each above-bandgap photon absorbed in the junction creates an electron-hole pair, and make use of the relevant electronic and optical properties (e.g. doping) of the device materials obtained from previous work[97]. Following the scattering matrix approach, the net photogenerated current $I_{\text{rad}}$ is given by:

$$I_{\text{rad}}(V) = A_{\text{mesa}} e \int_{\omega_g}^{\infty} d\omega \frac{1}{\lambda^2} \left[ \phi_{\text{E}\to\text{J}} \left( \frac{1}{e^{\frac{\hbar\omega}{k_B T_E}} - 1} - \frac{1}{e^{\frac{\hbar\omega - qV}{k_B T_J}} - 1} \right) + \phi_{\text{A}\to\text{J}} \left( \frac{1}{e^{\frac{\hbar\omega}{k_B T_A}} - 1} - \frac{1}{e^{\frac{\hbar\omega - qV}{k_B T_J}} - 1} \right) \right], \tag{3-2}$$

where $f_{1\to2}$ is the computed transfer function from body 1 to body 2 (subscripts *E*, *J*, and *A* for emitter, junction, and ambient, respectively). Note that our model requires two fitting parameters: the view factor *f* from the non-mesa region of the emitter to the cell, which is chosen so that our

modelled power output matches the measured values in the far-field, and the surface recombination velocity *S*, which is determined by fitting the slope of the *I-V* curve to the measured data.

Because our model indicates that the TPV performance is sensitive to errors in emitter temperature of a few Kelvin, and because our estimate of the emitter temperature has an uncertainty of ±5 K, we depict our theoretically computed data in Fig. 3.4b by a shaded region bounding $T_E \pm 5$ K. Comparing the experimentally measured data to the shaded region in Fig. 3.4b, the measured electrical output power ($P_{MPP}$) from our TPV system operating at 655 K is in good agreement with the computed expectation at all gaps. Similarly, good agreement holds at all other emitter temperatures considered (Fig. 3.4c). Therefore, we believe that our model provides an accurate description of the experimental findings and further supports our conclusions regarding the enhancements observed in NFTPV. In Fig. 3.4d, we report the modelled energy flux spectrum from emitter to cell. The lower panel of Fig. 3.4d shows the computed spectral energy flux at the smallest gap ($d$ = 60 nm) when the emitter is at 655 K. The green shaded region represents the maximum energy extractable by the TPV at this gap size, while the red and blue regions represent losses. At a 60 nm gap, the energy flux exceeds the limit for blackbodies by more than threefold, which leads to the observed enhancement in $P_{MPP}$. The middle and upper panels show how the energy flux decreases with increasing gap size. In the far-field, the energy flux is greatly diminished compared to blackbody exchange (Fig 3.4d, upper panel).

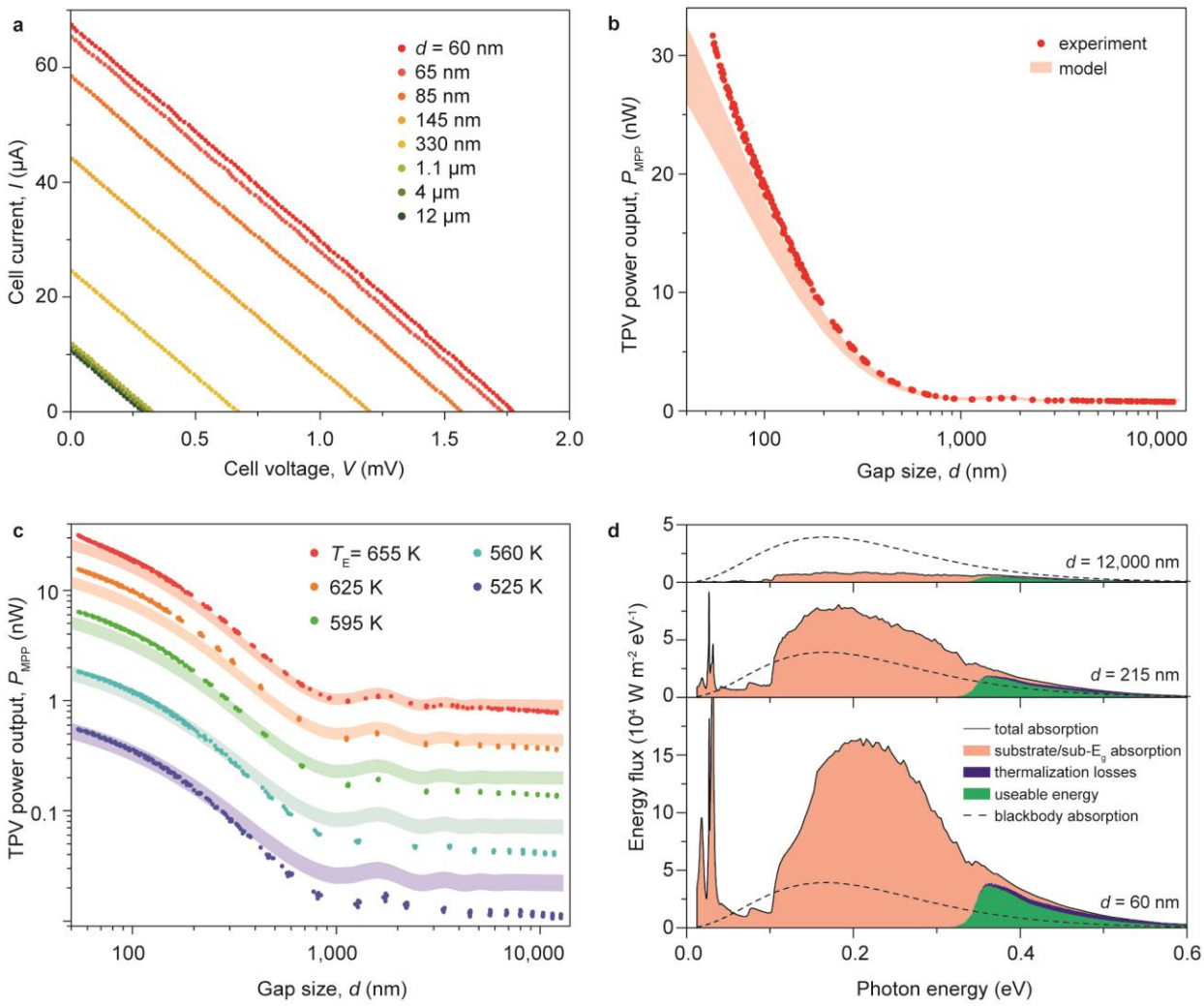


*Figure 3.4 Thermophotovoltaic performance enhancement in the near field.*

*a, Measured I-V curves at various gap sizes for the 0.345 eV-bandgap cell when $T_E$ = 655 K. As the gap size decreases, the curve shifts further into the first quadrant. b, Measured TPV power output $P_{MPP}$ vs. gap size d for the 0.345 eV-bandgap cell when $T_E$ = 655 K. When d = 60 ± 6 nm, $P_{MPP}$ is enhanced ~40-fold relative to the far-field. The shaded region indicates the theoretically expected values for 650 K < $T_E$ < 660 K c, Measured $P_{MPP}$ vs. d for $T_E$ ranging from 525 K to 655 K. The shaded regions indicate the theoretical expectation for the indicated $T_E$ ± 5 K. d, Calculated spectral energy flux for emitter temperature $T_E$ = 655 K and gap size d = 60 nm (lower panel), 215 nm (middle panel), and 12 μm (upper panel), from our computational modelling. The green shaded region represents, for an ideal cell, the maximum energy extractable from above-bandgap photons absorbed in the active layer, while the blue region represents the excess photon energy lost to thermalization. The red shaded region represents lost energy due to photon absorption in the substrate/cladding layers as well as to below-bandgap absorption in the active layer.*

To clarify the effect of bandgap on the TPV performance, we repeated our measurement using a different PV cell with a slightly narrower bandgap, 0.303 eV (Electro Optical Components Lms41PD-03), for which we obtained results shown in Figs. 3.5a & b. The minimum effective gap size attainable with this PV cell increased to 75 nm due to the increased surface roughness (53 nm

peak-to-peak), leading to a slightly more modest power output enhancement of ~33-fold. To obtain a quantitative comparison between the 0.303 eV- and 0.345 eV-bandgap cells in our TPV system, we plot $I_{sc}$, $V_{oc}$, and $P_{MPP}$ for both cells when $T_E$ = 525 K (Fig. 3.5c) and $T_E$ = 655 K (Fig. 3.5d). It is evident from Fig. 3.5c that at $T_E$ = 525 K, employing the smaller bandgap cell improves the TPV power output: the increase in $I_{sc}$ in the 0.303 eV cell more than compensates for the decrease in $V_{oc}$, leading to slightly higher $P_{MPP}$ at a given gap. At higher temperatures, however, when the emission shifts to higher energy[98], the higher bandgap cell clearly outperforms its narrower-bandgap counterpart (Fig. 3.5d) in terms of the power output.

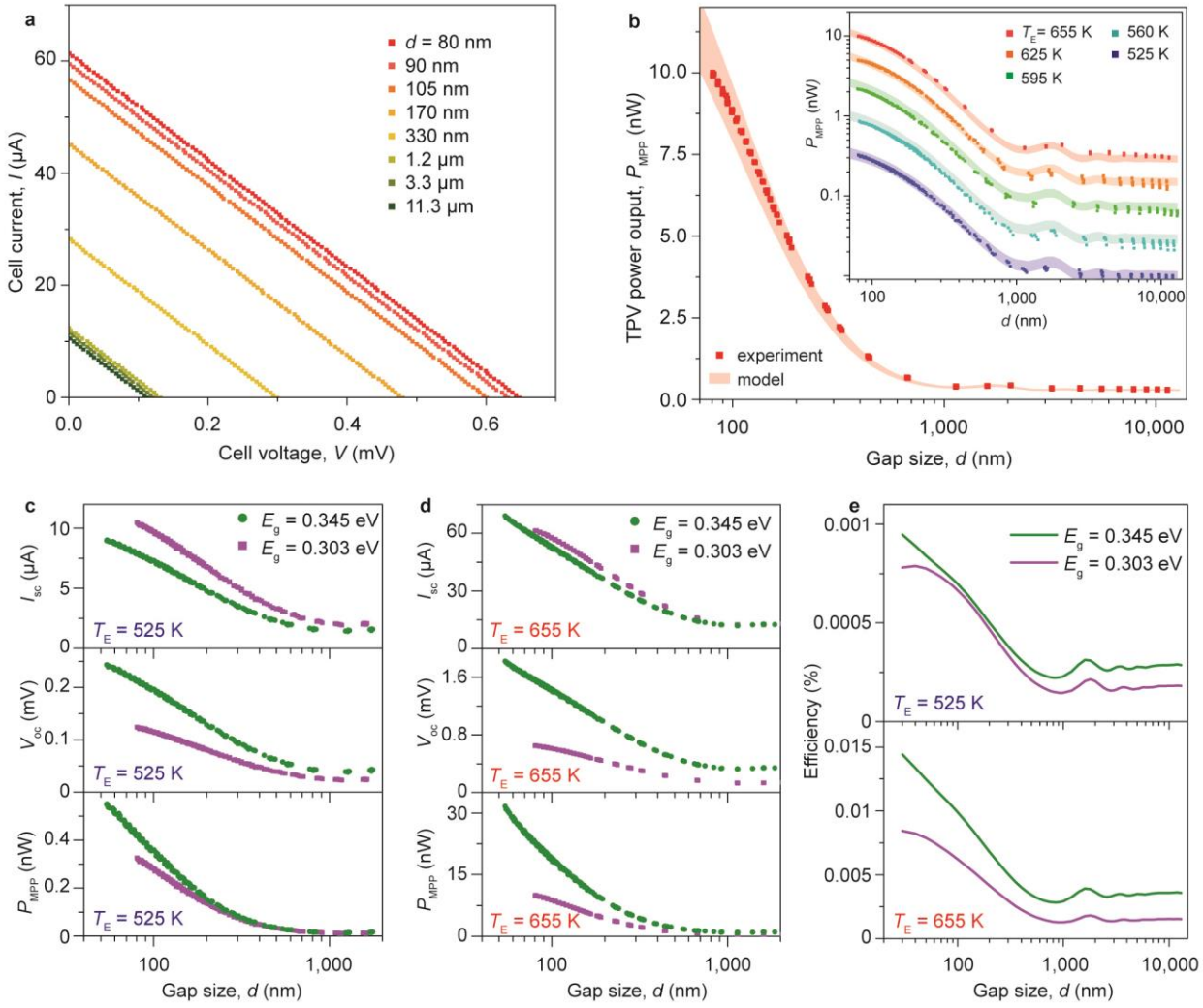


*Figure 3.5 Near-field thermophotovoltaic measurement with 0.303 eV-bandgap cell.*

*a, Measured I-V curves at various gap sizes for the 0.303 eV-bandgap cell when $T_E$ = 655 K. b, Measured TPV power output $P_{MPP}$ vs. gap size d for the 0.303 eV-bandgap cell when $T_E$ = 655 K. When d = 120 nm, $P_{MPP}$ is enhanced by a factor of 33 relative to the far-field. The shaded region indicates the theoretical expectation for $T_E$ = 655 K ± 5 K from our modelling. Inset: Measured $P_{MPP}$ vs. d for $T_E$ in the range from 525 to 655 K (points), with modelled (shaded region). c, Measured short circuit current $I_{sc}$ (top panel), open circuit voltage $V_{oc}$ (middle panel), and TPV output power $P_{MPP}$ (lower panel) vs. gap size d for both cells at $T_E$ = 525 K. d, Same as in (c) but for $T_E$ = 655 K. e, Modelled TPV efficiency (defined in main text) for both cells when $T_E$ = 525 K (top panel) and 655 K (bottom panel).*

While the central goal of this work is to experimentally demonstrate that large power enhancements are possible in nanogap NFTPV devices, an analysis of the effect of gap size on efficiency is important in evaluating the performance of TPV systems. In the context of this work, we define the efficiency of our NFTPV devices as the ratio of electrical power ($P_{\mathrm{MPP}}$) extracted to the net energy radiated from the emitter to the PV cell. Since it is not possible to measure the total radiated energy directly in our setup, we used our model to estimate the energy radiated across the gap and the $P_{\mathrm{MPP}}$, from which we calculated the efficiency (Fig. 3.5e). The data suggest that efficiency is not a monotonic function of gap size in our system; a minimum in efficiency occurs for $d \approx 1$ μm, and the efficiency increases substantially when $d \lesssim 300$ nm, suggesting that NFTPVs can achieve much higher efficiency compared to TPVs operating in the far-field. The absolute values of the efficiency of our current NFTPV systems are low (~0.02%) due to the small illuminated cell areas (~5% of cell surface, which diminishes efficiency due to increased recombination), relatively low emitter temperatures, relatively low PV shunt resistance, and high energy absorption in the substrate.

### 3.4 Devices and experimentation

To further explore the principles of high efficiency NFTPV energy conversion from planar surfaces and PV cells operating at room temperature, we developed microdevices capable of being heated to temperatures as high as 1270 K, along with matching thin film PV cells (Fig. 3.6a) with a spectral response that is capable of absorbing above-band gap (ABG) thermal radiation while minimizing absorption of sub-band gap (SBG) photons[59-61]. To elaborate, the emitter features

a monolithic, doped silicon cantilever with a circular mesa (see Fig. 3.6b, Methods for details) connected to a substrate at room temperature by two stiff beams (Figs. 3.6a & 3.6d). The two beams form an electrical resistor ($R_{emitter}$) that can be employed to elevate the temperature of the mesa ($T_{emitter}$) by distributed Joule heating ($j^2\rho$), where $j$ and $\rho$ are the local current density and resistivity, respectively. Also, a 10 nm-thick layer of AlN (Fig. 3.6b) was conformally deposited over the emitter to form both an electrically insulating layer and a diffusion barrier to protect the emitter surface from degrading at high temperatures[99].

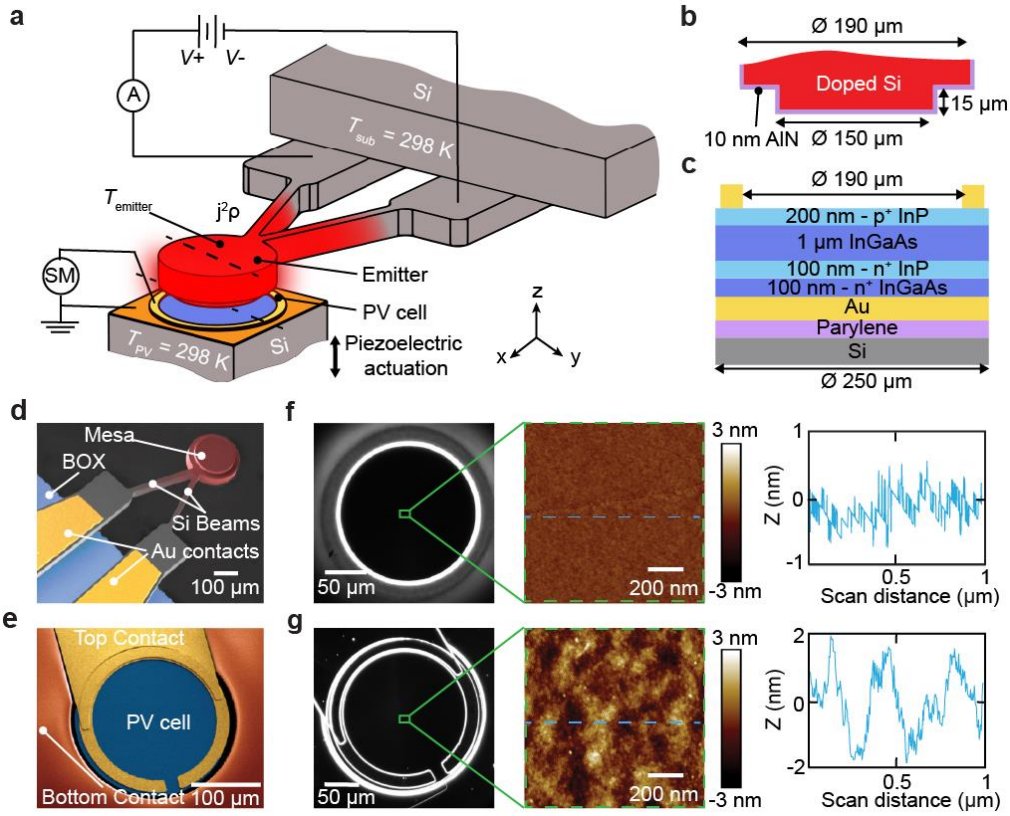


*Figure 3.6 Devices and experimental setup*

*a, Schematic depiction of the experimental setup employed for near-field thermophotovoltaic measurements. The custom-fabricated Si emitter features a suspended mesa (see panel d) that is Joule heated (heat dissipation quantified with an ammeter 'A') up to1270 K by applying a bipolar voltage (V+, V-) to the two beams. The epitaxially-grown InGaAs photovoltaic (PV) cell is moved towards the emitter via a piezoelectric actuator to systematically control the gap size while the electrical power generated is quantified with a source meter (SM). The emitter substrate and the PV cell are at a temperature of ~298 K. b, c, Cross-sectional profiles of the emitter and the PV cell at the sections along the black dashed lines in Fig. 1a. d, False-colored scanning electron micrograph (SEM) of the emitter with mesa, showing the buried oxide layer (BOX) and the gold contacts on the Si beams. The Si beams featuring a temperature gradient are depicted in red e, False-colored SEM of the PV cell showing the central active layer of the*

*PV cell (blue) as well as top (yellow) and bottom (orange) Au contacts. f, g, Dark-field microscope (left panels), atomic-force microscopy (AFM) images (middle panels) and surface roughness profiles (corresponding to the blue dashed lines in the AFM images) of the mesa (f) and the PV cell (g) are shown in the right panels. The peak-peak roughness of the mesa is ~1 nm, while that of the PV cell's active surface is ~4 nm.*

The PV cell has a circular active area of diameter 190 μm (Fig. 3.6c) to closely match the dimensions of the emitter, and features a thin film $In_{0.53}Ga_{0.47}As$ (InGaAs) layer epitaxially grown by solid source molecular beam epitaxy on an InP wafer, and transferred to a silicon substrate (see Methods). The top and bottom Au layers serve as electrical contacts (Fig. 3.6e). The bottom contact also acts as a back surface reflector (BSR) for recycling SBG photons back to the emitter[52, 53]. The emitter and the PV cell, as verified by dark-field optical microscopy[100] and AFM scans of the mesa (Fig. 3.6f) and active area (Fig. 3.6g), are extremely flat and free of particles and other contamination that would interfere with the NF operation of the TPV system.

To parallelize the emitter and the PV cell (see Methods for parallelization procedure), we employed a nanopositioning platform[19, 65, 100, 101] in a high vacuum environment (~1 μTorr), and varied the gap size between the emitter and the PV cell from micrometers to nanometers even while the emitter was heated to high temperatures (Fig. 3.6a). This was accomplished by applying a bipolar voltage across the two terminals of the emitter and maintaining the voltage of the mesa close to the ground potential (see Methods), thus reducing electrostatic interactions with the PV cell, and enabling creation of small gap sizes. Further, no additional active thermal management (i.e. refrigeration) was applied to the PV cell, as the heat transfer is primarily localized to the mesa region of the emitter interacting with the PV cell.

**Experimental scheme for probing NFTPV energy conversion**

Here we describe the experimental strategy for heating the emitter, controlling the gap between the parallelized devices, and measuring the power output at each gap size. We began our experiments by passing a current of ~70 mA through the two terminals of the emitter (Fig. 3.6a).

This results in a power dissipation of $P_{Joule}$ = 411.8 mW within the beams of the emitter and heats the mesa to a temperature, $T_{emitter}$ = 930 K, as determined by a scanning thermal probe-based method [102]. The heated emitter and PV cell were placed at an initial separation of ~7 μm using a coarse-positioning stepper motor that controls the position of the PV cell. The PV cell was then stepped closer to the emitter using a feedback controlled piezoelectric actuator. The data corresponding to this process are shown in Fig. 3.7a, where the top panel shows that large steps of ~800 nm are taken initially followed by finer steps of ~2 nm before contact. The electrical resistance ($R_{emitter}$) of the emitter (third panel, Fig. 3.7a) and the short-circuit current ($I_{sc}$ at $V = 0$) measured across the PV cell (schematic, fourth panel Fig. 3.7a) at each gap size do not change significantly during the initial steps, but a large variation is seen over the last hundreds of nanometers due to NF enhancement. A sudden jump in the optical signal that monitors deflection of the emitter, which is accompanied by a simultaneous change of $R_{emitter}$ and $I_{sc}$, at the end of the approach clearly indicates contact between the devices. At this point the PV cell is quickly withdrawn, to separate the devices back to the initial gap of 7 μm.

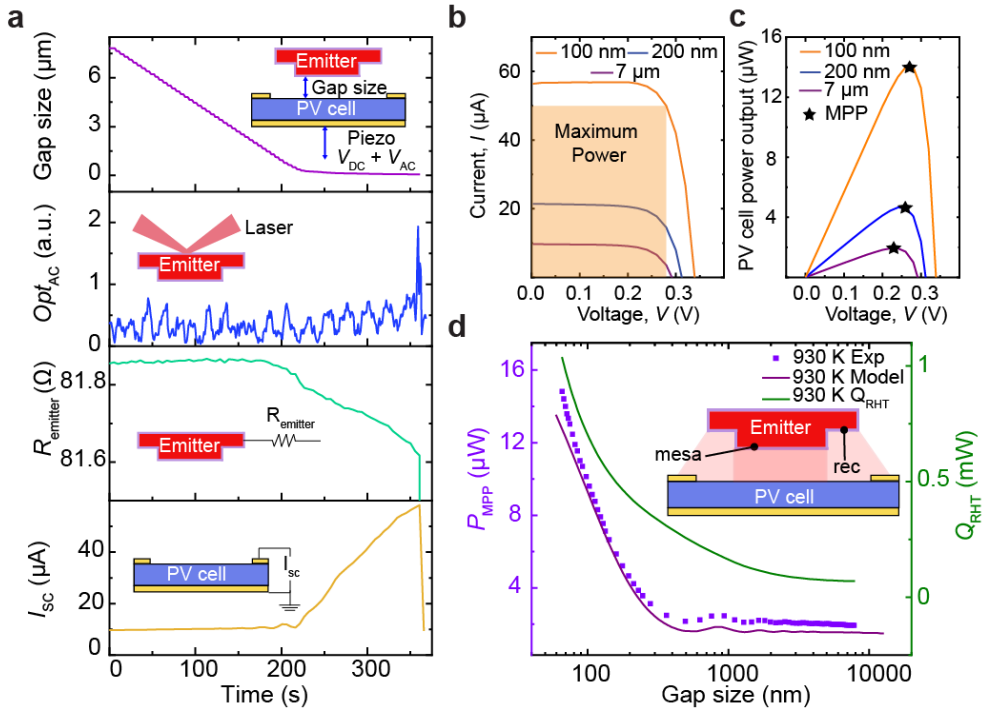


*Figure 3.7 Experimental data with an emitter heated to 930 K and the photovoltaic cell at room temperature.*

*a, Data obtained as the gap size between the emitter and the photovoltaic (PV) cell is reduced from ~7 μm to contact. The top panel shows the gap size as a function of time. The inset shows how the PV cell mounted on a piezoelectric actuator is displaced ($V_{DC}$ is the DC voltage applied to the feedback-controlled piezo and $V_{AC}$ is a superimposed small AC modulating signal at 4 kHz). The second panel shows the variation of the AC optical signal ($Opt_{AC}$), while the third and fourth panels show the changes in the resistance of the emitter ($R_{emitter}$) and short-circuit current ($I_{sc}$) in the PV cell. The simultaneous jumps in $Opt_{AC}$, $R_{emitter}$ and $I_{sc}$ indicate contact. b, Data from current-voltage (I-V) characterization performed for gaps of 7 μm, 200 nm and 100 nm. The orange shaded region represents the maximum power extractable from the PV cell for a gap size of 100 nm. c, The power output of the PV cell as a function of the voltage showing the maximum power points (MPP). d, The power output at the maximum power point ($P_{MPP}$) at different gaps. Violet squares indicate the measured data, the purple solid line represents the theoretically estimated $P_{MPP}$ and the green line shows the total radiative heat transfer ($Q_{RHT}$) between the emitter and the PV cell as a function of gap size. The inset (not to scale) indicates that both the 'mesa' (near-field contribution from the circular region in the center) and 'rec' (far-field contribution from the 15 μm-recessed circular ring) surfaces contribute to the total $P_{MPP}$ and $Q_{RHT}$.*

## 3.5 Results

To measure the electrical power output of the PV cell, its current-voltage (*I-V*) characteristics are measured at each gap size (see Methods). Typical curves are shown for gaps of 7 μm, 200 nm and 100 nm in Fig. 3.7b, where a clear upward shift of the *I-V* curve to larger short circuit currents ($I_{sc}$) and moderately increased open-circuit voltage ($V_{oc}$) is seen with decreasing gap size. The increase in $I_{sc}$ from 9.8 μA at 7 μm, to 56 μA at 100 nm can be attributed to the

increased above band-gap (ABG) photon flux from evanescent modes coupled at sub-wavelength gaps (see below). The electrical power output at the maximum power point ($P_{MPP}$, Fig. 3.7c) of the *I-V* curve is $P_{MPP} = FF \times V_{oc} \times I_{sc,}$ where *FF* is the fill factor (at 100 nm, *FF* = 0.73). The variation of $P_{MPP}$ with gap size is plotted in Fig. 3.7d (violet squares, left axis), where the PV cell power output remains around 2 μW for gaps from 7 μm to 600 nm. Below 600 nm, the power output increases substantially to 14.8 μW at the smallest gap of 70 ± 2 nm, indicating an ~8-fold power enhancement in the NF when compared to the far-field. To interpret this NF enhancement, all the surfaces of the emitter that contribute radiative energy fluxes to the PV cell must be considered. The surfaces of the emitter are labeled 'mesa' and 'rec' (see schematic Fig. 3.7d), where 'mesa' refers to the central region ($A_{mesa} = 7.07 \times 10^{-8}$ m$^2$) and 'rec' signifies the recessed ring ($A_{rec} = 4.2 \times 10^{-8}$ m$^2$) surrounding the mesa. When considering only the contribution from the $A_{mesa}$, the NF power enhancement is 11-fold relative to power generation in the far-field, whereas a smaller 8-fold enhancement is observed when contributions from $A_{rec}$ are included in the power transfer as seen in the experimental data of Fig. 3.7d. This is because only the mesa enters the NF of the PV cell, while $A_{rec}$ always remains in the far-field. Thus, the actual enhancement can be larger if all surfaces are brought into the NF.

To understand the physical mechanisms behind the enhancement, we developed a model based on the formalism of fluctuational electrodynamics[3]. Specifically, we employed our model (Methods) to estimate the power output $P_{MPP}$ and the total radiative heat transfer $Q_{RHT}$ as functions of $T_{emitter}$ and gap size for the geometries (including $A_{mesa}$ and $A_{rec}$) and materials that correspond to those employed in this work. The estimated $P_{MPP}$ is plotted as a purple line in Fig. 3.7d, which agrees with the experimentally measured $P_{MPP}$. Further, the calculated $Q_{RHT}$ is observed to continuously increase from ~72 μW at 7 μm, to ~1 mW at 70 nm.

**NFTPV performance at temperatures above 1000 K**

To understand the temperature-dependent performance of the TPV system, we systematically increased $T_{emitter}$ in steps of ~100 K and performed experiments as described above. When the emitter temperature increases, the characteristic wavelength of the radiated spectrum decreases, increasing the fraction of energy in the ABG region, and correspondingly the photocurrent ($I_{sc}$). As the emitter temperature is raised from 1050 K to 1270 K, in Fig. 3.8a we observe that $I_{sc}$ increases from 30 μA to 150 μA. Importantly, a large shift in $I_{sc}$ is seen as the gap size is reduced from 7 μm to ~100 nm; for example, at the highest temperature of 1270 K, a ~5-fold increase in $I_{sc}$ is measured (purple solid and dashed lines in Fig. 3.8a). We note that the *I-V* curve at 1050 K and a gap size of 100 nm is similar in shape to that of one obtained at 1270 K in the far-field, highlighting that NFTPVs can achieve similar or higher power outputs at significantly lower temperatures when contrasted to a comparable far-field TPV device. Further, in Fig. 3.8b, we plot $V_{oc}$ as a function of $I_{sc}$ for the different temperatures and gap sizes (the direction of the arrows signifies decreasing gap size), which indicates a logarithmic dependence of $V_{oc}$ on $I_{sc}$, characteristic of PV cells (see Methods). Thus, $V_{oc}$, $I_{sc}$ and $P_{MPP}$ increase with decreasing gap size and increasing temperature. Further, the calculated $V_{oc}$ and $I_{sc}$ (solid lines in Fig. 3.8b) agree with the experimental data over the broad range of temperatures and gap sizes explored.

The measured $P_{MPP}$ as a function of gap size is plotted in Fig. 3.8c at different temperatures between 810 and 1270 K. At all temperatures, $P_{MPP}$ increases when the gap size is decreased sufficiently; for example, at 1050 K the power output increased from ~7 μW at 7 μm, to 41 μW at a 90 nm gap, a six-fold increase due to NF enhancement. The measured (various symbols) $P_{MPP}$ agree well with that estimated from our model (color bands corresponding to $T_{emitter} \pm \Delta T$, where $\Delta T$ = 27 K when $T_{emitter}$ = 1270 K and $\Delta T$ = 10 K for other temperatures, as 10 K is the upper bound

to uncertainty in that temperature range). Non-monotonic changes in the experimental power outputs are seen for gap sizes between 500 nm and 7 μm at all temperatures due to interference effects, highlighting the capability of our platform to resolve such effects in agreement with the model.

The NFTPV energy conversion efficiency ($\eta$), defined as the ratio of the measured power output $P_{MPP}$ to the calculated total radiative heat transfer $Q_{RHT}$ to the PV cell ($\eta = (\frac{P_{MPP}}{Q_{RHT}}) \times 100$) is plotted in Fig. 3.8d as a function of gap size and temperature (color bands correspond to efficiencies obtained by calculating $Q_{RHT}$ in a temperature interval of $T_{emitter} \pm \Delta T$, where $\Delta T$ = 27 K for $T_{emitter}$ = 1270 K and 10 K for other temperatures, as described above). Here, $\eta$ increases with temperature, independent of gap size. For example, at 100 nm gaps, an increase in efficiency from 0.5% to 6.8% is observed as the emitter is heated from 810 K to 1270 K. We note that at temperatures >930 K, the efficiency is greater than the highest efficiencies reported in the literature[65-67]. At a given temperature, the efficiency initially decreases with gap size for the smallest gaps, then starts to increase, as predicted by our model (see below).

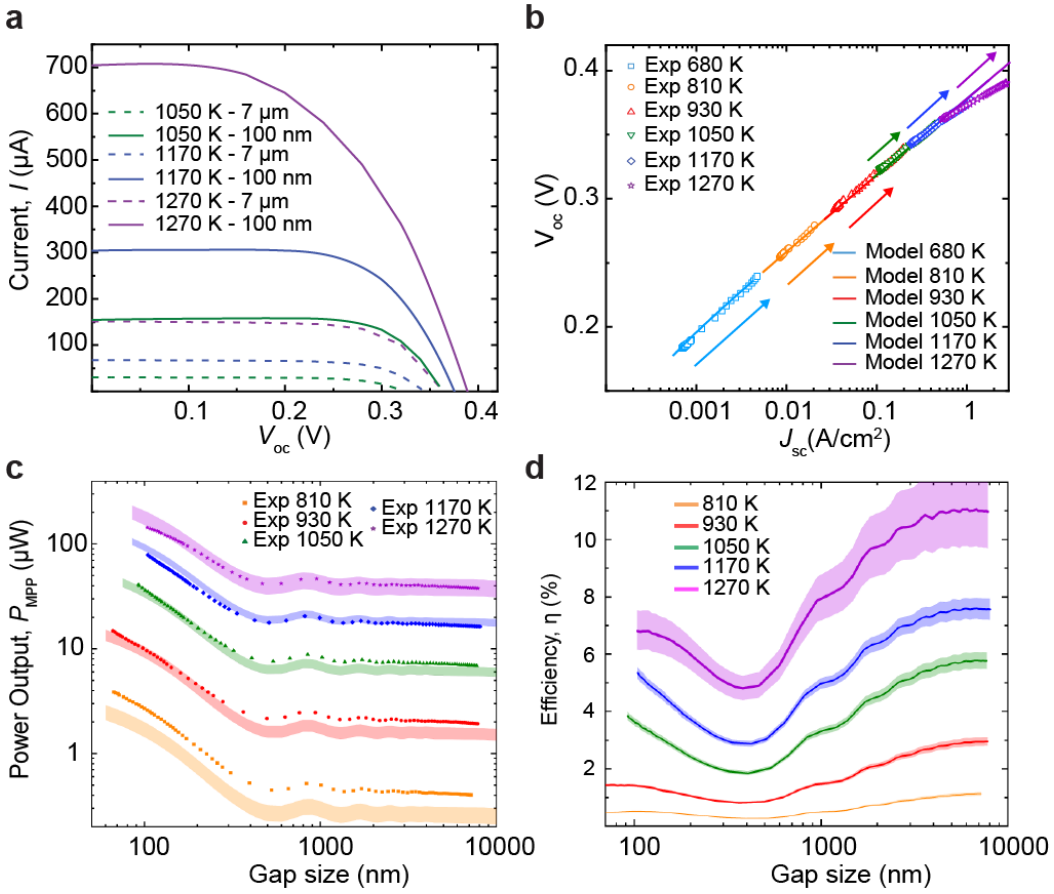


*Figure 3.8 Performance of the thermophotovoltaic system as a function of temperature and gap size.*

*a, Current-voltage (I-V) curves obtained at three emitter temperatures and two gap sizes, indicating an upward shift with increasing temperature and reduced gap size. Dashed lines and solid lines correspond to 7 μm and 100 nm gap sizes respectively. b, $V_{oc}$ (open-circuit voltage) as a function of $J_{sc}$ (defined as short-circuit current ($I_{sc}$) per unit area of the PV cell) obtained from experimental data (various symbols) and calculations (solid lines) at all temperatures. The arrow direction indicates decreasing gap size. At high temperatures there is some overlap in the data sets. c, The experimentally measured power output ($P_{MPP}$) at different temperatures as a function of gap size, indicating power enhancements as the gap size is reduced from 7 μm to 100 nm. The shaded regions indicate the theoretical power output ($P_{MPP}$) based on our model in a temperature range of $T_{emitter} \pm \Delta T$, $\Delta T = 27$ K for $T_{emitter} = 1270$ K and 10 K otherwise. d, The efficiency (η) defined as ratio of $P_{MPP}$ to the calculated total radiative heat transfer ($Q_{RHT}$) at different temperatures of the emitter as a function of gap size. The solid lines correspond to the efficiencies obtained by calculating $Q_{RHT}$ at $T_{emitter}$, while the shaded regions correspond to the efficiencies due to the uncertainty ($\Delta T$) in the measurement of $T_{emitter}$.*

To understand the detailed spectral characteristics of NF energy transfer, we calculate the spectral energy transfer (Fig. 3.9a) from the emitter at 1270 K to the PV cell at 300 K for a range of gap sizes. For example, at a gap size of 100 nm, significant enhancement over the blackbody limit (black dashed line) can be seen in the ABG energy transfer, while considerable suppression of SBG energy transfer below the blackbody limit is observed, due to the incorporation of a thin-

film back reflector (see Methods for comparison with a bulk PV cell). The residual SBG energy transfer has contributions from surface phonon-polaritons in the low frequency range (~14% of $Q_{RHT}$ in 0.0124 - 0.073 eV range) while the rest of the absorption primarily occurs in the Au BSR (~55% of $Q_{RHT}$ in 0.074 - 0.74 eV range). The power generating component of the ABG spectrum absorbed in the active layer ($P_{AL}$) is shaded in orange (~26% of $Q_{RHT}$). Approximately 32% of $P_{AL}$ is extracted as electrical power, while the rest is lost due to thermalization, non-radiative recombination and ohmic losses.

Next, the efficiency trend as a function of gap size can be understood by comparing the spectral energy transfer at three gap sizes of 7 μm (far-field), 400 nm and 100 nm. In the far-field (green line), a large suppression of SBG energy transfer is observed that is related to the thin-film BSR[52, 53]. Even when we reduce the gap size, the SBG energy transfer remains below the blackbody limit. Moreover, as the gap size is reduced from 7 μm to 400 nm, SBG energy transfer is observed to increase more rapidly than ABG energy transfer. These differences in the rates of change of SBG and ABG energy transfer cause an initial drop in the efficiency in Fig. 3.8d at intermediate gaps around 500 nm. As the gap size is further reduced to 100 nm, ABG energy transfer exceeds the blackbody limit, whereas a comparatively smaller rise in SBG energy transfer results in the efficiency increase at smaller gaps.

To further elucidate the contribution of different modes to the observed NF enhancement in $P_{AL}$, we evaluate the transmission coefficients of *s* and *p*-polarization modes ($\tau_s+\tau_p$) as a function of photon energy ($\hbar\omega$ > 0.74 eV) and parallel wavevector ($k$) (Fig. 3.9b). In the far-field at a gap of 7 μm, only propagating modes above the light line in vacuum contribute to ABG energy transfer, whereas in the NF at 100 nm, evanescent modes between the light line in vacuum (green

dashed lines in Fig. 3.9b) and in the top substrate of the PV cell (white dashed lines) also contribute, leading to a broadband enhancement in ABG energy transfer.

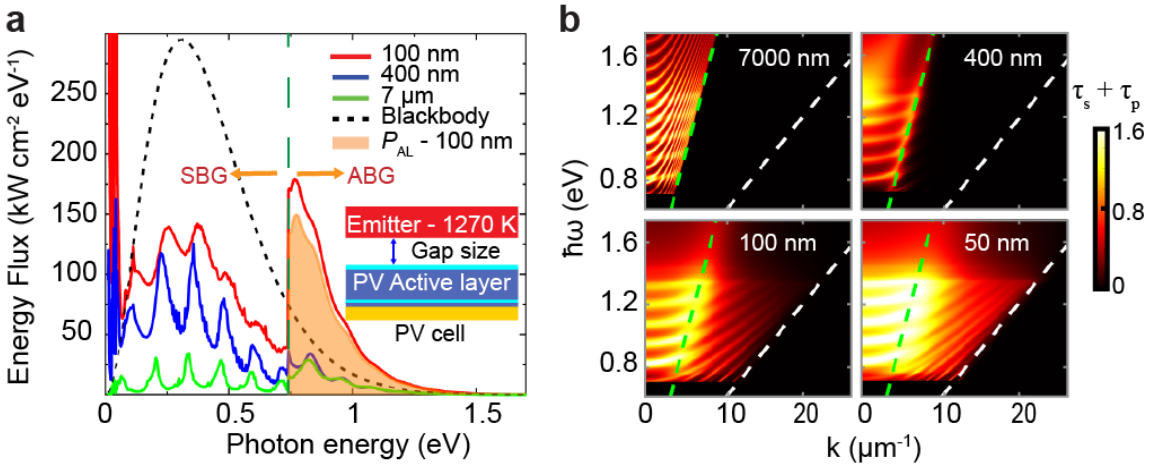


*Figure 3.9 Physical mechanism of NF enhancement.*

*a, The spectral energy transfer from a hot thermal emitter at 1270 K to a photovoltaic (PV) cell at 300 K is plotted as a function of photon energy for three gap sizes. The black dashed line represents the blackbody radiative limit between two semi-infinite plates at 1270 K and 300 K. Enhancement in above-band gap (ABG) transfer is seen as the gap size is reduced down to 100 nm. The orange shaded region represents the radiative energy transfer ($P_{AL}$) from the emitter to the InGaAs active layer, which drives the generation of charge carriers. Green dashed line represents the band gap of the PV cell while SBG represents the sub-band gap region. Note that the energy flux for the 100 nm gap size at low energies (<0.1 eV) extend beyond the y-axis range. b, The total transmission function of different modes from the emitter to the active layer, as a function of photon energy and parallel wavevector at four gap sizes. The green dashed line represents the light line in vacuum, while the white line represents the dispersion relation in the top InP layer.*

The performance of a PV cell under illumination is generally determined by the short-circuit current ($I_{sc}$), open-circuit voltage ($V_{oc}$) and the fill factor (*FF*). While $I_{sc}$ depends on the incident photon flux, the internal quantum efficiency and series resistance (weak dependency due to low series resistance) of the PV cell, $V_{oc}$ and *FF* depend on various factors such as the non-radiative recombination, series and the shunt resistances of the PV cell (see Methods for dark *I-V* characteristics of the PV cell and the variation of *FF*). In our experiments, $I_{sc}$ (Fig. 3.10a) is observed to increase with more-than-linear dependency on temperature at both gap sizes of 100 nm (NF, green circles) and 7 μm (far-field, violet squares). Similarly, the variation of $V_{oc}$ with temperature is plotted in Fig. 3.10b along with the theoretical calculations. The experimental data agree quite well with the theoretical calculations. Specifically, the agreement in $V_{oc}$ with our model

which does not include temperature dependency of the PV cell, indicates that the cell remained close to room temperature during our measurements.

Finally, the power density and efficiency in the far-field (7 μm) and NF (100 nm), respectively, as functions of temperature are shown in Figs. 3.10c and d. A clear enhancement in power density is observed at all temperatures (~7× at 810 K and ~4× at 1270 K). The estimated efficiency from our calculations of $P_{\mathrm{MPP}}$ and $Q_{\mathrm{RHT}}$ is $\eta = (\frac{P_{MPP}}{Q_{RHT}}) \times 100$ ~8.3% (green dashed line), which is slightly higher than the efficiency estimated from the experimental power output (~6.8%). This ~18% disagreement at the highest temperature with the theoretically predicted value may be attributed to uncertainty in temperature measurement of the emitter, modelling parameters, such as the dielectric properties of the emitter as a function of temperature and the PV cell's series and shunt resistances or a small increase in the temperature of the PV cell. The efficiencies in the NF are slightly smaller than in the far-field, owing to absorption in the Au film reflector, which can be mitigated by engineering the devices to further suppress SBG energy transfer. This can be achieved by employing an air-gap PV cell which has recently been shown to support very efficient SBG suppression[53]. Such devices must be engineered to address a host of technical requirements (smooth surfaces, planarity, temperature compatibility) before they can be adapted for NFTPV studies.

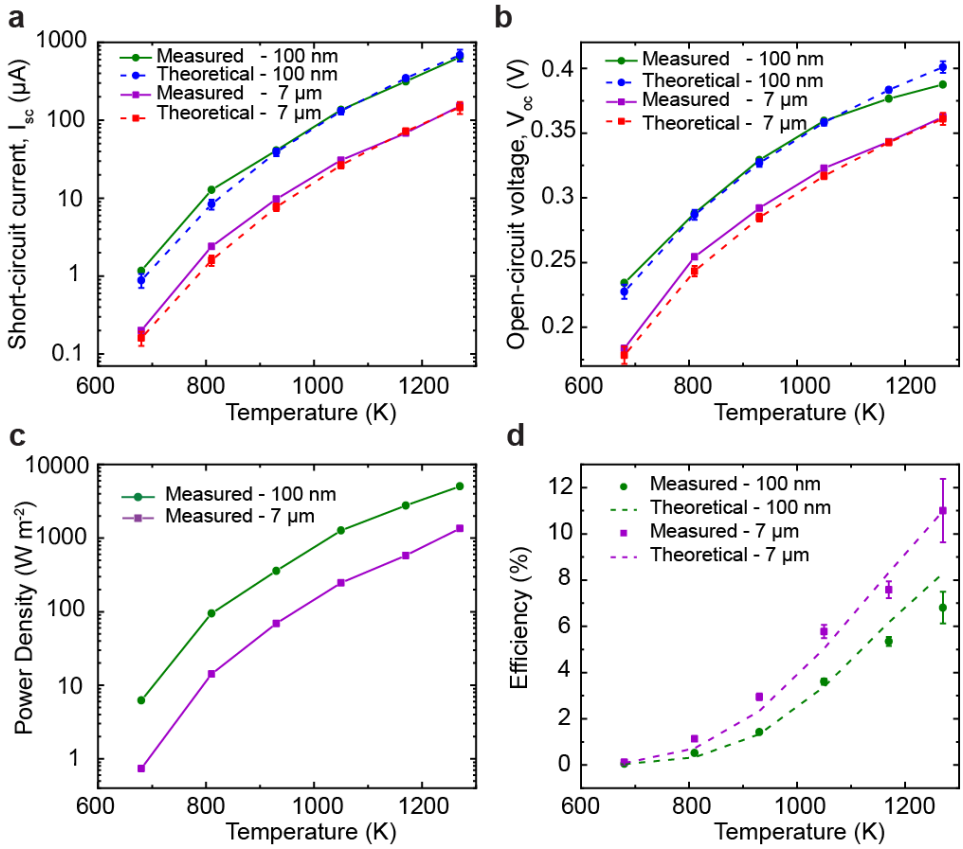


*Figure 3.10 Performance of near-field thermophotovoltaic system (NFTPV).*

*a, b, Measured and calculated short-circuit current ($I_{sc}$) and open-circuit voltage ($V_{oc}$) as a function of temperature. Green circles and violet squares represent the experimental data points, while blue circles and red squares represent the calculated data points with the corresponding uncertainties, at gap sizes of 100 nm and 7 μm respectively. Solid and dashed lines added as a guide to the eye. c, The measured power density ($P_{MPP}$ per unit area of the PV cell) is plotted as a function of temperature at two gap sizes, one in the far-field (violet squares) and other in the near-field (green circles, solid lines plotted as visual guide). d, Efficiency of NFTPV system at different temperatures for two gap sizes, defined as the ratio of the measured power output ($P_{MPP}$) and theoretical radiative heat transfer ($Q_{RHT}$), calculated at $T_{emitter}$ with an uncertainty of $\pm \Delta T$, where $\Delta T = 27$ K for $T_{emitter} = 1270$ K and 10 K otherwise. The dashed lines represent theoretical estimates of the efficiency based on our model.*

## 3.6 Methods

### Device geometry and electrical setup

The thermal emitter and the PV cell were custom-fabricated using standard micro-fabrication and MBE techniques. The emitter is a cantilevered structure that features a large planar island suspended from the substrate through two beams. Silicon was chosen as the emitter material due to its ease of micro-fabrication and compatibility with other thin-film material growth

processes such as ITO, TiN, AlN etc. The heavily doped (~$3\times10^{19}$ $cm^{-3}$ B-doped) Si emitter allowed us to reliably heat the emitter in a large temperature range. The suspended island consists of a 150 µm diameter 'mesa' region and a 190 µm diameter 'rec' region, which is recessed from the mesa to a depth of 15 µm (Fig. 3.6b). The beams are each 20 µm wide, 270 µm long and 45 µm deep, resulting in a typical thermal conductance of $G_{beam}$ = 400 µW $K^{-1}$, stiffness of ~2 kN $m^{-1}$ in the 800 - 1300 K temperature range and a resistance of $R_{emitter}$ = 80 Ω. The two beams are electrically isolated from the substrate via a buried oxide layer (labeled BOX in Fig. 3.6d). A bipolar voltage ($V$) is applied across the two beams using an Agilent E3631A DC power supply and the current was monitored through an Agilent 34401A multimeter (Fig. 3.6a). The PV cell comprises of a (100 / 100 / 1000 / 200 nm) $1\times10^{18}$ $cm^{-3}$ $n^+$ InGaAs / $1\times10^{18}$ $cm^{-3}$ $n^+$ InP / $1\times10^{17}$ $cm^{-3}$ n InGaAs ($E_g$ ~ 0.75 eV) / $1\times10^{18}$ $cm^{-3}$ $p^+$ InP heterostructure, which is epitaxially transferred to a 500 µm thick Si handle wafer coated with 2 µm of Parylene-C and a 400 nm Au bottom contact (Fig. 3.6c). The device has a 250 µm diameter of which a 190 µm diameter region enclosed by a 20 µm circular Au contact is available for measurement (Fig. 3.6c, 3.6e). The PV cell sidewalls and the bottom contact Au surface are coated with 1 µm thick PI-2555 for insulation. Finally, the *I-V* characteristics of the PV cell are measured using a Keithley 2401 sourcemeter (SM in Fig. 3.6a) between the top and the bottom contacts.

**Parallelization of the devices**

Our custom-built nanopositioner allows lateral alignment of the devices with an accuracy of a few micrometers along the *x*- and *y*-directions (see Fig. 3.6a where the directions are shown), and ~6 µrad of angular alignment about both the axes. The parallelization is achieved in a two-step process. First, coarse alignment is accomplished by imaging the chip surface (~1 cm × 1 cm in size) that has the PV cell integrated, using a 50× microscope objective (Zeiss LD EC Epiplan-

Neofluar 50× / 0.55 HD) with a shallow depth of focus of 2 μm. The tip/tilt of the PV chip is then manually adjusted, while translating the chip along *x* and *y* directions, to bring the whole chip into focus. Thus, the angular deviation of the PV chip is less than ~200 μrad and consequently the deviation from parallelism across the PV cell surface is less than 40 nm. This tip/tilt process is repeated on the emitter (placed at a safe distance above the PV cell) using a goniometer integrated into our nanopositioner, resulting in a similar deviation across the mesa surface. Thus, in the first coarse-positioning step, the devices are parallelized with a deviation of ~80 nm across the surfaces of the devices. The whole assembly is then moved into a vacuum chamber (~1 μTorr). Upon heating the emitter to a desired temperature, the alignment may be impacted by thermal effects. Therefore, we perform a second *in-situ* parallelization step after heating the emitter to high temperatures, by using the integrated goniometer. To perform this step, we take advantage of the fact that energy transfer from the emitter to the PV cell is maximized when the devices are perfectly parallel. Specifically, we first reduce the gap size between the emitter and the PV cell until contact is made, record the $P_{MPP}$ at the smallest gap size and withdraw the PV cell by 10 μm. The tip/tilt of the emitter is then adjusted in steps of ~100 μrad and the approach to nanogaps and contact is repeated to maximize the measured $P_{MPP}$. Following this iterative second alignment procedure, we estimate a maximum deviation from parallelism of ~15 nm across the 150 μm mesa.

**Detecting contact between the emitter and the PV cell**

To detect mechanical contact between the emitter and the PV cell, we employ a scheme similar to the optical scheme used in atomic force microscopes. Specifically, we focus a laser onto the backside of the emitter and collect the reflected laser beam (schematic in panel 2 of Fig. 3.7a) on a segmented photodiode with two independent detectors. Further, a small AC signal $V_{AC}$ is applied to the piezoactuator which modulates the gap size between the emitter and the PV cell at

an amplitude of ~2 nm at 4 kHz. The 4 kHz component of the difference signal of the two segments in the photodiode ($Opt_{AC}$) is continuously measured in a lock-in amplifier (SRS 830). When the PV cell makes physical contact with the emitter, a change in this signal can be noticed indicating contact (see panel 2 of Fig. 3.7a). In addition, sudden changes in the simultaneously measured $R_{emitter}$ due to rapid cooling through heat conduction to the PV cell enables us to independently detect contact (Fig. 3.7a).

**Estimation of emitter temperature**

The temperature of the emitter $T_{emitter}$ for various power dissipations ($P_{Joule}$) was measured using an ultra-high vacuum scanning thermal microscopy (UHV-SThM) technique. The emitter is loaded into the UHV chamber (UHV 750) of an RHK SPM (SPM 1000) and heated by supplying a known power, (e.g. 411.8 mW). Subsequently, a SThM probe with an embedded temperature sensor is brought into contact with the hot emitter and the temperature of the probe and the probe-sample thermal contact resistance are measured (see ref.[102]), which enable us to directly estimate the temperature of the emitter. This measurement of $T_{emitter}$ is repeated for various values of $P_{Joule}$ from which the temperatures described in Fig. 3.8c are obtained. The uncertainty of this temperature measurement is shown in Fig. 3.17d. Since the uncertainties associated with our measurements are different across temperatures, we use an uncertainty of ±27 K for the highest temperature and an upper bound of ±10 K for all other temperatures in estimating the uncertainty bands in Figs. 3.8c and 3.8d.

**Modeling approach for calculating NF radiative energy transfer**

To model the power output and calculate the total radiative energy transfer between the emitter and the PV cell, we first approximate our devices as infinitely extended in the lateral $x$, $y$ dimensions and multi-layered along the $z$ direction (see Fig. 3.6a for directions). The thermal

emission from each layer is generated by fluctuational currents within that material. The correlations of these fluctuational currents are described by fluctuation-dissipation theorem[5, 6] and the resulting energy flux in any layer of the structure is calculated using a numerically-stable scattering matrix formulation[103]. Using this method, we calculate $Q_{RHT}$ from different layers of the emitter to the PV cell. To estimate the $P_{MPP}$, we first calculate the spectral photon flux from the emitter to the active layer of the PV cell. The photocurrent generated from this photon flux is incorporated in an equation describing the PV cell and the maximum power $P_{MPP}$ is obtained from the corresponding *I-V* characteristics. A detailed description of this model can be found in subsequent sections.

**Fabrication of the suspended thermal emitter**

A schematic diagram of the fabrication process for the emitter device is shown in Fig. 3.11a. (Step 1) A commercially available 4" SOI wafer (Ultrasil LLC) with a heavily doped (P-type B-doped) device layer and a thickness of 60 ± 1 μm is chosen. The specified resistivity of the top device layer is <0.005 Ω.cm, which corresponds to a doping level ~3 × 1019 cm-3. The handle layer is undoped with a thickness of 500 ± 10 μm. The oxide layer thickness between the device layer and the handle layer is 2 μm ± 5%, which acts as an etch stop for fabricating the suspended emitter. (Step 2) The top surface is patterned using standard lithographic techniques to define the mesa surface. This pattern is etched to a depth of 15 μm in a deep reactive ion etching (DRIE) tool. (Step 3) A three-layer metal contact pad (Ti/Pt/Au – 10/30/200 nm) is evaporated and lifted-off to form electrical contacts to the two legs of the emitter. The wafer is then lithographically patterned and etched (~45 μm deep) in a DRIE tool until the BOX layer is reached. This step defines the beam structures and isolates the two electrical contacts. (Step 4)

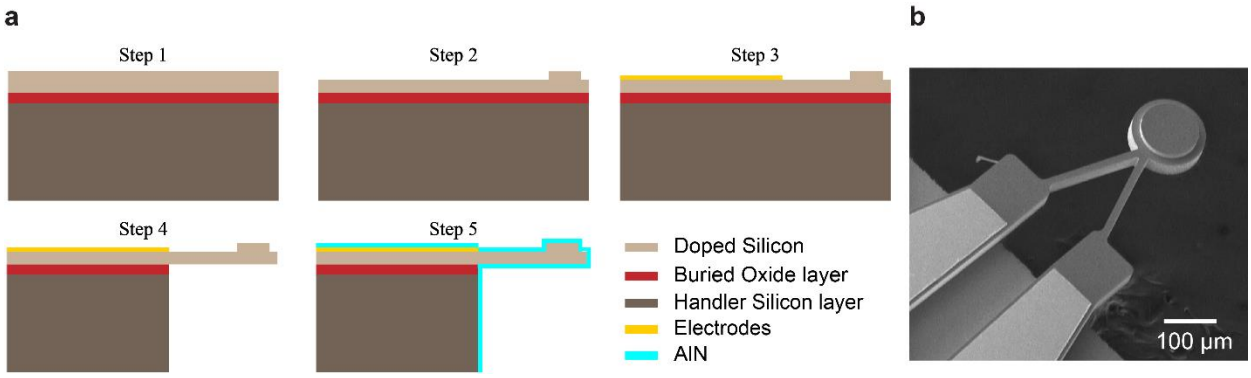


*Figure 3.11 Fabrication process for the suspended silicon emitter.*

*a, Steps followed to suspend silicon emitter from two isolated beams. b, Scanning electron micrograph of the fabricated structure.*

Next, we proceed to release the emitter device to form a suspended structure. The front-side of the wafer is first coated with a thick photoresist (AZ-9260) for protection. The backside is subsequently coated with a thick photoresist (10 µm) and patterned to expose windows for etching. The exposed silicon undergoes a through-etch (DRIE – 500 µm deep) process until the stop BOX layer is reached. The residual BOX layer is then etched using a recipe that selectively etches silicon dioxide, resulting in a suspended monolithic silicon emitter. Next, the released chips are thoroughly cleaned in hot Piranha to remove any organic contaminants while retaining the smoothness of the mesa surface. (Step 5) A 10 nm-thick layer of aluminum nitride (AlN) is coated using an atomic layer deposition (ALD) tool. In Fig. 3.11b we show a SEM image of a fabricated silicon emitter device, suspended from the base through two silicon beams.

**Fabrication of the InGaAs photovoltaic cell**

A schematic diagram of the fabrication process for the PV cell is shown in Fig. 3.12. (Step 1) The PV cell fabrication starts with the epitaxial growth of a lattice-matched, inverted *P-n-N* heterostructure on a 2 inch, 350 µm thick, single-side polished, Zn-doped, (100) InP substrate using a GENxplore Molecular Beam Epitaxy system (Veeco Corp.). The structure comprises of a 200 nm undoped InP buffer layer, 200 nm Be-doped ($1 \times 10^{18}$ $cm^{-3}$) $In_{0.53}Ga_{0.47}As$ (InGaAs) top

contact layer, 200 nm Be-doped ($1 \times 10^{18}$ $cm^{-3}$) InP front window layer, 1 μm Si-doped ($1 \times 10^{17}$ $cm^{-3}$) InGaAs absorption layer, 100 nm Si-doped ($1 \times 10^{18}$ $cm^{-3}$) InP back window layer and 100 nm Si-doped ($1 \times 10^{18}$ $cm^{-3}$) InGaAs bottom contact layer. (Step 2) The PV structure is rinsed in buffered HF (BHF) for 90 s, followed by deposition of an Au/Parylene-C (400/1000 nm) bottom contact and bonding layer via sputtering and physical vapor deposition. Subsequently, the wafer is bonded, via thermal compression bonding (150˚ C, 500 kPa, 5 min) onto a 500 μm Si handle coated with 1 μm Parylene-C. (Step 3) The Si/Parylene/Au/PV/InP stack is submerged in HCl: $H_2O$ (1:1) solution with Si handle facing down for 24 hrs, to remove InP substrate. After removal of the InP substrate, the top surface of the PV device was immediately cleaned using $NH_4OH$ brushing and megasonic cleaning. (Step 4) The PV mesa is defined using standard photolithography and wet etching. Citric acid: $H_2O_2$ (4:1) and HCl: H2O (1:1) solutions are used for etching the InGaAs and InP layers, respectively. (Step 5) The Ti/Pt/Au (10/30/1000 nm) top contact layer is patterned via standard photolithography and electron beam deposition. (Step 6) A polyimide insulating layer (PI-2555) was spin-coated and annealed at 200°C for an hour, and then patterned via standard lithography and RIE plasma etching to define the device active area and bottom contact pad openings. (Step 7) The Ti/Au (5/1000 nm) top contact pad is patterned via standard photolithography and electron beam deposition. Finally, the top InGaAs contact layer is etched using a citric acid: $H_2O_2$ (4:1) solution to expose the active area of the PV cell and prevent parasitic absorption.

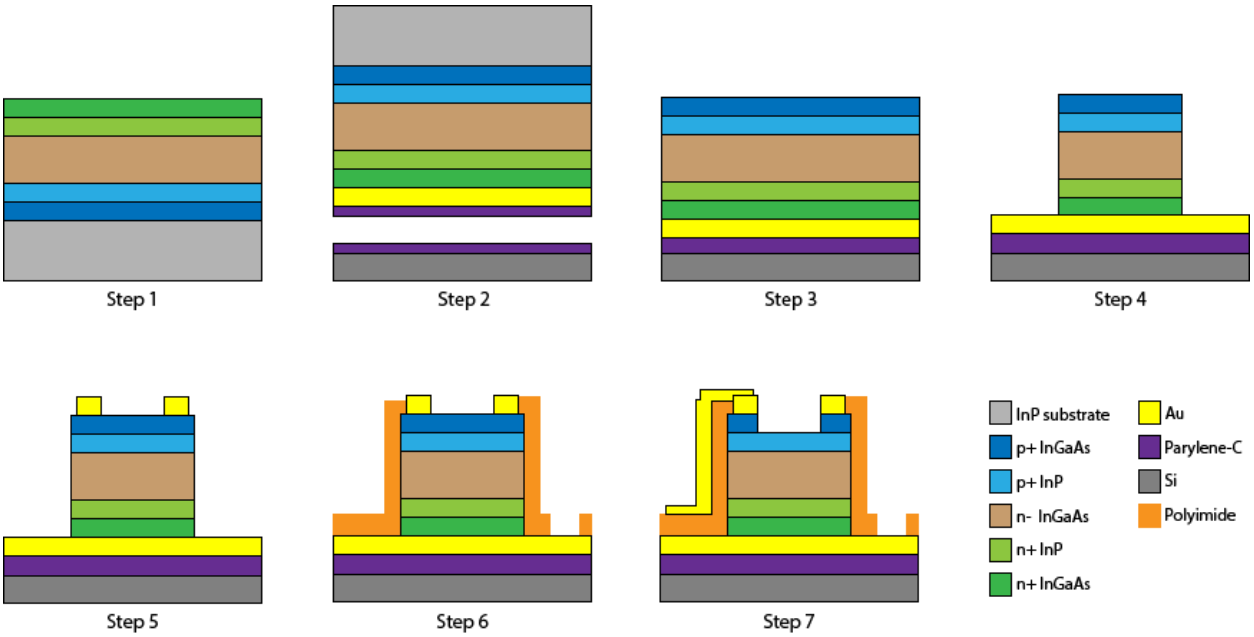


*Figure 3.12 Fabrication process for the InGaAs PV cell.*

*The various steps involved in the fabrication of the PV cell are illustrated.*

**Thermal and mechanical modelling of silicon emitter and quantification of heat loss through various pathways**

*Thermal characteristics*

To understand the thermal and mechanical characteristics of the emitter at high temperatures, we performed FEM analysis, using COMSOL Multiphysics, on the structure shown in Fig. 3.13a. Specifically, we employed the heat transfer, solid mechanics, electric currents and surface-to-surface radiation modules, which were coupled to the physics modules of thermal expansion and electromagnetic heating by using the relevant boundary conditions. In the heat transfer module, a constant temperature (300 K) condition was applied on surfaces A and B (see Fig. 3.13a). Bipolar voltages of $V$+(~3.75) and $V$–(~-3.75 V) were also applied on surfaces A and B respectively, which were then used to solve for the resulting currents to determine the Joule heating in the electromagnetic heating module. To account for the radiative coupling to the environment, a nominal emissivity of 0.7 is applied on all the surfaces of the emitter, while the

environmental temperature was set to 300 K. The thermal conductivity of silicon as a function of temperature was approximated from that of bulk intrinsic silicon as described in ref.[104]. Fig. 3.13b shows the resulting temperature rise (color scale in kelvin) in the emitter structure, with the mesa being at the highest temperature of 1292 K. The distributed Joule heating in the beams results in a temperature gradient that is nearly exclusively spread along the length of the beams, while the mesa surface is seen to be isothermal with less than 4 K temperature change along the two lines shown in Fig. 3.13b. A transient thermal analysis was performed on the structure to estimate the time constant of the emitter. The temperature change with respect to time is shown in Fig. 3.13c, indicating that the thermal time constant is ~20 ms. We note that all the near-field measurements were carried out after allowing for a thermal stabilization time of at least 3 s.

An important consideration in the design of thermal emitters is the possible distortion of the emitter due to thermal expansion and bi-material effects. We note that by suspending a monolithic silicon emitter, instead of creating a doubly clamped structure; we reduce potential bending and buckling effects. In Fig. 3.13d, we show the computed absolute displacements for an emitter heated to 1292 K. Thermal expansion occurs predominantly in the direction along the length of the beams with a maximum displacement of ~1 μm at the distal end of the cantilever (Fig. 3.13d) and the mesa surface is expected to remain flat at all temperatures. We note that, for simplifying the simulations, we did not consider the temperature-dependence of resistivity and emissivity of doped silicon in this simulation, but this simplification is not expected to affect any of our conclusions.

Finally, we note that the heat dissipated in the beams is lost through conduction along the beams and radiation from all the surfaces to the surroundings. The contribution of different pathways is affected by the temperature and the gap size. For example, at $T_{\text{emitter}}$ = 1270 K achieved

by dissipating 550 mW in the emitter and a gap size of 100 nm, the total radiative heat from the surfaces facing the PV cell is 2 mW (0.4%) and from the backside and the side walls of the emitter is ~10 mW (1.8%). The major heat pathway is through conductance along the beams of 537 mW (98%).

*Mechanical stiffness*

To precisely maintain the gap size between large planar surfaces, it is important to design a stiff cantilever to minimize deflections at the smallest gap sizes and avoid snap-in (for example due to electrostatic attraction) at nanometer-scale gap sizes. Our emitter consists of a large circular island suspended by two beams, each 20 μm wide, 270 μm long and 45 μm deep. The resulting stiffness of the emitter as a function of temperature was also calculated using a FEM model similar to that described in the previous section. The temperature-dependent elastic modulus ($E$) of silicon is estimated from the semi-empirical formula obtained from ref.[105].

$$E(T) = E_0 - BTe^{-T_0/T} \tag{3-3}$$

Here, $T$ is the temperature of silicon, $E_0$ = 167.5 GPa is the elastic modulus at 0 K, $B$ = 15.8 MPa $K^{-1}$ and $T_0$ = 317 K are the fitting parameters[105]. A constant force, $F$ = 10 mN, was applied on mesa normal to the surface (Fig. 3.13a), while the emitter is heated, using the model described in the previous section, by applying a voltage $V$ that is varied from 1.5 V to 3.9 V in steps of 0.1 V. The resulting displacement ($\delta$) at point 'A' (Fig. 3.13e) is monitored at these temperatures and the stiffness is calculated as $k = F/\delta$ (Fig. 3.13f). This was found to be ~2.15 kN/m at 800 K and reduced by ~5% as the temperature is increased to 1300 K.

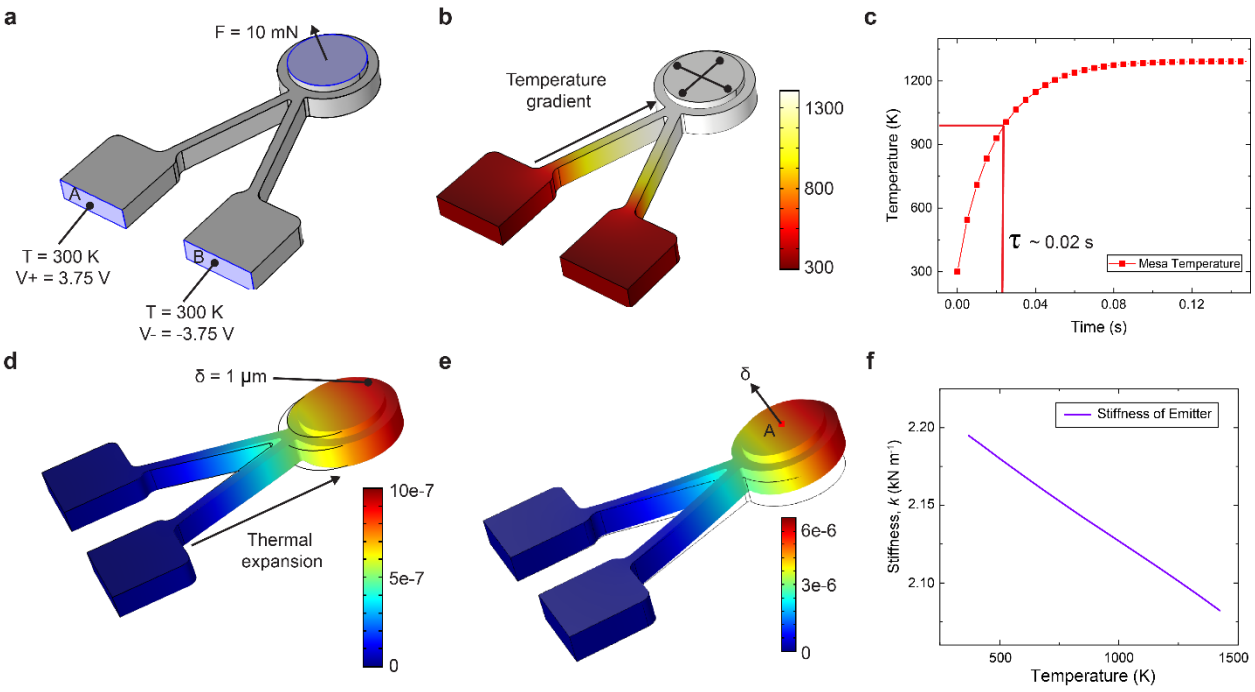


*Figure 3.13 Thermal and mechanical characteristics of the emitter.*

*a, Boundary conditions applied for the FEA analysis. b, Temperature distribution on the emitter when heated by joule heating to 1292 K (scale bar in K). c, Temporal response of the emitter showing a thermal time constant of 20 ms. d, Thermal expansion of the emitter (color bar in m). e, The displacement, at point 'A' on the surface, resulting from a force F = 10 mN, applied on mesa surface as shown in Fig. 3.13a. f, Stiffness of the emitter as a function of temperature.*

## Electro-thermal characteristics of emitter

In this study, controlled heating of the emitter is achieved by employing heavily-doped silicon (~$3 \times 10^{19}$ $cm^{-3}$) as the resistive material. The electrical circuit used in this study involves applying a bipolar voltage using a DC power supply and measuring the electrical current through the circuit using a multimeter, as shown in the inset of Fig. 3.14a. In Fig. 3.14a, we plot the resistance of the emitter as a function of the power dissipated, while the corresponding temperature of the emitter is plotted on the secondary axis. An initial increase in the resistance of the doped silicon is observed when the emitter is heated, with the resistance reaching a maximum at ~1200 K, beyond which it starts to decline. This trend can be understood by considering the temperature-dependent electrical resistivity ($\rho(T)$) of doped silicon as $\frac{1}{n(T)e\mu(T)}$, where $n(T)$ is the temperature-

dependent number of charge carriers, $e$ is the elementary charge and $\mu(T)$ is the temperature-dependent charge carrier mobility. At relatively low temperatures, $\rho(T)$ is dominated by the temperature dependency of carrier mobility ($\mu(T)$) which decreases with increasing temperature[106]. As the temperature is increased, the number of thermally generated intrinsic carriers ($n(T)$) increases significantly[107], causing $\rho(T)$ to drop with temperature. Such a behavior, called thermal runaway, is observed in doped silicon resistors as described in ref.[107]. An additional observation is that the resistance curve displays hysteresis after few hours of operation at high temperatures, and thus, it is not feasible to use the resistance as an indicator of temperature, instead, we measure the temperature in an independent experiment.

To reduce the electrostatic forces between the parallel plates of the emitter and PV cell during the near-field approach, we apply a bipolar voltage across the device bringing the mesa potential close to ground. To test the effectiveness of this approach, we fabricated a few 3-terminal devices and tested them in representative conditions. In Fig. 3.14b two examples are shown, one by applying a bipolar voltage (case a) and the other by passing current (case b) from a Keithley 6220 current source (insets of Fig. 3.14a) through the two outer terminals of the device, while monitoring the voltage ($V_{\mathrm{Mon}}$) on the mesa with the third terminal in the center. It can be seen that for case a, $V_{\mathrm{Mon}}$ remains close to zero potential while a continuous increase is seen for case b, indicating that the higher electrostatic force for case b could lead to snap-in of the devices at higher gap sizes than that for case a.

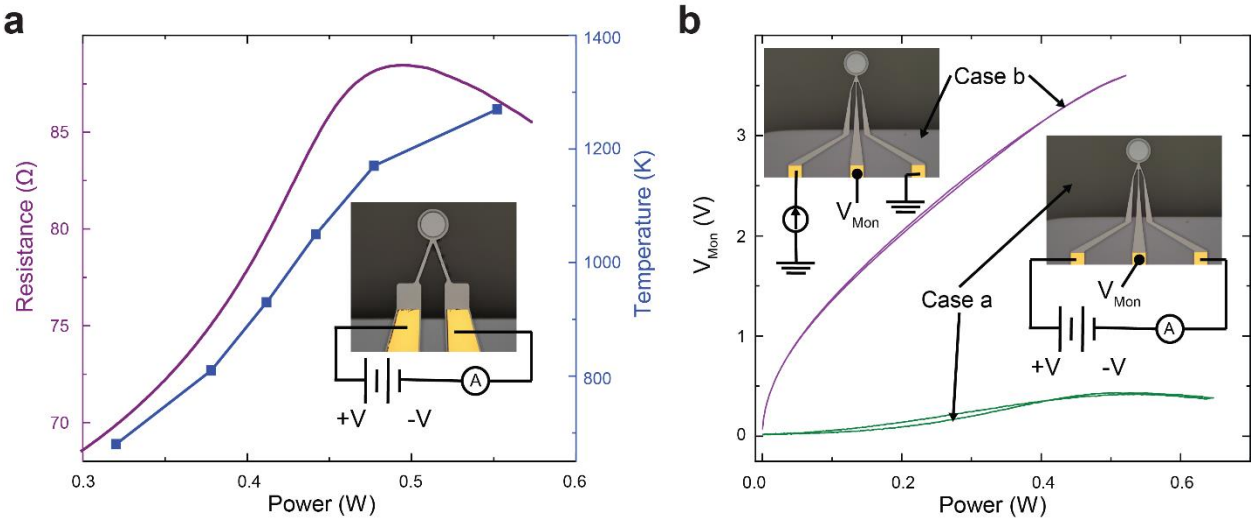


*Figure 3.14 Electro-thermal characteristics of the emitter.*

*a, Resistance (violet solid line, left axis) and experimentally measured temperature (blue squares, data points connected by a straight line, right axis), as a function of the power dissipated in the emitter. Inset shows the electrical connections b, Measured voltage of the mesa ($V_{Mon}$) as a function of power dissipation in a representative 3-terminal device for two cases (bipolar and unipolar heating).*

**Thermal modelling to determine temperature rise of the PV cell**

In our experiments, the PV cell is mounted on the bottom assembly of our custom-built nanopositioner as shown in Fig. 3.15a. As can be seen, the PV cell substrate (10 × 8 × 0.5 mm, red square) is mounted on a DIP chip carrier (shown in yellow, 'B') with silver paste which in-turn is attached to an aluminum platform. From a simple one-dimensional thermal model, we estimate the thermal conductances from point 'A' to point 'F' (a large heat-sink at ambient temperature). The smallest thermal conductance is between point 'A' to point 'B'. In other words, the thermal resistance is dominated by the structure shown in Fig. 3.15b. In order to identify the temperature rise of the PV cell due to the heat transfer from the emitter, we then performed FEM analysis, solving the thermal conduction equation for a representative PV cell when it is illuminated by the hot emitter. Fig. 3.12b shows the simulated structure consisting of a thick silicon substrate (0.4 × 0.4 × 0.2 mm). Thin layers of parylene (2 μm), gold (400 nm), GaAs (1.5 μm) and gold (1 μm) are included to represent a realistic model of the PV cell consistent with the

description above. The bottom surface is maintained at a constant temperature of 300 K, while heat ($Q_{input}$) is applied on the top surface of the PV cell at its center. The corresponding temperature rise ($\Delta T_{PV}$) is calculated for different inputs of heat (Fig. 3.12a). The estimated radiative heat transfer ($Q_{RHT}$) to the PV cell at the highest temperature (1270 K) achieved in this work and a gap of 100 nm, is ~2 mW. Thus, based on this analysis the temperature rises of the PV cell in the experiments performed in this study are expected to be less than 1 K. We note that in the real experiments, the PV cell may be heated to a slightly higher temperature (~5 K), possibly due to heat emission from the beams of the emitter which is not considered in the calculation of $Q_{RHT}$ and interfacial thermal resistances in the multilayers of the PV cell that are also not included in the simulation.

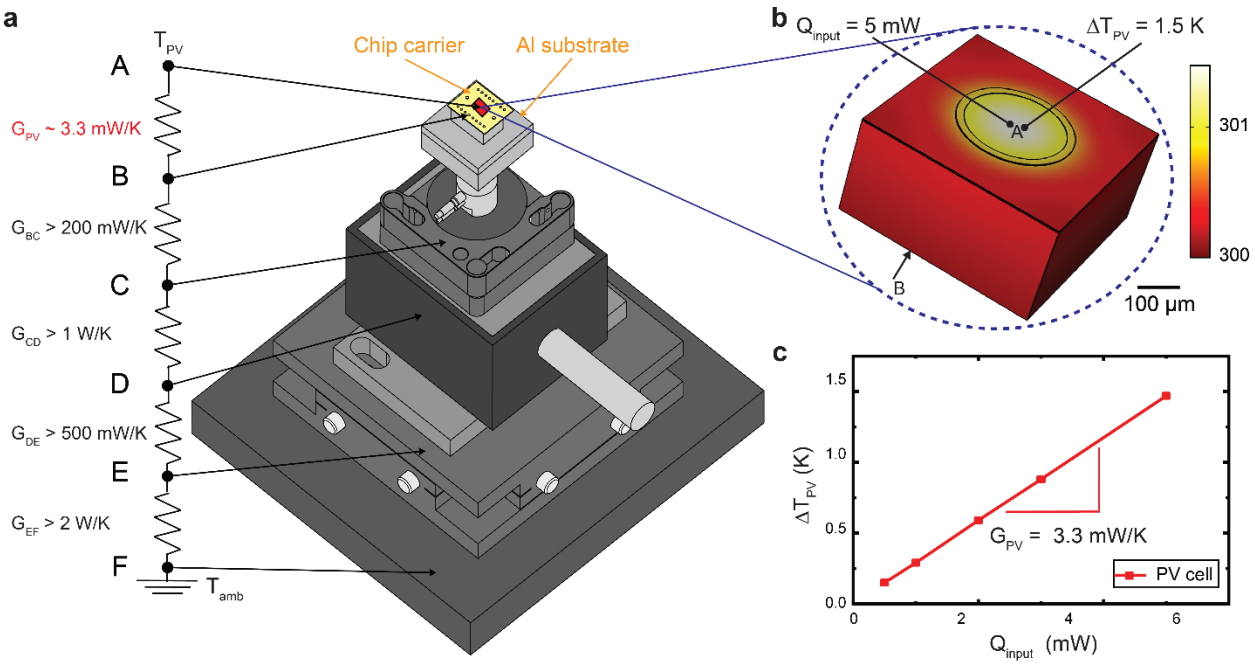


*Figure 3.15 Thermal management of PV cell.*

*a, Schematic of the bottom assembly of the nanopositioner onto which the PV cell is mounted. Typical thermal conductances along different sections of this assembly are shown. b, Boundary conditions applied for FEA of the temperature distribution of the PV cell due to heat transfer from the mesa of the emitter to the PV cell. c, Temperature increase at point 'A' (Supplementary Fig. 5a) at the center of the top surface of the PV cell, as a function of heat input to the PV cell.*

## Emitter Temperature Measurement via Scanning Thermal Microscopy

The temperature of the emitter as a function of dissipated power was measured on the same device after the near-field experiments were performed, using a quantitative high-temperature scanning thermal microscopy (SThM) technique in an ultra-high vacuum environment following an approach described in ref.[102]. Briefly, a custom-fabricated SThM probe with an integrated Pt serpentine resistor that serves both as a heater and thermometer was used for these measurements. The temperature at the probe's tip ($T_{\text{tip}}$) can be accurately quantified with the Pt thermometer. Further, the same Pt resistor can be used to simultaneously heat the probe tip by inputting heat ($\dot{q}_{tip}$) into the tip. In our measurements the probe was placed close to the center of the emitter's mesa but at a distance of ~5 μm above the surface, with the orientation shown in Fig. 3.16a. Then the probe was moved towards the mesa to contact the emitter. The thermal behavior of the resulting structure can be represented by the DC equivalent thermal circuit shown in Fig. 3.16b, where $R_{\text{C}}$ and $R_{\text{TS}}$ are the cantilever thermal resistance and tip-sample thermal contact resistance, respectively. Given the value of $R_{\text{TS}}$, the surface temperature ($T_{\text{s}}$) can be calculated based on the measurement of $T_{\text{tip}}$ using

$$T_S = \frac{R_{TS}}{R_C}\left(T_{tip-contact} - T_{tip-retract}\right) + T_{tip-contact} \tag{3-4}$$

where $T_{\text{tip-retract}}$ and $T_{\text{tip-contact}}$ refer to SThM tip temperatures when retracted (out of contact) and when in contact with the mesa. We note that upon contact of the probe and emitter, an additional heat transfer path is provided by which the emitter's temperature is reduced. However, this decrease is less than 0.4% of the total temperature rise of the emitter due to the significantly larger thermal resistance of the additional path ($R_{\text{TS}}$ + $R_{\text{C}}$) compared to the thermal resistance of the emitter. Hence this effect can be neglected.

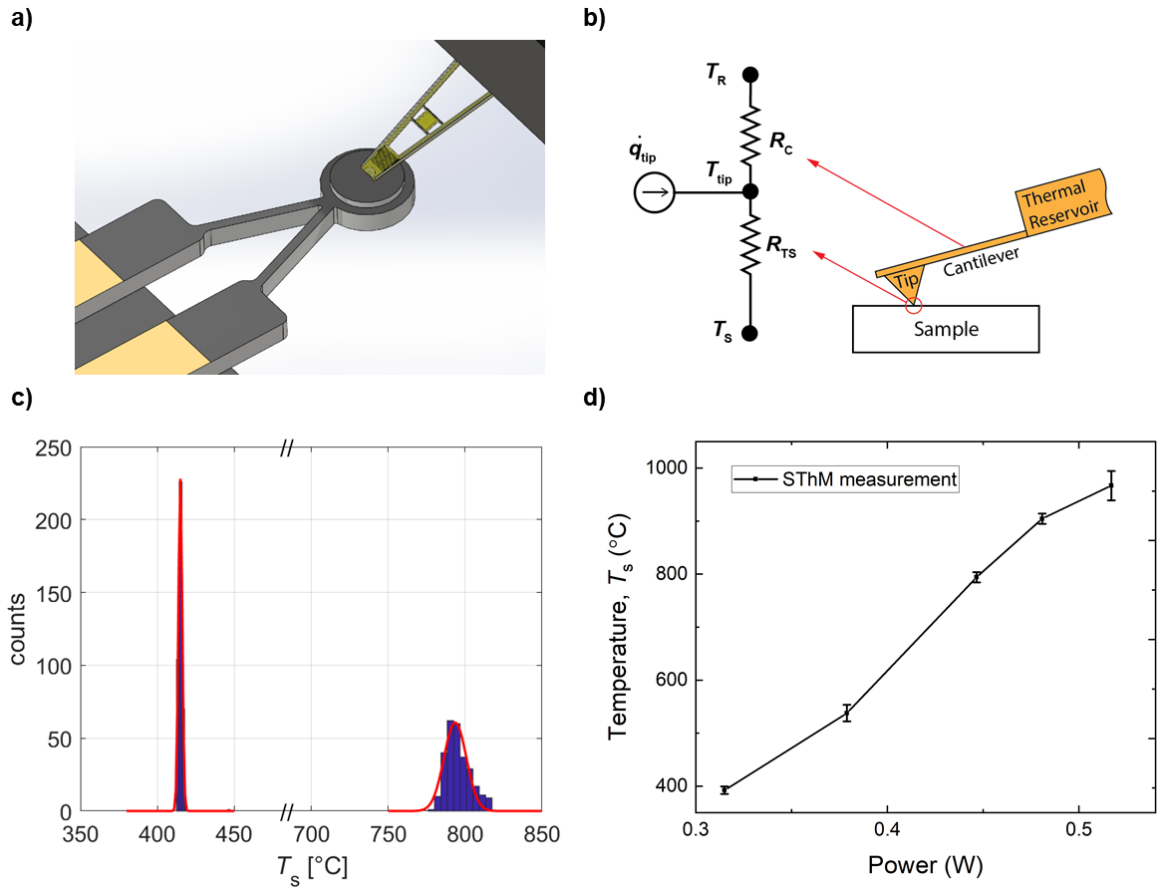


*Figure 3.16 Temperature measurement of emitter using SThM.*

*(a) Schematic of the SThM measurement orientation on the emitter mesa. (b) DC-equivalent thermal resistance network of the SThM probe in contact with a sample, and (c) histograms of surface temperature measurement using SThM at two different emitter powers of 0.314 W and 0.45 W showing mean temperature values of 414.8 °C and 794.1 °C and the standard deviation in the data is 1.6 K and 9.7 K, respectively. (d) Mean value of the emitter surface temperature as a function of dissipated power, error bars correspond to ±1σ (standard deviation).*

The contact resistance ($R_{TS}$) depends on the topography and local mechanical and thermal properties of the tip and contact point, therefore it typically varies from one measurement to another and can also change over time due to the mechanical drift of the SThM probe. For quantification of $R_{TS}$, we employed a DC + AC temperature measurement scheme (see ref.[102] for details) by applying a modulated heating power to the tip heater ($\dot{q}_{tip}$) at a frequency $f_h$ = 4 Hz, and measuring both the DC tip temperature, and AC tip temperature amplitude at $f_h$. The change in the AC temperature amplitude when the probe is in contact compared to out of contact provides

direct information about the value of $R_{TS}$ based on a single-state dynamic thermal model[102]. Fig. 3.16c shows the histogram of two measurements for an emitter that dissipated powers of 0.314 W and 0.45 W, showing mean temperatures of 414.8 °C and 794.1 °C respectively. As can be seen, the measurement uncertainty increases at higher temperatures, because it is more difficult to achieve a stable contact at elevated temperatures. Finally, the mean value of emitter surface temperature as a function of emitter power is shown in Fig. 3.16d. The non-monotonic increase in temperature with power may be attributed to increasing radiative coupling to the environment at higher temperatures and due to the temperature and position-dependent changes in material properties such as resistivity along the beams.

**Modelling of the NF-TPV system**

As described in the methods section of the main manuscript, our theoretical modelling involves calculating the radiative energy transfer between the emitter and the PV cell, and further estimating $P_{MPP}$ from a PV cell model. We begin by describing our approach to modelling the spectral energy transfer.

*Modelling Radiative Energy Transfer*

The geometry and composition of the emitter and the PV cell used for modelling the radiative energy transfer are shown in Fig. 3.17a. First, we model the permittivity of n-InGaAs by combining the intrinsic optical response of pure InGaAs, and free carrier absorption due to doping as:

$$\epsilon_{n-InGaAs}(\omega) = \epsilon_{InGaAs}(\omega), \text{ when } \omega \geq \omega_g \tag{3-5}$$

$$\epsilon_{n-InGaAs}(\omega) = \epsilon_{InGaAs}(\omega) + \epsilon_{Drude}(\omega), \text{ when } \omega < \omega_g, \tag{3-6}$$

where $\omega_g$ is the angular frequency corresponding to the bandgap of InGaAs.

For $\epsilon_{InGaAs}(\omega)$, at wavelengths shorter than 12 μm, we use tabulated values[108]. At wavelengths longer than 12 μm, the intrinsic optical response is due to phonons. We model $\epsilon_{InGaAs}(\omega)$ at these long wavelengths by interpolating between the permittivity of InAs[79] and the permittivity of GaAs[79] using the composition ($In_{0.53}Ga_{0.47}As$):

$$\epsilon_{InGaAs} = 0.53 \times \epsilon_{InAs} + 0.47 \times \epsilon_{GaAs}, \text{ when } \lambda > 12\ \mu m. \tag{3-7}$$

We use the following Drude term to account for the free-carrier absorption in the n-doped material:

$$\epsilon_{Drude} = -\frac{N_e e^2}{\epsilon_0 m_e^*} \frac{1}{\omega^2 - i\omega\Gamma_e}\ , \tag{3-8}$$

where the electron concentration is given by $N_e = \frac{1}{2}\left(N_D + \sqrt{N_D^2 + 4n_i^2 e^{qV_J/k_B T_C}}\right)$, $N_D$ is the donor concentration, and $n_i = 6.3 \times 10^{11}\ cm^{-3}$ is the intrinsic carrier concentration for InGaAs at room temperature[109]. Here, $V_J$ is the voltage bias on the photovoltaic cell junction, and $T_C$ is the temperature of the photovoltaic cell. The electron effective mass, $m_e^*$, is determined by using the dependence of electron effective mass on electron concentration[110]. The electron scattering rate is $\Gamma_e = \frac{e}{m_e^* \mu_e}$, where the electron mobility $\mu_e$ is obtained from ref.[111]. For a n-doping level $N_D = 1 \times 10^{17}\ cm^{-3}$, the effective mass is $m_e^* = 0.041\ m_e$, where $m_e$ is the mass of electron, and the electron mobility is $\mu_e = 8727\ \frac{cm^2}{V \cdot s}$; At an n-doping of $1 \times 10^{18}\ cm^{-3}$, the effective mass $m_e^* = 0.0483\ m_e$, and electron mobility is $\mu_e = 5639\ \frac{cm^2}{V \cdot s}$.

To model the permittivity of doped InP, we use a similar approach by accounting for both the intrinsic optical response and free carrier effects. The permittivity of doped InP is:

$$\epsilon_{doped\ InP}(\omega) = \epsilon_{InP}(\omega), \text{ when } \omega \geq \omega_g$$

$$\epsilon_{doped\ InP}(\omega) = \epsilon_{InP}(\omega) + \epsilon_{Drude}(\omega), \text{ when } \omega < \omega_g \ ,$$

where $\omega_g$ is the angular frequency corresponding to the bandgap of InP. The permittivity for intrinsic InP is taken from ref.[79]. We use a Drude term to account for the free carrier optical response in doped InP:

$$\epsilon_{Drude} = -\frac{N_e e^2}{\epsilon_0 m_e^*}\frac{1}{\omega^2 - i\omega\Gamma_e} - \frac{N_h e^2}{\epsilon_0 m_h^*}\frac{1}{\omega^2 - i\omega\Gamma_h}. \tag{3-9}$$

Here, the electron and hole concentrations are given by

$$N_e = \frac{1}{2}\left(N_D - N_A + \sqrt{(N_D - N_A)^2 + 4n_i^2}\right) \text{ and}$$

$$N_h = \frac{1}{2}\left(N_A - N_D + \sqrt{(N_A - N_D)^2 + 4n_i^2}\right), \tag{3-10}$$

where $N_D$ and $N_A$ are donor and acceptor concentrations, respectively, and the intrinsic carrier concentration for InP[109] at room temperature is $n_i = 1.3 \times 10^7\ cm^{-3}$. The electron effective mass $m_e^*$ is determined by using the dependence of electron effective mass on electron concentration[112]. The electron scattering rate is $\Gamma_e = \frac{e}{m_e^* \mu_e}$, where the electron mobility $\mu_e$ is obtained from ref.[113]. For the hole effective mass we use $m_h^* = 0.6\, m_e$. The hole scattering rate is $\Gamma_h = \frac{e}{m_h^* \mu_h}$, where the hole mobility $\mu_h = 150\frac{cm^2}{V \cdot s} \times \frac{1}{1+\left(\frac{N_A}{2\times 10^{17} cm^{-3}}\right)^{1/2}}$ and was obtained from ref.[114].

Based on the above parameters, we adopt the following values for our model: For the n-doped InP layer, with $N_D = 1 \times 10^{18}\ cm^{-3}$ and $N_A = 0$, the effective electron mass is $m_e^* =$

$0.0831\ m_e$, the electron mobility is $\mu_e = 2096\,\frac{cm^2}{V\cdot s}$, the effective hole mass is $m_h^* = 0.6\,m_e$, and t-he effective hole mobility is $\mu_h = 150\,\frac{cm^2}{V\cdot s}$. For the p-doped InP layer, with $N_A = 1\times 10^{18}\ cm^{-3}$ and $N_D = 0$, the effective electron mass is $m_e^* = 0.08\,m_e$, electron mobility is $\mu_e = 5400\,\frac{cm^2}{V\cdot s}$, the effective hole mass is $m_h^* = 0.6\,m_e$, and the effective hole mobility is $\mu_h = 46.4\,\frac{cm^2}{V\cdot s}$. Finally, the permittivity for gold is obtained from ref[79].

Next, we describe the modelling of the emitter, where the circular mesa consists of a 60 μm thick layer of p-doped Si (doping concentration $3\times10^{19}$ cm$^{-3}$), covered by 10 nm-thick layer of AlN on both sides. To account for the high-temperature operation of the emitter, a temperature-dependent permittivity is used to model the doped Si[80, 115]. The optical properties of the aluminum nitride layer are modelled using tabulated permittivity at room temperature[116].

Using a scattering matrix formalism based on fluctuational electrodynamics, we then calculate the radiative energy transfer between any two layers in the multi-layer structure. In specific, to estimate $P_{\mathrm{MPP}}$, we calculate the transmission probability from the mesa of the emitter to the active layer (junction) for both transverse-electric (TE) and transverse-magnetic (TM) modes, i.e., $\tau_{TE,mesa\to J}(\omega,k)$ and $\tau_{TM,mesa\to J}(\omega,k)$, where $k$ denotes the parallel wave-vector. For simplicity, we use the following dimensionless transfer function.

$$\phi_{mesa\to J} = \left(\frac{\lambda}{2\pi}\right)^2 \int_0^\infty kdk\left[\tau_{TE,mesa\to J}(\omega,k) + \tau_{TM,mesa\to J}(\omega,k)\right]. \qquad (3\text{-}11)$$

Similarly, we denote the transfer function from the active layer of the photovoltaic cell to all the other layers of the photovoltaic cell as $\phi_{J\to O}$.

Next, to estimate the total energy transfer, $Q_{\mathrm{RHT}}$, we calculate the transfer function from the emitter to the whole PV cell denoted as $\phi_{mesa\to C}$, where C denotes the whole PV cell. We

denote the area of mesa as $A_{mesa}$. This calculation is performed in wavelengths ranging from 100 $\mu m$ to 0.7 $\mu m$. Further, to calculate the contributions from the recessed 'rec' region of the emitter, we model it as multi-layer structure as shown in Fig. 3.17b, similar to that followed for the mesa region. The corresponding transfer functions between the rec and active layer, rec and the whole PV cell are denoted by $\phi_{rec \to J}$ and $\phi_{rec \to C}$, respectively.

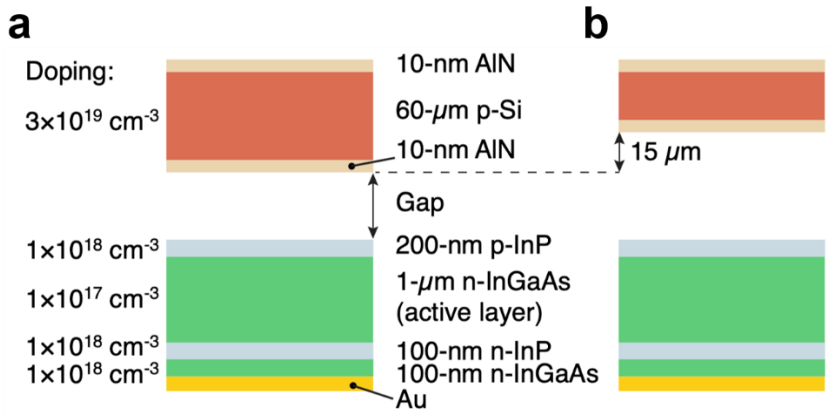


*Figure 3.17 Geometry for the PV cell and radiative energy transfer.*

*a, Schematic describing the geometry for the mesa of the emitter and the PV cell, including composition, doping concentration, and thickness of each layer. b, Schematic geometry for the recessed region of the emitter and PV cell.*

*PV cell I-V response modelling*

The *I-V* response of our PV cell is modelled using an equivalent circuit as shown in Fig. 3.18, where the polarity for the current is defined such that both *V* and *I* are positive when the cell generates electricity. We use an experimentally obtained dark *I-V* response, which is measured under no illumination in vacuum at room temperature, to estimate the parasitic series resistance as $R_{series} = 85\ \Omega$ based on the slope of *I-V* curve at large forward voltage and a parasitic shunt resistance as $R_{shunt} = 5 \times 10^6\ \Omega$.

To calculate the total current generated in our PV cell, we include the current contributions from both the radiative and non-radiative recombination processes. First, we describe the current generated by radiative processes ($I_{\text{rad}}$) as:

$$I_{rad}(V_d) = e\int_{\omega_g}^{\infty} d\omega \frac{1}{\lambda^2}\Bigg[\left(VF_{mesa,J}\, A_{mesa}\phi_{mesa\to J} + VF_{rec,J}\, A_{rec}\phi_{rec\to J}\right)\left(\frac{1}{e^{\frac{\hbar\omega}{k_B T_E}}-1} - e^{-\frac{\hbar\omega - qV_J}{k_B T_C}}\right) + \left(VF_{mesa,J}\, A_{mesa}\phi_{O\to J}^{mesa} + VF_{rec,J}\, A_{rec}\phi_{O\to J}^{rec}\right)\left(e^{-\frac{\hbar\omega}{k_B T_C}} - e^{-\frac{\hbar\omega - qV_J}{k_B T_C}}\right)\Bigg] \quad (3\text{-}12)$$

where $e$ is the elementary charge, $T_C$ is the temperature of the cell including the junction, $T_E$ is the temperature of the emitter, and subscript $O$ denotes all the layers in the PV cell other than the active layer. Here, $VF_{mesa,J}$ and $VF_{rec,J}$ are the view factors associated with both the surfaces, the details of which are discussed in the next section. We assume the internal quantum efficiency of the PV cell to be 100%, or every photon absorbed in the active layer generates an e-h pair. We note that we have used the reciprocal relation for transfer functions, i.e. $\phi_{1\to 2} = \phi_{2\to 1}$.

Next, to account for current from non-radiative processes, we consider Auger recombination and Shockley-Read-Hall (SRH) recombination. The net recombination current associated with Auger recombination ($I_{Auger}$) is given by:

$$I_{Auger}(V) = eA_J\left(C_n n + C_p p\right)(np - n_i^2)t_J, \quad (3\text{-}13)$$

where $C_n$and $C_p$ are the Auger recombination coefficients for electron and hole, respectively, $n_i$ is the intrinsic carrier concentration at zero bias, and $t_J$ and $A_J$ are the thickness and area of the active layer of the photovoltaic cell, respectively. The combined Auger recombination coefficient is $C_n + C_p = 7\times 10^{-29}\ cm^6/s$ as obtained from ref.[109]. We treat $C_n = C_p = 3.5\times 10^{-29}\ cm^6/s$. For the active layer with n-doping,

$$n(V_J) = \frac{1}{2}\left(N_D + \sqrt{N_D^2 + 4n_i^2 e^{\frac{qV_J}{k_B T_C}}}\right), \text{ and } p(V_J) = \frac{1}{2}\left(-N_D + \sqrt{N_D^2 + 4n_i^2 e^{\frac{qV_J}{k_B T_C}}}\right). \quad (3\text{-}14)$$

The net recombination current associated with SRH process ($I_{SRH}$) is given by:

$$I_{SRH}(V_C) = eA_J S\frac{2(np - n_i^2)}{n + p + 2n_i},$$

where $S$ is the effective surface recombination velocity. The total current ($I_J$) through the PV cell junction is then given by the sum of all the currents as:

$$I_J(V_J) = I_{rad}(V_J) - I_{Auger}(V_J) - I_{SRH}(V_J). \quad (3\text{-}15)$$

Further, by accounting for the series resistance and shunt resistance, the total current through the device and the total voltage across the device are:

$$I(V_J) = I_{rad}(V_J) - I_{Auger}(V_J) - I_{SRH}(V_J) - \frac{V_J}{R_{shunt}} \quad \text{and}$$

$$V = V_J - I(V_J) \cdot R_{series}. \quad (3\text{-}16)$$

The above two characteristic equations are used to obtain the *I-V* response of the PV cell. The surface recombination velocity $S \approx 3.5 \times 10^5 \frac{cm}{s}$ is a fitting parameter adjusted to best match the *I-V* curve obtained from our model with that of the experimentally measured dark *I-V* curve.

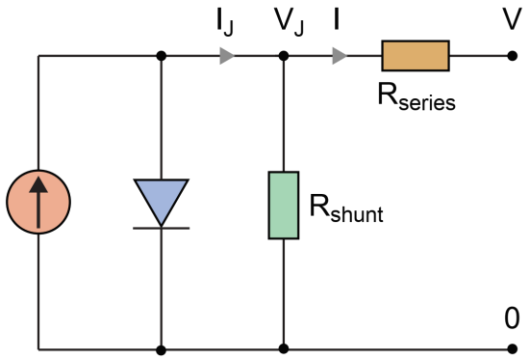


*Figure 3.18 Equivalent circuit of the photovoltaic (PV) cell.*

*Schematic illustration of the equivalent circuit used to model the photovoltaic response of our cells.*

**Effect of view factor in the near-field enhancement**

In our theoretical model described in the previous section, we incorporate the effect of view factors between the surfaces on the emitter ('mesa' and the recessed region 'rec') and the surface of the PV cell (labeled 'J'). Specifically, we compute the view factors $VF_{mesa,J}$ and $VF_{rec,J}$, as a function of gap size. $VF_{mesa,J}$ is calculated by treating the geometry as two coaxial parallel discs[1] (mesa = 150 μm diameter and J = 190 μm diameter) as shown in the top inset of Fig. 3.19a. Further,

$VF_{rec,J}$ is calculated by approximating the geometry of recessed region and PV cell as two coaxial circular rings with inner diameter 150 μm and outer diameter 190 μm (bottom inset of Fig. 3.19a). An analytical expression for the view factor between circular rings is used as described in ref.[117]. The variation of these two factors with gap size is plotted in Fig. 3.19a. Since our calculation of radiative energy transfer between multilayer structures assumes the structures to be infinitely long in lateral directions, it is important to delineate the effect of view factors in the enhancement of power generation in the near-field. To this end, we plot the variation of theoretically computed $P_{MPP}$ with the gap size. The data presented in Fig. 3.19b (computed for $T_{emitter}$ = 1270 K) illustrates that inclusion of the corrected view factor results in values of $P_{MPP}$ that are somewhat different from those calculated with a view factor of 1 (infinite plates). In the far-field at 10 μm gap, ~10% variation in the power output could be seen, while the variation is less than 1% at smaller gaps. This is because the energy transfer in near-field is dominated by mesa whose view factor is close to 1 at these gaps as seen in Fig. 3.19a. Thus, the effect of view factor on power enhancement at smaller gaps is negligible.

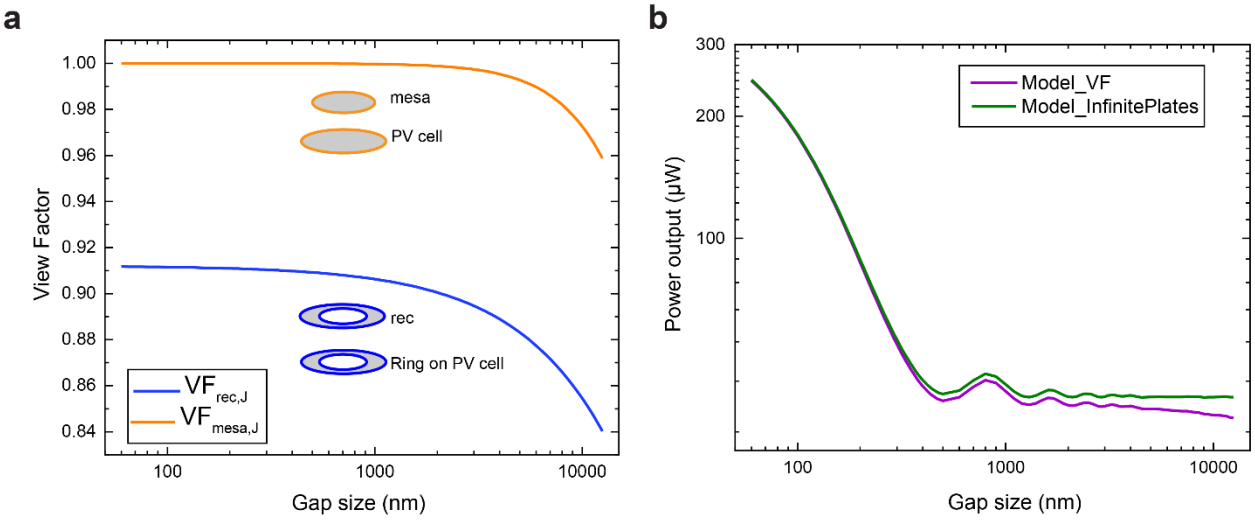


*Figure 3.19 Effect of view factor on power enhancement.*

*a, View factors $VF_{mesa,J}$ and $VF_{rec,J}$ as a function of gap size between the emitter and PV cell. The orange curve corresponds to the view factor change as the gap between mesa and PV cell is reduced from above 10 μm to 60 nm,*

*while the blue curve corresponds to the view factor change between the recessed region 'rec' (recessed by 15 μm) and a circular ring on PV cell with OD/ID of 190/150 μm. b, $P_{MPP,M}$ as a function of gap size for two cases. Violet solid line corresponds to the incorporation of view factors calculated in Supplementary Fig. 9a, while the green curve corresponds to the assumption of view factor of 1 (infinite plates).*

## Characteristics of the PV cell

The current-voltage response of the PV cell under dark conditions (referred to as Dark *I-V*) is shown in Fig. 3.20a. For this measurement the PV cell was maintained at room temperature in a high vacuum of 1 μTorr. The voltage across the PV cell was varied from -0.5 V to 0.5 V in steps of 10 mV, while the current through the circuit was measured. The variation of fill-factor (*FF*, Fig. 3.20b) with temperature is plotted along with the theoretical calculations. The small disagreement between measured and calculated *FF* may likely be due to the uncertainties in our modeling parameters such as the series and shunt resistances.

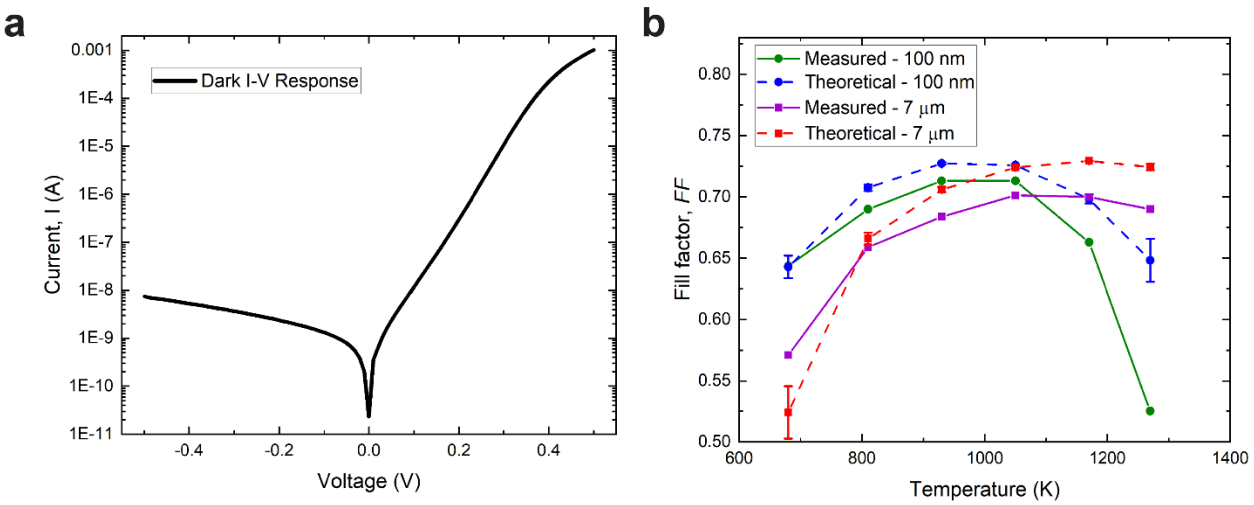


*Figure 3.20 Characteristics of the photovoltaic cell.*

*a, Dark I-V response of the PV cell. b, Measured and calculated fill factor (FF) as a function of temperature. Green circles and violet squares represent the experimental data points, while blue circles and red squares represent the calculated data points with the corresponding uncertainties, at gap sizes of 100 nm and 7 μm respectively. Solid and dashed lines added as a guide to the eye.*

## Sub-band gap reflection from thin-film PV cell

The improvement in the efficiency of our NFTPV system was achieved by employing a thin-film PV cell as shown in Fig. 3.21a. Typical bulk PV cells suffer from significant sub-band

gap (SBG) absorption as a result of free-carrier absorption in heavily doped layers. The SBG suppression in the thin-film PV cell can be understood by comparing two structures: The current NFTPV system with $T_{emitter}$ = 1270 K at a gap size of 100 nm (Fig. 3.21a) and a thick NFTPV structure, where the n-InP layer was assumed to have a thickness of 200 µm with $T_{emitter}$ = 1270 K at a gap size of 100 nm (Fig. 3.21b). Using our theoretical model, we then calculate the spectral energy transfers for both cases as shown in Fig. 3.21c as a function of photon energy. The above-band gap flux is similar in both structures because the active layers are of identical thickness. A significant suppression of SBG is seen in a thin-film PV cell as compared to a bulk PV cell, because lower energy photons get absorbed in the 200 µm-thick n-InP layer before getting reflected by the gold layer. Thus, for the thin-film case, low energy photons get reflected back to the emitter improving the overall efficiency. The residual SBG absorption in the thin-film case is due to absorption in the gold layer (imperfect reflector).

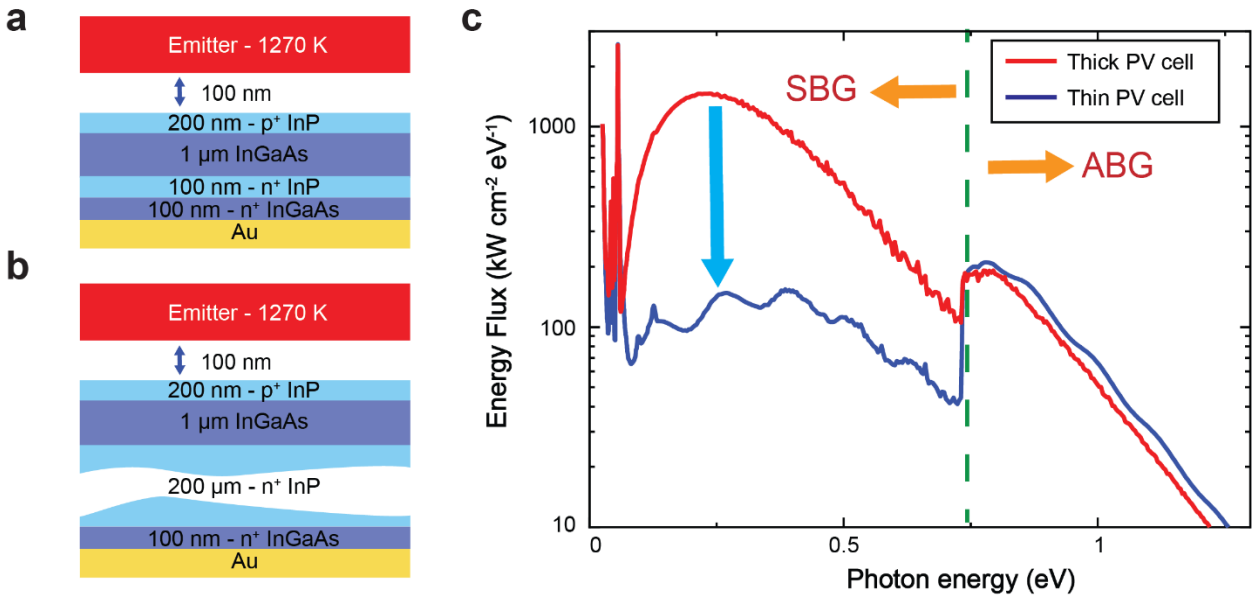


*Figure 3.21 Thin-film sub-band gap reflection*

*a, Schematic of the thin-film TPV system employed in this study showing the thicknesses of all the layers. b, Schematic of a hypothetical thick TPV structure, where the n-InP layer thickness is increased from 100 nm to 200 µm. c, Spectral energy transfer as a function of photon energy for a thin-film PV cell (solid blue line) and a bulk PV cell (solid red line).*

## 3.7 Conclusion

We demonstrated efficient (~6.8%, excluding the heat losses through conduction and radiation from surfaces not facing the photovoltaic cell) thermophotovoltaic power generation in the NF (<100 nm gaps) at an unprecedented power density of ~5 $kW/m^2$ when the emitter is heated to 1270 K and the PV cell is at room temperature. This power density is more than an order of magnitude higher than for the best-reported TPV systems in the NF, while also operating at 6-times higher efficiency[66]. By employing a heavily-doped silicon, we could successfully operate the emitter in the temperature range of 300 – 1270 K by Joule heating. Further, the emitters presented here, capable of operation at high temperatures (up to 1270 K), present a platform for future work aiming to experimentally explore novel strategies to improve NFTPV performance by engineering thermal emitters[118-122] or PV cells[53, 123]. These advances are expected to help establish the principles necessary for the exploitation of a range of NF based TPV nanotechnologies. Future studies on the long-term stability of the emitters at high temperatures with various protective coatings, under a range of pressures could enable realization of practical devices**.**

# Chapter 4 Sub-nanowatt Resolution Direct Calorimetry for Probing Real-time Metabolic Activity of *C. elegans* Worms

Reproduced with permission from reference[124]:

S. Hur*, R. Mittapally*, S. Yadlapalli, P. Reddy, E. Meyhofer, *Nature Communications*, 11, 2983 (2020).

## 4.1 Abstract

Calorimetry has been widely used in metabolic studies, but direct measurements from individual small biological model organisms such as *C. elegans* or isolated single cells have been limited by poor sensitivity of existing techniques and difficulties in resolving very small heat outputs. Here, by careful thermal engineering, we developed a robust, highly sensitive and bio-compatible calorimetric platform that features a resolution of ~270 pW—more than a 500-fold improvement over the most sensitive calorimeter previously used for measuring the metabolic heat output of *C. elegans*. Using this calorimeter, we demonstrate time-resolved metabolic measurements of single *C. elegans* worms from larval to adult stages. Further, we show that the metabolic output is significantly lower in long-lived *C. elegans daf-2* mutants. These demonstrations clearly highlight the broad potential of this tool for studying the role of metabolism in disease, development and ageing of small model organisms and single cells.

## 4.2 Introduction

Calorimetry, a technique that can be utilized to quantify the amount of heat released or absorbed during chemical or physical processes, has been instrumental in analyzing the thermodynamics of reaction mechanisms[125, 126]. Importantly, calorimeters are also critical for analyzing the metabolism of living cells and organisms, which is defined as the sum total of all the heat output associated with the bio-chemical processes in cells[127]. Because of the central role that energy and metabolism play in the normal function of cells[128], it is not surprising that metabolic changes are implicated in aging[129, 130] and human diseases, including cancers[131]. Calorimetric measurements, which directly record the heat generated by a (biological) system, represent a non-invasive approach for accurate quantification of metabolic activity, as the metabolic heat output is an integrated signal of both aerobic and anaerobic processes[132-134]. However, such calorimetric measurements have not been able to resolve the heat output from small individual organisms, such as the nematode worm *Caenorhabditis elegans* (*C. elegans*), or isolated cells, due to poor sensitivity, insufficient long-term stability and challenges in physiological compatibility.

In this work, we describe a tool capable of systematically studying the metabolism of individual *C. elegans,* which is a widely used model organism because of its ease of maintenance and short generation times[135, 136]. We note that this tool is expected to be broadly useful, as *C. elegans* metabolism is being actively investigated due to its promise for providing insights into human disease and ageing[129, 130, 134, 137-140]. For example, it is well known that genetic mutations, such as *age-1* and *daf-2* mutants, increase the lifespan of the worms mediated via various transcription factors with roles in insulin signaling, autophagy, and cellular energy metabolism[140-142]. Thus, metabolic heat output measurements on single worms through direct

calorimetry can provide fundamental insights into metabolic pathway regulation in the context of the biological mechanisms mentioned above. We note that so far *C. elegans* metabolic heat output studies have been limited to large populations of worms as existing calorimeters lack the desired sensitivity (sub-nW resolution) to resolve signals from a single worm[132-134, 143]. In fact, the highest resolution claimed for biological calorimetry is at the few nanowatt level (1.9 nW)[144] and was achieved by miniaturizing calorimetric platforms[144, 145] to such small sizes that they are unsuitable for studying relatively larger biological samples such as *C. elegans*. As a result, the most sensitive calorimeter used for measuring *C. elegans* was limited to a resolution of 170 nW[143] making it impossible to study metabolism from individual worms. Finally, we note that none of the available tools have been able to monitor real time metabolic heat changes with respect to worm size, their activity levels and individual physiological or genetic differences, posing significant barriers to progress.

### 4.3 Devices and experimentation

#### Design of the calorimeter

Our calorimeter provides a heat resolution of ~270 pW—a 500-fold[143] improvement over calorimeters employed for past *C. elegans* studies and a 10-fold[144, 145] improvement compared to the state-of-the-art bio-calorimeters. Further, our approach also incorporates a fluidic environment and optical imaging capabilities. Our instrument is made possible by integrating three sub-systems (see Fig. 4.1a): First, a thermal system composed of three nested shields (Fig. 4.1a, b) made from copper (whose temperature is feedback controlled) that house two capillary tubes—a sensing capillary tube containing the sample of interest and a matching capillary tube which acts as a reference (explained in more detail below)—ensures that ambient temperature fluctuations have a minimal effect on the temperature of the capillary tubes. Second, a fluidic system enables

transfer of individual worms into the sensing capillary tube and maintaining them under physiological conditions (Fig. 4.1a). Third, an inverted microscope-based imaging system facilitates tracking of the activity of the biological specimen (Fig. 4.1a).

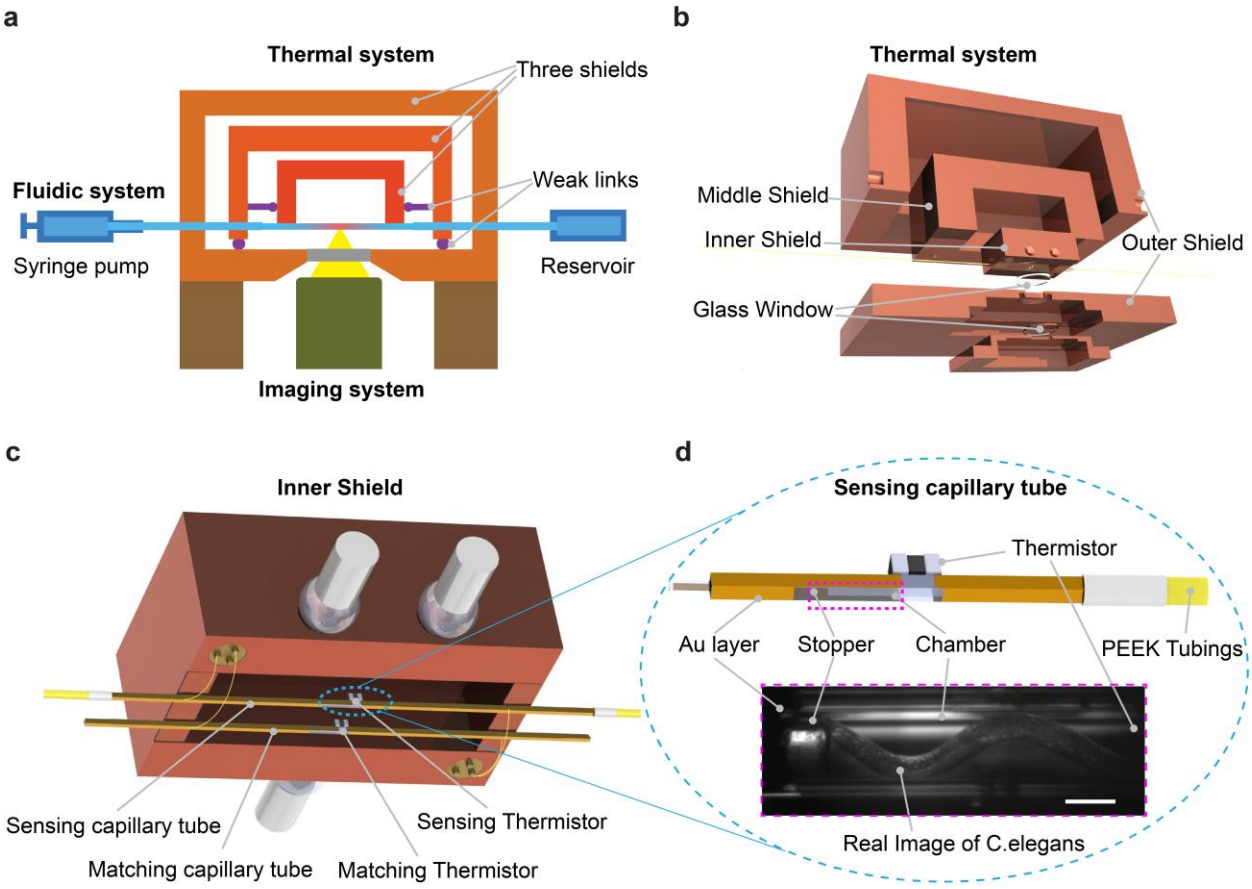


*Figure 4.1 Experimental setup.*

*(a) Schematic depicting the three subsystems in our calorimeter: the fluidic system (shaded in blue) with the syringe pump and reservoir for sample handling, the optical imaging system (green) focused to the center of the capillary tube and the thermal system involving the three shields with weak thermal links (between OS and MS, MS and IS shown in purple) mounted on the microscope stage. (b) Detailed isometric expanded view of the thermal system showing the assembly of all components. (c) Illustration of IS assembly (not to scale) showing two capillary tubes, the sensing capillary with a PEEK tubing assembly and the matching capillary, with respective thermistors connected in a Wheatstone bridge configuration to extract differential thermal signal. (d) Magnified view of the ringed area in (c), depicting the capillary tube coated with gold on all four sides, except for the central region, where the C. elegans is localized, and instrumented with a thermistor to record the temperature. A borosilicate stopper traps the C. elegans in the center of the sensing capillary tube. A CCD image (marked in magenta dashed line) of a trapped C. elegans during a reference measurement shows the corresponding stopper and Au layer. Images were reproducibly taken every second during the measurement. Scale bar: 100 μm.*

To elaborate, the shields are comprised of an outer shield (OS), a middle shield (MS) and an inner shield (IS) (Fig. 4.1b), which are nested into each other and are mechanically held together by thermally poorly conducting mechanical contacts, which we refer to as weak thermal links, to provide excellent thermal isolation from the ambient. The OS also serves as a vacuum chamber such that all the components included in it (including the capillary tubes) are maintained at a vacuum level below 10 μTorr. Further, the OS features custom-made instrumentation, fluidic and optical feedthroughs, and is actively controlled to a temperature stability of ±1 mK (all temperature signals are measured in a bandwidth of 0.1 Hz, unless mentioned). The MS and IS provide temperature stabilities down to ±15 μK through active proportional-integral-derivative (PID) feedback control (see Methods). We note that this temperature stability (with direct optical access) is comparable to the best stabilities achieved previously in similar approaches, but without optical access[146, 147]. The sensing and matching capillary tube systems are suspended on the IS (Fig. 4.1c). Both tubes are instrumented with thermistors at the center of the tubes (Fig. 4.1c). The two capillary tubes have nominally identical dimensions and are 20 mm-long borosilicate tubes with a square cross-section, (250 μm × 250 μm outer dimensions and 50 μm wall thickness). Further, the tubes are coated with a 100 nm-thick layer of gold on all sides except a small portion in the center that provides optical access for imaging (Fig. 4.1d). A 125 μm-diameter borosilicate rod is inserted from one end into the sensing capillary tube until it reaches the center and serves to localize the worm in the center of the capillary tube where the thermistor is mounted (Fig. 4.1d). The entire system is mounted on an inverted microscope and the sensing capillary is imaged through a 10x objective to monitor the specimen's activity. Finally, the fluidic system consists of a syringe pump at one end, for manipulating the specimen and flow rate, and a reservoir (petri dish) at the other end, for loading or unloading specimens (Fig. 4.1a).

**Characterization of thermal resolution**

The principle of operation of our calorimeter can be understood by noting that when heat is generated inside the sensing capillary tube (e.g. due to the metabolic output of a sample) its temperature rise, ($\Delta T_{th,}$), is detected by the thermistor and can be directly related to the metabolic heat output ($\dot{Q}_{metabolic}$) via $\dot{Q}_{metabolic} = G_{th} \times \Delta T_{th}$, where $G_{th}$ is the thermal conductance of the sensing capillary tube and can be directly measured (see Methods). Thus, the heat output resolution is determined by the thermal conductance of the capillary tube (low values of $G_{th}$ are desirable for increased resolution of $\dot{Q}_{metabolic}$) and the temperature resolution of the thermistor[77, 148]. In our system, we achieve a small $G_{th}$ by carefully engineering the capillary tube to minimize the contribution of the various heat pathways (conduction, convention and radiation). Specifically, the conductive contribution to $G_{th}$ is minimized by choosing a sufficiently small cross-section ($G_{capillary}$ = 9.6 μW $K^{-1}$, $G_{buffer}$ = 6 μW $K^{-1}$), while the thin gold coating ($G_{Au}$ = 2.7 μW $K^{-1}$) on the capillary reduces the radiative contribution to $G_{th}$. Nevertheless, providing optical access to the calorimeter results in some unavoidable radiative coupling ($G_{rad}$ ~ 6 μW $K^{-1}$) to the outer shield. Since the capillary is operated in a vacuum system, the convective contribution is reduced to negligible levels ($G_{th,air}$ ~ 250 μW $K^{-1}$). In total, the $G_{th}$ under operating conditions (flow rate of 100 nl $min^{-1}$) is 27 μW $K^{-1}$ (see Figs. 4.2a, 4.6), and the noise floor of the temperature measurement is 10 μK (see Fig. 4.2a and inset). As a result, our calorimetry successfully detects 270 pW of heat output ($\dot{Q}_{metabolic} = G_{th} \times \Delta T_{th}$ = 27 μW $K^{-1}$ × 10 μK).

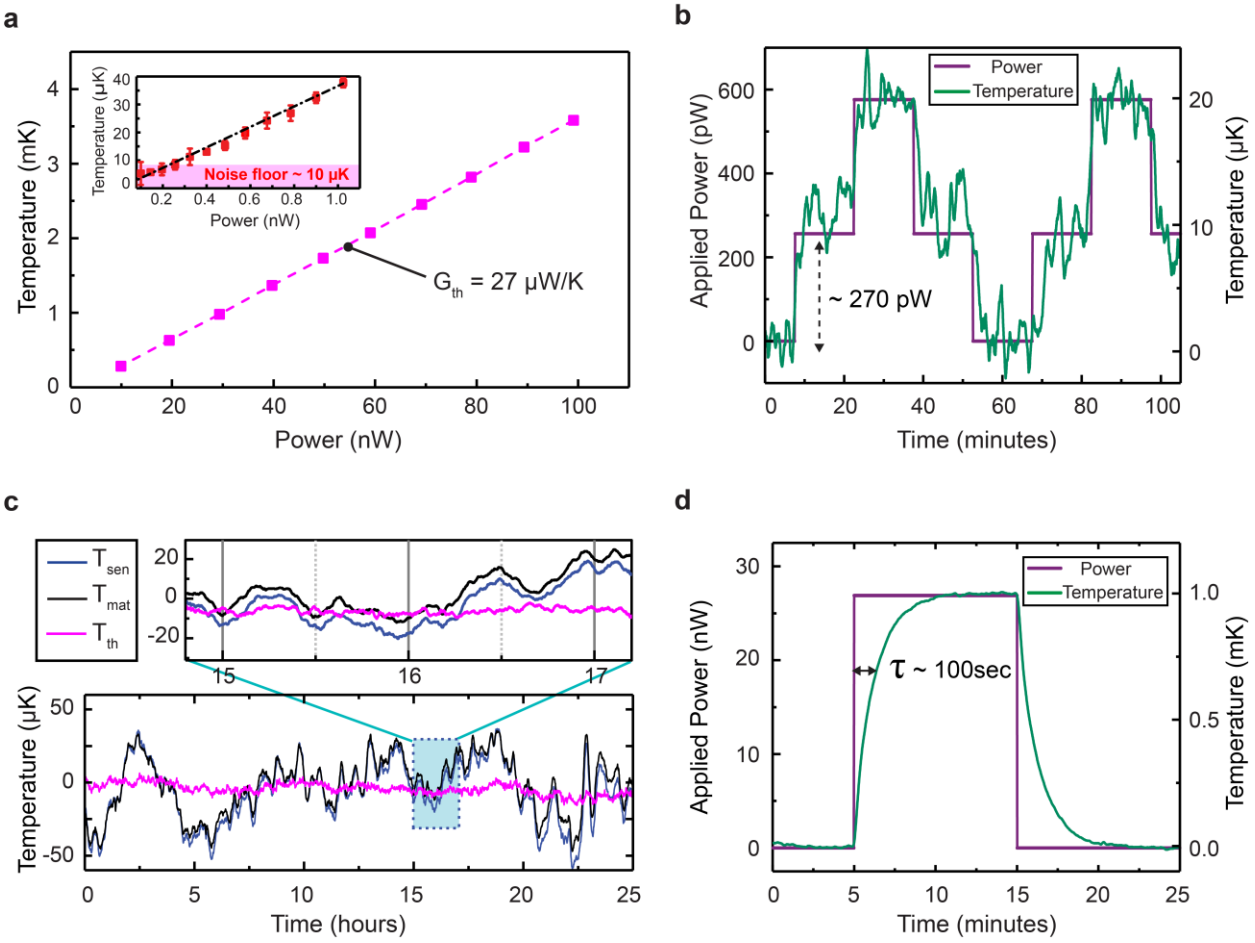


*Figure 4.2 Thermal characterization of the calorimeter.*

*(a) Thermal conductance characterization ($G_{th}$) performed at a flow rate of 100 nl $min^{-1}$: Temperature rise ($\Delta T_{th}$) of the center of the sensing capillary tube as a function of the DC power input is plotted, resulting in $G_{th}$ of ~27 μW $K^{-1}$ (magenta squares). The inset shows the temperature rise for sub-nW level inputs that result in a smaller temperature rise (0-40 μK). The data represents the mean value of four different measurements and the error bars represent the standard deviation (±SD). From the observed standard deviation of (±5 μK) we estimate a noise floor of ~10 μK. (b) Validation of thermal resolution. A thermal pulse (purple solid line) with steps of 270 pW applied on the capillary (see Methods) resulted in a corresponding 10 μK rise on the temperature signal (green solid line), validating our calorimeter's capability to resolve at least 270 pW (heat resolution). (c) Temperatures of both the capillaries ($T_{mat}$ in solid black, $T_{sen}$ in solid blue) without any sample in the sensing capillary tube are plotted for a 30-hour timespan, indicating fluctuations of ±5 μK in the differential signal ($T_{th}$ in solid magenta). A 2-hour window (blue box) clearly shows that $T_{mat}$ follows $T_{sen}$ indicating a common mode radiative coupling to the outer shield. (d) Time constant of the sensing capillary tube. A square thermal pulse (purple solid line) in steps of ~ 27 nW results in a first order temperature response with a time constant of ~1.5 minutes.*

We achieved excellent temperature resolution ($\Delta T_{th}$ = 10 μK), as reflected in the precision of the temperature measurements shown in Fig. 2a and its inset (see Methods section titled Thermal conductance measurement and power resolution for more details). We accomplished this high temperature resolution by employing an AC-excited Wheatstone bridge (see Methods) in an

environment where thermal fluctuations of the capillary tube were attenuated via feedback-controlled shields (described above). Further, we took advantage of a thermistor embedded into the matching capillary tube (see Fig. 4.1C) to attenuate common mode temperature drifts. As shown in Fig. 4.2c and its inset, the temperature of the sensing capillary ($T_{sen}$) follows that of the matching capillary ($T_{mat}$), indicating a common mode radiative coupling to the environment, while the differential signal ($T_{th}$) can be observed to be stable to within ±5 μK. Taken together, this approach enables us to accomplish a noise equivalent temperature (NET) resolution of ±5 μK in 2 hours and ~10 μK drift (bandwidth of 5 mHz) in 24 hrs (Fig. 4.2c). This implies that, in addition to being able to resolve transient heat output changes (occurring in mins) of 270 pW (Fig. 4.2b), our system can track heat output changes over a day with same accuracy. Thus, our instrument is well-suited for real-time metabolic measurements on several small biological specimens like *C. elegans*. The temporal resolution of our calorimeter is set by the thermal time constant of the device which is ~100 sec (Fig. 4.2d).

## 4.4 Results

### Heat output measurement protocol and analysis

To establish the applicability of our system to biological measurements, we performed metabolic measurements on individual *C. elegans* at 25 °C. A typical measurement in our calorimeter involves five phases (Fig. 4.3a): first, establishing a baseline $T_{th}$ (shown in gray) without a worm in the sensing capillary and a flow rate of 100 nl $min^{-1}$ (all measurements reported here were performed at this flow rate). The worm is then loaded from an external reservoir under visual inspection at a larger flow rate of ~2-10 μl $min^{-1}$ (shown in violet). Once the worm is loaded and properly localized in the sensing capillary tube, the flow rate is reduced to 100 nl $min^{-1}$, for continuously recording its heat output and for monitoring its activity (see Methods) via video

microscopy (indicated by orange region in Fig. 4.3a) for a desired time (~1-2 hrs). This optimal flow rate was chosen so as to both replenish the oxygen content in the fluidic medium (typical oxygen concentration < 8 mg.$O_2$ $l^{-1}$ at atmospheric pressure), thus avoiding oxygen deprivation of the worm (maximum reported[132] oxygen consumption of 16 ng.$O_2$ $h^{-1}$ worm), and holding the worm in the desired location, which is facilitated by both the flow and the borosilicate fiber stopper (see Fig. 4.1d). This approach solves the difficult task of constraining the worm[149] to the center of the sensing capillary while not inhibiting its natural swimming behavior. After monitoring the worm for the desired time interval, it is unloaded by reversing the flow at rates of 2-10 µl $min^{-1}$ (shown in blue in Fig. 4.3a). Once the worm is unloaded from the sensing capillary, the temperature (shown in grey) of the capillary is again recorded to confirm stability of the reference temperature ($T_{th}$). The worm is then transferred to a Nematode Growth Medium (NGM) Agar plate, to feed and grow (room temperature 22 °C), and the measurement cycle is repeated the following day, thus monitoring the metabolic heat changes of the same individual worm through its life-cycle. Maintaining such a small heat resolution while continuously replenishing nutrients and oxygen has not been possible in the most sensitive calorimeter[144], where the cells die within 20 minutes of their measurement due to lack of oxygen.

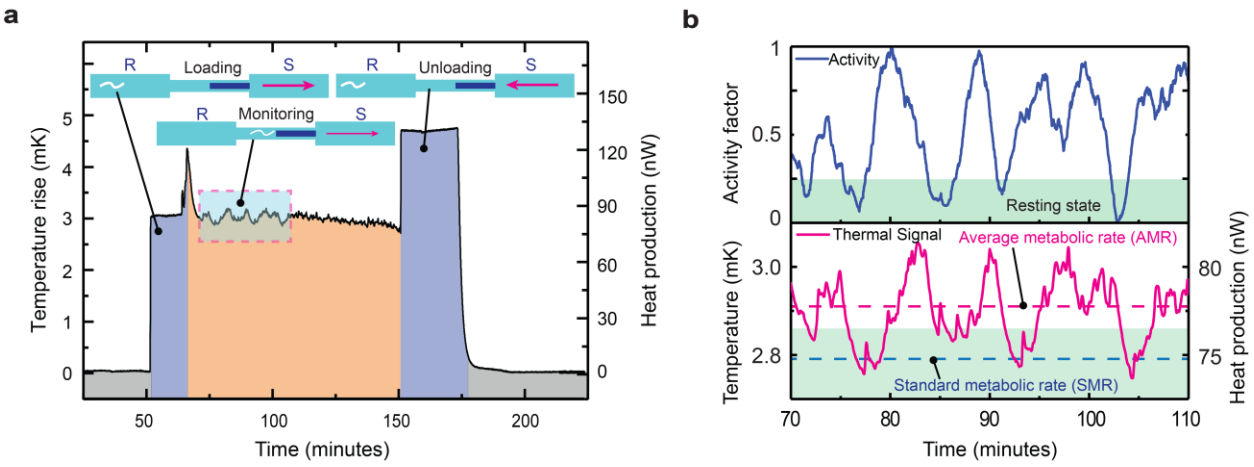


*Figure 4.3 C. elegans metabolic heat output measurement and analysis.*

*(a) A typical procedure to measure heat output from a single C. elegans involves establishing an initial reference (gray region), followed by loading the worm (violet region) from the reservoir side (R) with a syringe pump (S) at withdraw flow rates (R→S) of ~2-10 µl min-1. The orange region indicates the monitoring phase (1-2 hrs), followed by unloading (R←S, violet region) at flow rates of ~2-10 µl min-1. (b) Temperature rise (magenta plot in bottom panel) and activity factor (blue plot in top panel) of a reference measurement (marked blue region in fig. 3a). In the panel showing the activity factor, the worm's resting activity level is highlighted in green. From the corresponding metabolic signal, SMR (blue dashed line, bottom panel) is derived. AMR (magenta dashed line, bottom panel) is determined by averaging the thermal signal in a 30-minute time interval.*

In all our measurements, we observe that the worm's activity included prolonged periods of rapid swimming and resting periods, which are reflected, as expected, in distinct thermal signals. A normalized activity factor (see Methods) that quantifies worm activity shows that the metabolic heat output is strongly correlated with activity (correlation coefficient ~0.82, see Fig. 4.3b). Note that the blue line in Figure 4.3b shows a representative activity trace from a single *C. elegans*, while the magenta line presents simultaneously obtained metabolic heat output. From the measured thermal signal we extract two metabolic heat output readings, which we call the Average Metabolic Rate (AMR) and the Standard Metabolic Rate (SMR) (magenta and blue dashed lines respectively in Fig. 4.3b) at 25 °C. AMR is the average of the thermal signal in a 30-minute window (after an initial thermal equilibration time of 15 minutes) and SMR is the average of the metabolic heat output in the worm's resting state. We define the worm to be in resting state when activity factor is below 0.25 (green shaded region in Fig. 4.3b). These measurements clearly demonstrate our system's unique capability to monitor activity-related metabolic changes in single nematode worms.

**Metabolic measurements on N2 wild-type at different stages**

To investigate the metabolic changes during their life-cycle, we monitored the AMR of N2 wild-type strain from L1 larval stage to the adult stage (day 4). Since the size of *C. elegans* increases by more than an order of magnitude over the course of their lifetime, it is expected that early stage *C. elegans* metabolic heat output is smaller. As plotted in Figure 4.4a, our measurements reveal the metabolic heat output to vary from ~4 nW for the L1 stage to ~100 nW for the adult stage, more than a 20-fold change. The metabolic heat output increased as the worm progresses from L1 larval stage to the adult stage (day 4), and is consistent with the previously

observed oxygen consumption rates and heat output measurement performed on large number of worms[134, 138, 150]. Furthermore, we report metabolic heat output measurements from 61 N2 wild-type specimens (Fig. 4.4b, red triangles for AMR and blue triangles for SMR) as a function of weight. The weight (volume times density) of each worm was estimated by analyzing the 2D images captured from the imaging system (see Methods). These measurements indicate that the average mass-specific AMR and SMR (inset of Fig. 4.4b) are 55.8 ± 14.45 $\mu W\ mg^{-1}$ and 52.17 ± 12.65 $\mu W\ mg^{-1}$, respectively, demonstrating our calorimeter's ability to delineate small changes in activity-related metabolic heat output from that of the resting state (~ 7% increase above SMR). In these measurements the metabolic heat output of individual *C. elegans* worms increased with activity from 5-25% relative to the observed SMR. We note that a previous study[151] reported a 50% difference in AMR and SMR as opposed to the 7% observed in our study, but a direct comparison of our results with them is challenging due to important differences in the experimental conditions. In specific, we acquired SMR without restraining worm's activity to monitor metabolic rate whereas the earlier report[151] immobilized *C. elegans* either by levamisole-induced paralysis or by genetic paralysis. It is known that the relationship between any organism's metabolic rate and size is expected to follow a simple exponential scaling law[152], described as $Q = aM^b$, where $Q$, $M$, $a$ and $b$ are standard-metabolic heat output, body size, scalar constant and exponential constant, respectively. Most studies focused on this exponential constant $b$ across species (inter-specific) of animals ranging from unicellular microbes to elephants[153], including in *C. elegans*[154]. Here, we deduce an exponential constant of 0.76 ± 0.06 (Fig. 4.4c) from the metabolic rate measurements (SMR) of wild-type worms (intra-specific) at different stages (L3 – Day 3), which concurs with the reported inter-specific value of 0.72 ± 0.09[154]. Thus, our work

shows that the above scaling law is applicable to adult *C. elegans* intra-specifically and predicts the mass-specific metabolic rate across different stages.

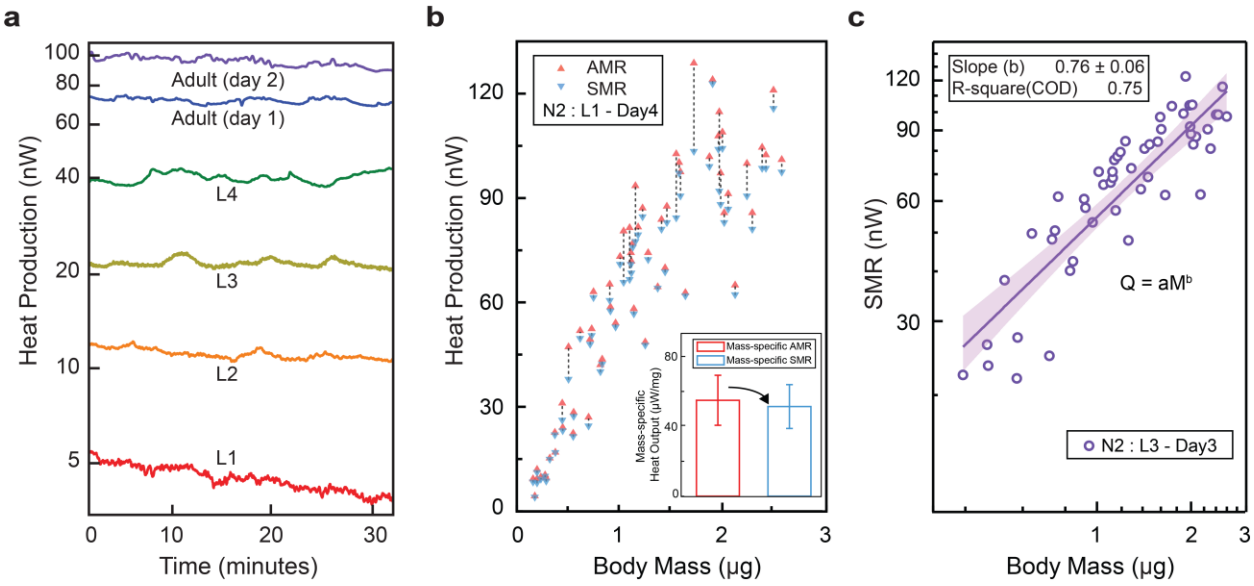


*Figure 4.4 Size-dependent metabolic heat output measurements on N2 wild-type.*

*(a) Real-time metabolic heat output profiles of referential C. elegans from L1 stage to Adult (Day 2) stage. (b) Metabolic heat output measurements of N2 wild-type worms (n = 61 independent trials) at different stages from L1 to Adult (Day 4). The red and blue triangles represent the AMR and SMR of individual worms, respectively, and are connected by a black dashed line to identify measurements from individual worms. The inset shows the mass-specific AMR (red) and SMR (blue) averaged over 61 N2 wild-type worms while the error bars represent the standard deviation (±SD) about the mean. (c) AMR vs. body size on a log-log plot to extract an allotropic scaling constant of 0.76 from (n = 52 independent trials) wild-type N2 samples from L3 to Adult (Day3). The purple solid line represents the best-fit with R-squared error of 0.75. The purple shaded region indicates the 95% confidence interval.*

### A long-lived mutant, daf-2, has lower metabolic heat output

To further demonstrate our system's ability to detect differences in metabolic activities, we have performed age-dependent metabolic heat measurements on a long-lived mutant, *daf-2(e1370)*. It is well established that the mutations that reduce the activity of a gene called *daf-2* (insulin/insulin-like growth factor-1 receptor) double the worm's lifespan[140]. This gene, which controls the expression of multiple longevity genes, is known to affect several biological processes including development, metabolism and resistance to stress. Assaying physiological factors like metabolic rates of such mutants in addition to the chronological lifespan measures could provide further

insights into aging mechanisms[133]. In our studies, both the strains (N2 wild-type and *daf-2* mutant) are cultured and maintained at identical conditions (room temperature 22° C) and care was taken to perform the measurements under the same environmental conditions (inner shield temperature 25 °C, flow rate 100 nl $min^{-1}$) for a consistent comparison. We performed metabolic rate measurements on adult wild-type and *daf-2* mutant worms as they age from Day 1 – Day 4 and observed significant difference in metabolic heat outputs (wild-type: 92.2 ± 17 nW, *daf-2*: 53.9 ± 8.7 nW) between both genotypes (Fig. 4.5a). In the case of wild-type, an increase in AMR from 78.3 ± 11.6 nW to 108.1 ± 9.1 nW is observed as the worm progresses from Day 1 – Day 4 (Fig. 4.5b). The metabolic rates of *daf-2* reveal a significant metabolic shift to lower rates with Day 1 worms showing an AMR of 61.8 ± 5.8 nW, which further drops to 45 ± 5.8 nW on Day 4. We note that the variations (±12 nW maximum) observed in the metabolic heat outputs of worms of the same age may result from the limited duration from which the AMR is determined, differences in the time of day when the measurements were taken or individual physiological variability, which further highlights our instrument's capability to discern such differences. Based on the size measurements from CCD images, we also report age-dependent mass-specific AMR (Fig. 4.5c) of the same sample set described above where it is known that metabolic rate normalized with protein content is negatively correlated with age of the adult worms[150]. We observe that the mass-specific AMRs of Day 1 wild-type and *daf-2* worms are significantly different with average values of 69.3 ± 9.6 μW $mg^{-1}$ and 36.1 ± 5.7 μW $mg^{-1}$ respectively, which further reduced to 42.9 ± 3.8 μW $mg^{-1}$ and 27.8 ± 7.3 μW $mg^{-1}$ on Day 4. The rate of decrease in mass-specific AMR of *daf-2* (~ -2.7 μW $mg^{-1}$ $day^{-1}$) is significantly small compared to that of wild-type (~ -9 μW $mg^{-1}$ $day^{-1}$), suggesting a potential mechanism for increased longevity.

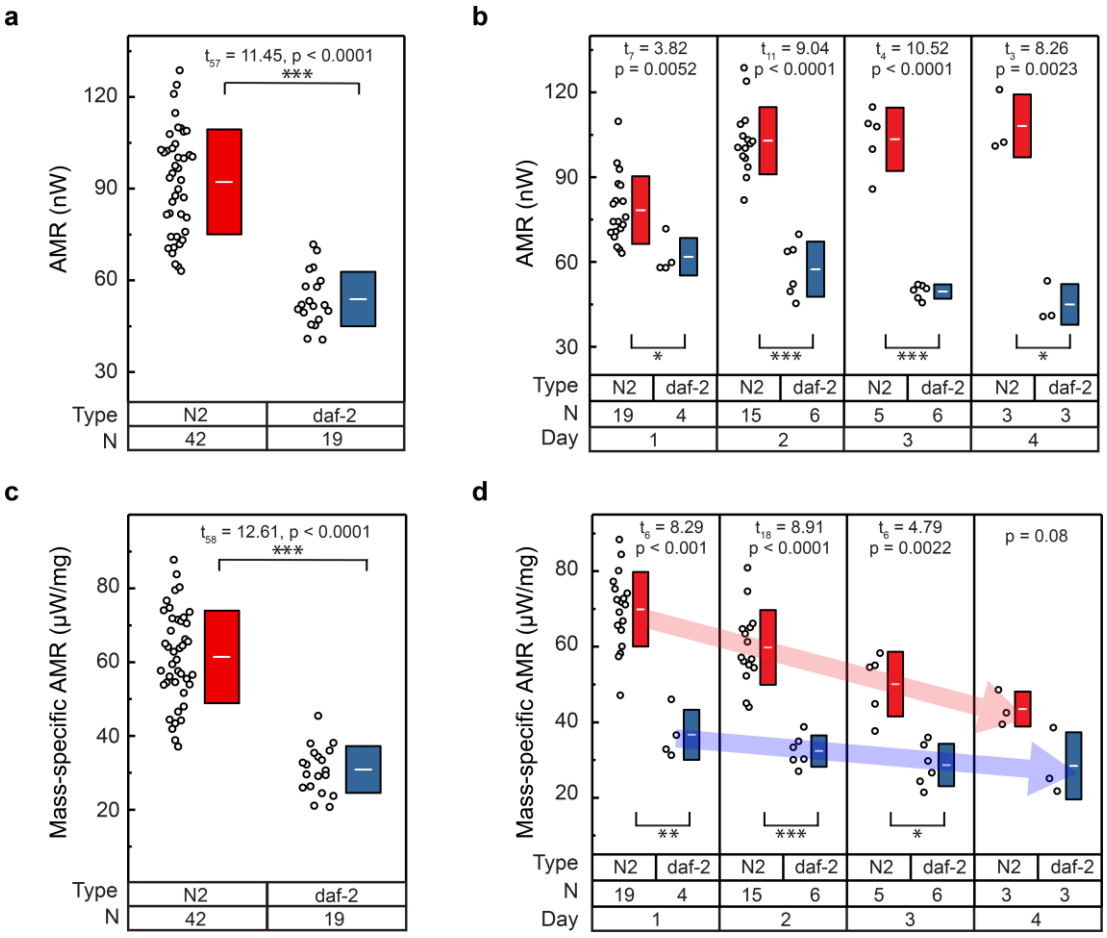


*Figure 4.5 Age-dependent metabolic heat output measurements on N2 wild-type and daf-2 mutant.*

*(a) AMR from 52 worms of wild-type and 19 worms of daf-2 from Day 1 - Day 4. The white line in the center of the box represents the mean value of the corresponding set, while the height of the box represents the standard deviation (±SD). N indicates the corresponding number of samples. (b) AMR of several worms (black circles) of wild-type (red) and daf-2 (blue) from Adult Day 1 to Day 4. (c) Mass-specific AMR of the sample set in fig. 5a. (d) Mass-specific AMR is plotted for the same sample set in fig. 5b. Statistical analysis was performed using two-tailed t-test. Statistical significance was determined for p<0.05; *p<0.01, **p<0.001, ***p<0.0001.*

## *4.5* Methods

### Fabrication of the calorimeter

Each capillary is a 20 mm long, hollow, borosilicate capillary tube (250 × 250 μm, wall thickness 50 μm) coated with 100 nm thick gold on all sides except a small portion (~2 mm) in the center to provide optical access for imaging. A 125 μm-diameter borosilicate rod is placed close to the center for localizing the *C. elegans* movement to the center of the capillary tube (Fig. 4.1a). The borosilicate capillary tube has the advantage of transparency for optical imaging and low

thermal conductivity, while the square cross-section with the flat surface aids in imaging by avoiding the aberrations due to the curvature.

A schematic of the fabrication process for the calorimetric system is shown in Figure 4.7. The tubes (VitroTubesTM) are first cleaned in an oxygen plasma cleaner to remove organic contaminants and improve surface adhesion for further processing. They are then masked with Kapton tape before being sputtered with Ti/Au (10/100 nm) thin films in the next two steps. The first mask (~400 μm across) in the center provides the isolated electrical leads, while the second mask (~2 mm) on the opposite surface generates a window for optical access. The Au-layer thickness is chosen to reduce the radiative coupling of the tube to the outer shield while minimizing the thermal conductance along the tube and maintaining a high quality film for uninterrupted electrical current flow. A 10 kΩ thermistor (Murata Electronics, -4% TCR, 0603 metric) is then soldered between the two leads. The tubes are flipped and mounted on the IS, where the electrical isolation between the IS and tubes is achieved by incorporating a 100 μm-thin glass slide while silver epoxy is used to improve thermal contact. The 125 μm diameter glass fiber is then inserted into the capillary tube and fixed at the exposed end with epoxy. Finally, a PEEK tube (360 μm/150 μm OD/ID) is connected to the capillary tube through a PEEK tubing sleeve (800 μm/400 μm OD/ID) and all the gaps are sealed with a vacuum epoxy. This tubing system is then anchored to the MS and passed through microfluidic connectors (MicroTight® Adapter PEEK 1/16" ID x 360 μm w/Fittings) on the OS that act as vacuum feedthroughs to the outside.

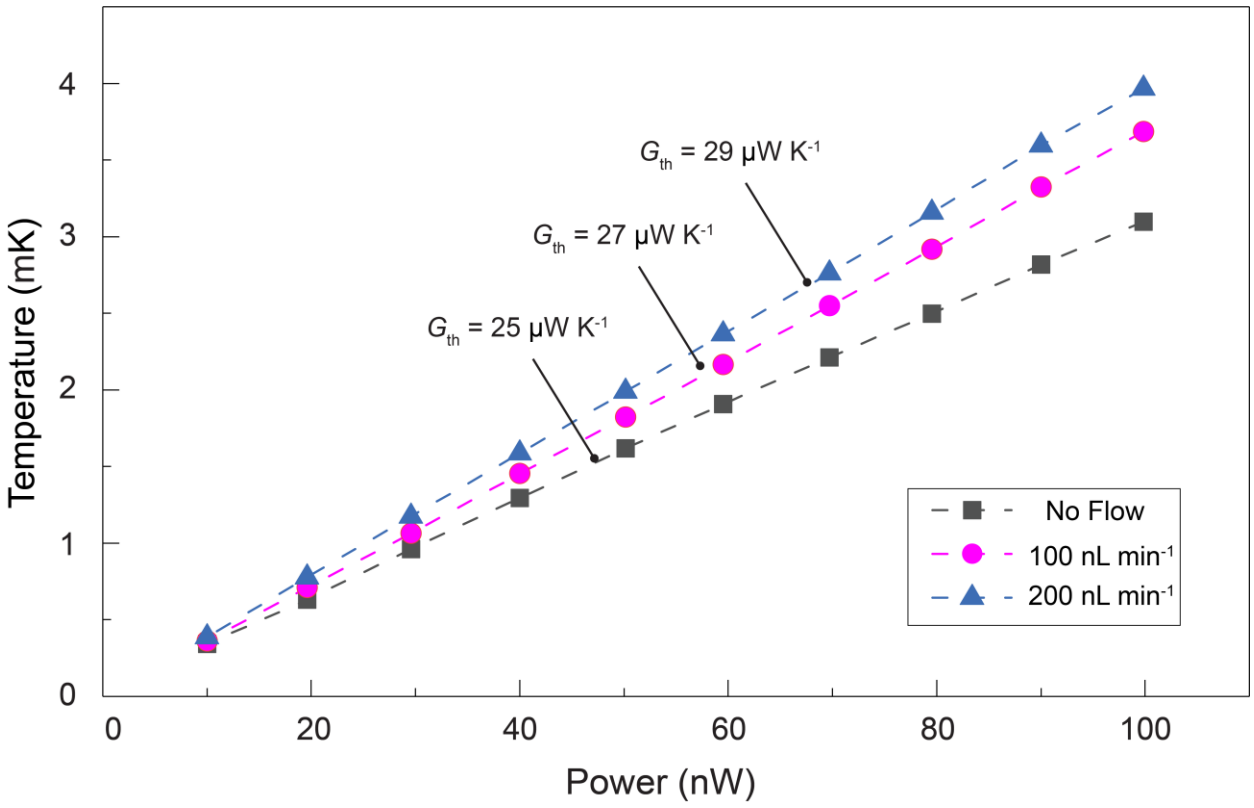


*Figure 4.6 Thermal conductance ($G_{th}$) measurement under different operation conditions.*

*The thermal conductance, $G_{th}$, increases as flow rate increases. Our metabolic heat output measurements were performed at a flow rate of 100 nL min$^{-1}$, which corresponds to a thermal conductance of 27 μW K$^{-1}$.*

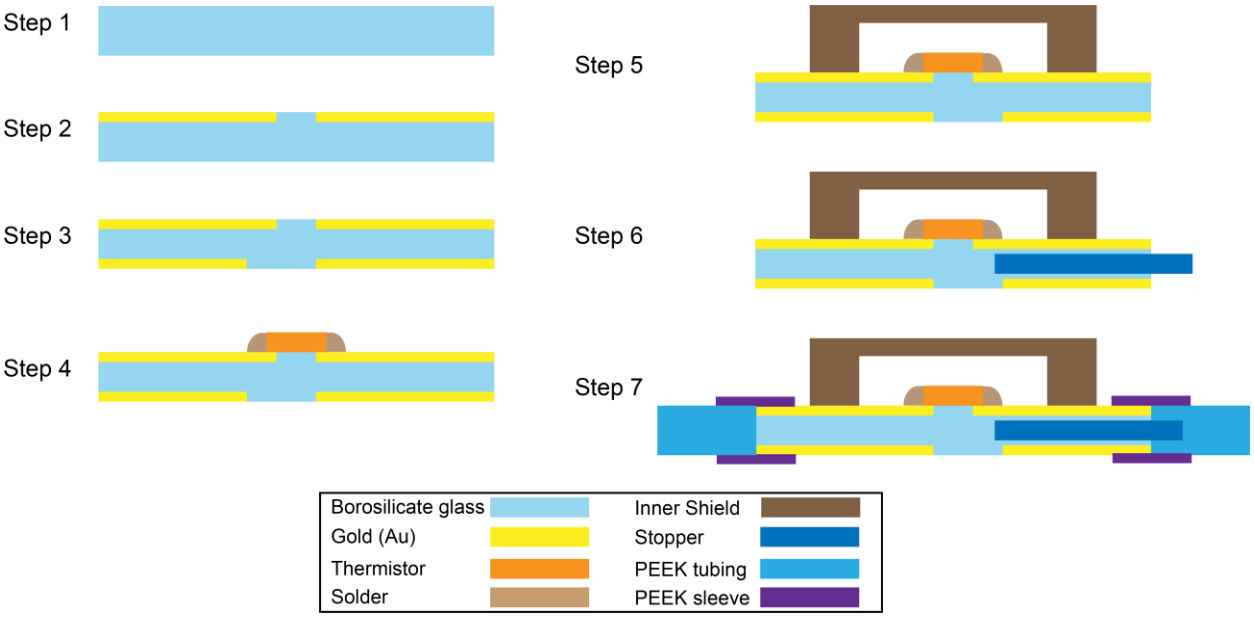

*Figure 4.7 Fabrication steps for the calorimeter.*

*(Step 1) Borosilicate capillary tubes are prepared by chemical and oxygen plasma cleaning. (Step 2) Using a shadow mask, we deposit 10/100 nm Ti/Au to form a metal coating. (Step 3) The tubes are flipped and 10/100 nm Ti/Au are deposited to cover most of the surface of the tubes, including the sides, while leaving a small access window at the center for imaging. (Step 4) A thermistor (Murata Electronics, NCP03, 10 kΩ) is positioned and soldered between the Au films deposited in step 3. (Step 5) The tubes are mounted to the Inner Shield using silver epoxy to achieve good thermal contact with the window facing downwards. (Step 6) A stopper is inserted to the inside of the tube to help localize the worms to the recording area. (Step 7) PEEK tubing is connected to the borosilicate capillary tube using PEEK tubing sleeves.*

**High stability temperature system**

To improve the temperature resolution, we built a three-shield system (Figs. 4.1a, b) with large thermal time constants to decouple high frequency temperature fluctuations from the ambient and controlled individual shield's temperature in a PID loop to reduce low frequency temperature fluctuations. The OS is a nested three-shield structure forming a vacuum enclosure (20 × 20 × 12 $cm^3$, wall thickness of 1.2 cm) with electrical, optical and fluidic feedthroughs holding vacuum down to at least 10 μTorr. Thermistors (US Sensor Corp. USP12838) are bonded to each shield in a drilled hole at a representative location using epoxy (3M Scotch-Weld Epoxy Adhesive 2216 B/A) and provide temperature feedback for PID control. Polyimide flexible heaters (Omega KH series) are attached in series to each shield on different surfaces providing uniform heat to the system. The MS (7 × 7 × 3.5 $cm^3$) with a central pocket (4 × 4 × 2 $cm^3$), is held on the bottom part of OS supported by four spherical borosilicate balls. The IS (3 × 3 × 1.2 $cm^3$) with a central pocket (2 × 0.8 × 0.6 $cm^3$), is then suspended in the MS pocket by 3 polymer supports with a spherical end. These spherical contacts provide weak thermal links (OS/MS – 50 mW $K^{-1}$ & MS/IS – 5 mW $K^{-1}$) while maintaining robust mechanical stability. From the thermal mass of copper shields and the calculated thermal conductance, the thermal time constants of the OS, MS, and IS are estimated to be 3000 s, 12000 s and 1600 s respectively, which match with the time constants obtained experimentally. The PID control scheme, as described in the following section, enables our setup to maintain OS, MS and IS temperatures to within ±1 mK, ±15 μK and ±15 μK, respectively.

**Thermometry & Temperature control of shields**

In order to measure temperature changes with μK resolution, we used resistance-based thermometry in an ac-driven Wheatstone bridge configuration (Figure 4.8). Briefly, the right half of the bridge consists of a sensing resistor on the lower branch with an associated resistance on the top while the left side is described as the matching side. Fixed resistors with ultra-low temperature coefficient of resistance (Vishay Z201 Series Z-Foil Resistors, $\pm$ 0.2 ppm $K^{-1}$) are used with the resistance values chosen to improve the stability and resolution based on previous studies[77, 155]. To balance the bridge, a fixed matching resistance equal to that of the sensing thermistor's resistance at its average temperature of operation is used while a potentiometer (Vishay Spectrol 534 series, $\pm$ 20 ppm $K^{-1}$) is used on the top branch of the matching side for fine tuning. The bridge is excited by a sinusoidal voltage ($V_{AC}$ = 1V peak-to-peak) using a waveform generator (Agilent 33210) at frequencies in the range of 10-100 Hz (frequencies were selected to avoid crosstalk). We note that this sinusoidal voltage dissipates ~0.5 μW in the calorimeter, causing the sensing capillary temperature to rise by 20 mK above the baseline temperature without sinusoidal excitation. The matching and the sensing signals are then fed into an instrumentation amplifier (Analog Devices AD524) where the common-mode signal is subtracted, and differential mode AC signals are amplified (Gain = 100 and Gain drift is at most 25 ppm $K^{-1}$). The amplitude of this amplified signal is then measured in a lock-in scheme (SRS 830) at a bandwidth of 0.1 Hz and recorded using a data acquisition card (PCI-6014) in the LabVIEW environment. The temperature resolution of the resulting circuit is quantified to be ±5 μK. As shown in Fig. 4.2c, $T_{sen}$ and $T_{mat}$ are the temperatures of the sensing and the matching capillary tube and are measured by employing the corresponding thermistors in two independent circuits based on the thermometry described above.

To provide current to the polyimide heaters introduced above, we developed a voltage-controlled current source (Fig. 4.8) where the emitter voltage of the transistor is controlled through an op-amp with the polyimide heater on the collector side. This op-amp is configured to sum a manual voltage signal ($V_{man}$) providing heat to reach the desired temperature and a controlled voltage signal ($V_{PID}$) to stabilize the temperature at that set-point in a PID loop (Fig. 4.8). The temperature measured from the Wheatstone bridge circuit acts as feedback to the PID controller (implemented in Labview) whose output controls $V_{PID.}$ Preliminary PID parameters were obtained from the step response of each thermal system using SIMC criterion[156] and were further manually tuned to minimize the temperature fluctuations.

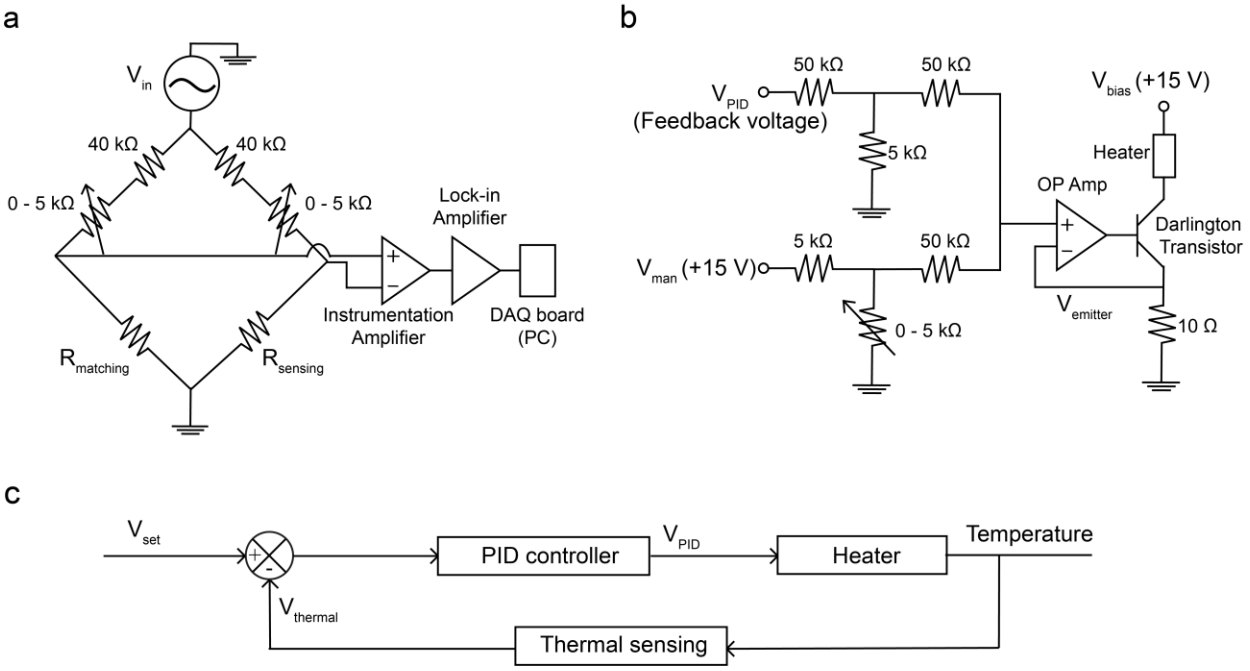


*Figure 4.8 Electronic circuit diagram and schematic of the Proportion Integral Derivative (PID) controller employed for temperature control.*

***(a)*** *Circuit diagram for the calorimetric temperature measurement and shields' temperature measurement. When the resistance of the sensing thermistor, $R_{sensing}$, changes due to the heat production by C. elegans at the center of the tube, an ac voltage difference, $V_{sensing} - V_{matching}$, develops across the bridge. When the resistance of the sensing thermistor, $R_{sensing}$, changes due to environmental temperature drift, similar changes also arise in the resistance of the matching thermistor $R_{matching}$ and keep the bridge voltage balanced, thus attenuating detrimental effects of temperature drift. The ac output voltage of the bridge circuit is amplified in an instrumentation amplifier (Analog Devices, AD524) and demodulated with a Lock-in Amplifier (Stanford Research Systems, SR830). This output voltage, $V_{thermal}$, is digitized via a data acquisition board (National Instruments, PCI-6014) and a custom LabView (National Instruments)*

*program. We note that similar circuits are used for sensing the shields' temperature by incorporating a precision fixed resistor as $R_{matching}$.* ***(b)*** *Schematic of the circuit employed to drive the heater. $V_{man}$ is set to a specific value to supply a constant current to the resistive heater. $V_{PID}$ is added to $V_{man}$ to adjust the current supplied to the heater by controlling the transistor emitter voltage. The current to the heater is set by $V_{emitter}$ divided by 10 Ohm.* ***(c)*** *Block diagram of PID feedback loop. Temperature is controlled stably through a PID control system. $V_{thermal}$ is compared to $V_{set}$ and a net voltage is delivered to PID controller. $V_{PID}$ adjusts the current flow through the resistive heaters (as shown in (b)) and the controlled temperature is read by thermal sensing circuit (as shown in (a)). This loop continues to maintain $V_{thermal}$ to be $V_{set}$.*

## Optical imaging

Our calorimeter incorporates good optical access to the central region of the sensing capillary tube, which aids in trapping and monitoring the activity of the *C. elegans*. Though systems employing multiple shields to achieve thermal stability are well established, integrating an optical imaging capability is challenging as this naturally couples environmental fluctuations into the system through radiative coupling and the illumination source. A combination of IR reflective (Hot Mirror-Edmund Optics) and IR absorptive (Heat absorbing KG5 Schott filter) windows, sealed to the bottom part of the OS (Fig. 4.1b) reduce the coupling to the outer environment by reflecting IR radiation (~90%) to the environment and absorbing the remaining transmitted radiation. The temperature-controlled calorimeter is mounted on an inverted microscope (ZEISS Axiovert 200) and imaging is performed with epi-illumination through a 10x objective (CFI Plan Fluor DL 10XF). A DC power supply (Agilent 6033A) provides power (3V, 0.75A) to the Halogen light source while a CCD camera (RET-4000R-F-M-12-C) controlled through Micro-Manager 1.4.22 acquires images at 1 frame per second. The minimum illumination that provides a legible image at an exposure time of 0.5 sec is chosen to minimize thermal instabilities due to the light source fluctuations. This illumination results in a temperature rise of ~1 mK (corresponding to ~27 nW) on both sensing and matching capillary tubes. We note that all thermal signals reported here were measured under this illumination setting.

## Estimating the size and activity of *C. elegans*

The mass/volume of an individual *C. elegans* needed for obtaining the mass-specific properties was estimated from the images captured during the measurement. Considering the axi-symmetric structure of the worm, the body is carefully divided into small sections of cylinders[157] along the length of worm (see Fig. 4.9a). The relevant dimensions (pixel lengths) for each section (diameter $D_n$ and width $H_n$) were measured in ImageJ with the appropriate calibration of the microscope's magnification. The volume of the worm is the sum of the volumes of all cylindrical sections. The mass of each worm is then derived from the total estimated volume with the density considered to be ~ 1.08 g/cc[158].

$$Volume = \sum_{n=1}^{N} \frac{\pi D_n^2 H_n}{4} \tag{4-1}$$

An activity factor is defined to quantitatively represent the worm's activity which is derived by performing the following image analysis in ImageJ on a stack of images collected during the measurement at a frame rate of 1 sec. Initial brightness and contrast adjustments are performed on two image stacks, where the second image stack is a duplicate of the first with a single frame offset. The two stacks are then subtracted to create a new stack which now represents the worm activity, i.e. subtracting a frame at $(n+1)^{th}$ sec (Fig. 4.9b) from that at the $n^{th}$ sec eliminates the motionless background and captures only the movement of the worm. To quantify this movement, the mean pixel intensity of each frame was then calculated and converted to a dimensionless activity factor ranging from 0 to1, where 0 and 1 indicate the lowest and the highest activity levels of a given worm. We note that absolute quantities can be used for activity comparison between wild-type and *daf-2* worms, instead of normalized quantities.

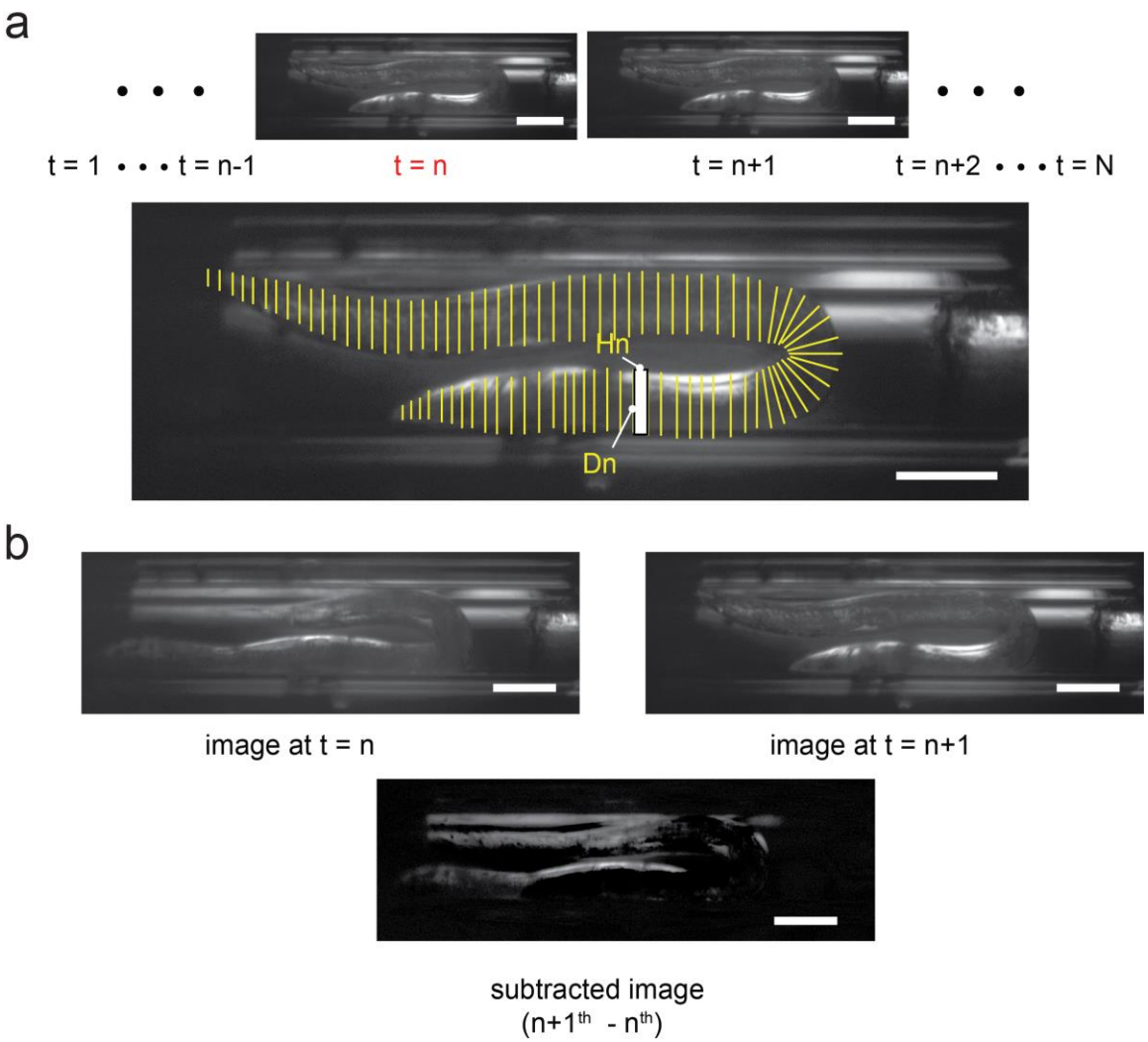


*Figure 4.9 Size measurement and analysis of C. elegans.*

*(a) C. elegans size measurement. (Step 1) Choose a clear image from the acquired image stack. (Step 2) Divide the organism into small sections manually. (Step 3) Sum all volumes by acquiring the diameter ($D_n$) and width ($H_n$) of small cylinders. This procedure, applied to independent images (n = 3) in the stack, resulted in similar volumes to within ±5%. The process was repeated for every independent metabolic heat output measurement (n = 61 for N2 wild-type and n = 19 for daf-2) (b) Activity analysis of C. elegans: An image at time t = n, corresponding to the $n^{th}$ image in the stack (top-panel), is subtracted pixel-by-pixel from the $n+1^{th}$ image (middle panel) at time t = n+1, resulting in the subtracted image (bottom panel). The mean intensity (brightness) of all pixels in the subtracted image is calculated to define an activity factor (see Methods section) and indicates the movement of the worm at that point in time during the recording. Scale bars: 100 μm.*

**Thermal conductance measurement and power resolution**

To experimentally quantify the thermal conductance of our capillary system, DC power is input at the center of the capillary tube by superimposing a DC voltage offset ($V_{DC}$) on top of the sensing AC voltage ($V_{AC}$), which causes a DC temperature rise ($T_{DC}$) of the sensing capillary tube

corresponding to the power expenditure of $P_{DC} = \frac{V_{DC}^2}{R_{th}}$, where $R_{th}$ is the nominal electrical resistance of the thermistor at room temperature (~10 kΩ). The resultant temperature rise is measured by the same thermistor using the thermometry scheme discussed above with a bandwidth of 5 mHz. The slope of $P_{DC}$ with respect to $T_{DC}$ corresponds to the thermal conductance $G_{th}$ of the capillary system. As shown in Fig. 4.2a, we dissipated power in the calorimeter from 10 nW to 100 nW in steps of 10 nW and measured corresponding temperature rises from 0.37 mK to 3.7 mK. From the slope of this plot, we estimate the thermal conductance of the capillary tube to be 27 μW $K^{-1}$. Further, to test the response of our calorimeter to sub-nW inputs, we varied the offset voltage ($V_{DC}$) from 1 mV to 3 mV in steps of 0.2 mV. This corresponds to a power dissipation of ~100 pW to ~1 nW in the calorimeter. In the inset of Fig. 4.2a, we plot this temperature rise with respect to the power dissipation. The data points shown in the plot correspond to mean values of four independent measurements performed for each power input while the error bars represent standard deviation in the temperature rise. From the observed standard deviation of 5 μK, we estimate the noise floor to be 10 μK (the maximum standard deviation observed at different heat inputs). Thus, the minimum precisely measurable power change using our calorimeter is defined as the noise floor and is estimated to be 270 pW (corresponding to temperature drift of ~10 μK). We note that the theoretical electronic noise in our system considering Johnson noise, shot noise, voltage source noise and the noise added at the amplifier inputs corresponds to a NET of <1 μK in a bandwidth of 5 mHz. But the inherent long-term drift in our system, unintended radiative coupling to the outer shield and added noise in the data acquisition result in the increased NET of 10 μK (270 pW). Thus, a resolution of less than 100 pW is potentially possible by carefully addressing long term drift. Further, to establish the sub-nW resolution of our system, a DC offset voltage ($V_{DC}$) of ~1.6 mV, corresponding to power dissipation of 270 pW (thermal pulse in Fig. 4.2b) is applied and the

resulting steps in temperature rise of 10 μK can be clearly observed in Fig. 4.2b. Similarly, a square pulse with an amplitude of ~16 mV, corresponding to a power dissipation of 27 nW, is applied to estimate the time constant of our system to be 100 s (Fig. 4.2d).

**Sample preparation and control**

The nematodes were maintained at 20 °C on NGM agar plates with OP50 *E. coli* as food source, according to standard protocols[159]. The following strains were used in our studies: Bristol N2 (used as wild-type), *daf-2(e1370).* For heat output measurements, the worms were transferred to the sensing capillary tube at 25 °C, which was filled with S-basal buffer.

## 4.6 Conclusion

We have performed direct, high-resolution calorimetric heat measurements and related them to the physiological state of individual *C. elegans* via simultaneous optical measurements. Cellular processes (e.g. energy conversion, gene expression, signal transduction, cell division) are not 100% efficient and are always accompanied by heat dissipation. Therefore, the proposed continuous opto-calorimetric measurements from individual organisms can enable direct heat output quantification of the metabolic contributions of various intracellular processes. This sub-nW resolution (~270 pW with a temporal resolution of 100 sec) direct calorimeter was accomplished by a combination of low thermal conductance capillary tubes ($G_{th}$ ~ 27 μW $K^{-1}$) and high-resolution ($\Delta T$ ~ 10 μK) thermometry. This resolution presents more than two orders of magnitude improvement over the best calorimeters previously employed[143] in *C. elegans* studies and one order of magnitude resolution improvement over the most sensitive calorimeter[144] employed to date for biological studies. We demonstrate the usefulness of this

instrument for studies on *C. elegans* by conducting a series of measurements on larval and adult stages. In fact, this work represents the first metabolic rate measurement on a single *C. elegans* from L1 to the adult stage. In addition, our calorimeter captures variations of metabolic heat generation corresponding to the worm's locomotive activity, which is shown to be about 5 - 25% above the SMR. Further, the worm's metabolic responses to external stimuli, like temperature and oxygen deprivation, may also be explored in our system. This method can be combined with other metabolomics approaches where mass-spectrometry can be used to profile metabolites in cells. Calorimetric approaches overcome some of the limitations posed by metabolomics approaches: for example, destructive sample preparation prevents continuous, time-resolved measurements and relating detected biomarkers to biological mechanisms is challenging. Finally, we note that our calorimeter, built from commercially available parts, without involving any complicated microfabrication processes, can in principle be employed to study metabolism of several other model organisms (e.g. Chlamydomonas, Brown fat cells) whose metabolic output is in the nanowatt range.

# Chapter 5 Summary and Outlook

## 5.1 Summary

In this dissertation, I presented my work related to both near-field radiative heat transfer between different material systems and the development of a bio-calorimeter for measuring metabolic rates of individual *C. elegans* worms. In the first chapter, I provided a brief review of the near-field radiative heat transfer and thermophotovoltaic energy conversion to give a sense of where the field is heading.

In the second chapter, I discussed my work on near-field RHT measurements between $MgF_2$ and $Al_2O_3$ devices. While $SiO_2$ has remained the state-of-the-art material for exploring near-field RHT, it is in no way the best polar material for RHT. I have demonstrated through a series of near-field measurements that near-field RHT between $MgF_2$ plates is 2.5 times more than that of $SiO_2$. I have also presented the results obtained from measurements on $Al_2O_3$ which indicated a modest 1.5 times enhancement over $SiO_2$. Finally, I discussed other materials with potential improvements above that of $SiO_2$.

In the third chapter, I described my initial work on developing devices for probing near-field thermophotovoltaic energy conversion. By placing this device at known-nanometric separations from a commercial PV cell, we have shown that the power output can be enhanced by up to 40 times as compared to the far-field. Extending this work, I have developed emitters that could be heated to ~1300 K and showed that power extraction of up to 5 $kW/m^2$ at an efficiency

of 6.7% can be obtained at a separation of 100 nm. Further, I discussed the performance of the system as a function of both temperature and gap sizes.

Finally, I discussed the development of a calorimeter with sub-nW resolution that is compatible for metabolic studies on living organisms. Specifically, I discussed the design and development of the tool leading to a 270-pW heat resolution. Using this tool, we monitored metabolic heat rate measurements from wild-type *C. elegans* as a function of their age. Further, we also reported measurements on *daf-2* variant which revealed a shift in metabolic activity as compared to wild-type worms.

## 5.2 Outlook

Thermal radiation has garnered ever increasing interest in the thermal research community due to the numerous novel phenomena that arise at the nanoscale. A lot of fundamental questions still need to be answered and systems improved to make feasible translation into real-life devices. In the following paragraphs, I will discuss the future work that I believe would push the boundaries of what we know about near-field radiative heat transfer.

### *5.2.1 Near-field radiative heat transfer*

The presence of a strong phonon resonance in $MgF_2$ enables immediate improvements to novel thermal devices such as thermal diodes. A radiative thermal diode formed between $MgF_2$ and vanadium oxide devices can enable rectification coefficients of up to 0.67. The enhanced RHT as compared to $SiO_2$ directly translates to this improved coefficient. The work on near-field RHT measurements on $MgF_2$ and $Al_2O_3$ stemmed from the fundamental need to understand the limits to RHT. It is intriguing to question the limits to near-field RHT based on polar dielectrics. Since most studies assume crystalline materials for theoretical calculations, it may be interesting to

consider amorphous nature of the films which has a direct effect on the phonon-phonon scattering. Further, theoretical studies have shown that maximum RHT can be attained in Drude materials with optimized parameters. The measurements made possible on materials that are deposited using standard deposition techniques open up avenues for exploring other materials that can further enhance the RHT. For example, transparent conductive oxides (TCOs) are a class of materials that can be doped in a wide range. Doping is significant in defining the plasmon resonance in Drude materials and TCOs are particularly interesting in this regard as they possess relatively smaller background permittivities as compared to doped silicon.

Experimental studies on thin-films have been scarce but interesting because of the predictions of increased local density of states. This relies on the thin-film surrounded on both sides by material with permittivity close to that of vacuum ($n = 1$). Since it is practically challenging to make suspended thin-films, it may be beneficial to consider materials with low refractive indices in the wavelength range of interest, for example, several halides (KBr, LiF etc.). Polymers PMMA, parylene etc. are another class of materials with refractive indices close to 1.

### *5.2.2 Near-field thermophotovoltaic energy conversion*

Near-field TPV systems have potential ramifications in fundamental studies and real-life devices. The near-field TPV system reported in this dissertation can be further improved by making the following interventions. First, employing an air-bridge PV cell can immediately improve the efficiency up to ~19% at 1300 K, by reflecting sub band-gap photons that are otherwise absorbed in Au. But realizing this experimentally is quite challenging due to the practical difficulties in suspending a thin-film and keeping it flat and clean. Further, improving the emitter devices to be able to heat to further higher temperatures can improve the spectral match with the band-gap of the PV cell. For example, an emitter heated to 1500 K will result in efficiencies higher

than 30%. Another gain in the overall efficiency can be obtained by suppressing the unintended sub-band gap absorption at higher wavelengths due to SPhP coupling. By depositing a sufficiently thick film of amorphous silicon on top of the PV cell, the SPhPs can be suppressed, further improving the efficiency.

Further gains in efficiencies can be obtained by improving the open-circuit voltage, minimizing the series resistance and increasing the shunt resistance. The open-circuit voltage can be enhanced by employing a hotter emitter, thus increasing the photocurrent. This inadvertently increases the series resistance, hurting the total power generated. In fact, at high-injection levels, it becomes critical to collect electrons/holes close to the source of generation. The contact resistance can be minimized by designing an electrical grid on the top of the PV cell. This, along with the deposition of amorphous silicon should enable immediate gains in efficiency. Efforts to reduce the dark current during the material growth itself can also improve the open-circuit voltage and thus efficiency.

In the experimental front, the measurements can be improved by measuring the temperature of the emitter in real-time. This can be either done optically or by using the resistance of the emitter as an indicator of temperature. Resistance thermometry at high temperatures is prone to drifts due to diffusion of charge carriers and electro-migration. Since the optical properties of the material are consistent with increasing temperature, it may benefit from using an optical technique to measure temperature. Efforts were made to develop such a technique which is based on collecting the radiation emitted from the backside of the emitter. The radiation collected from the backside can then be measured in a photodetector and the temperature calculated using a pre-determined calibration. The temperature changes thus measured as a function of gap size can enable direct measurement of near-field radiative heat fluxes. This provides a simultaneous measurement of

electric power generation and the total radiative heat flux. Further, the optical setup designed for measuring the temperature can also be used to pump green laser on the backside of the emitter and heat it optically. The resistance of the emitter can then act as a temperature read-out.

The doped silicon emitters can also enable studies on PV cells with bandgaps lower than that of the current InGaAs cell. Employing a commercial PV cell with bandgap of ~0.3 eV and the emitter at 1300 K should enable large efficiencies. While low band-gap PV cells suffer from large non-radiative recombination losses, the gains attained due to the spectral match make them potential candidates for exploring improved TPV performance, especially in the low temperature range (600 – 1000 K).

### *5.2.3 Bio-calorimeter*

The bio-calorimeter described in this dissertation boasts a heat resolution of 270 pW. The system can be improved in terms of the heat resolution and time constant. The heat resolution can be improved by reducing the capillary size to smaller dimensions. In fact, up to 5 μW/K - a five-fold improvement over the current calorimeter - can be built from commercially available capillary tubes with dimensions of 50 × 50 μm OD and 30 × 30 μm ID. At these scales, it is important to sufficiently minimize the radiative component by appropriately coating all surfaces with reflective metals. The Johnson-noise limited temperature resolution of the thermometry is ~2 μK, while experimentally the smallest temperature resolution obtained is ~10 μK. This is limited by the unavoidable drift in the temperature of the thermistor owing to its significant radiative coupling either to the outer shield or to the environment outside the calorimeter. Reducing the bandwidth of the temperature measurement can improve the resolution, but this would increase the total time constant of the measurement. Thus, in the short-term, heat resolutions of ~10 pW can be obtained

by tackling the challenges mentioned above. Such heat resolutions would be necessary to perform metabolic rate measurements from single cells such as brown fat cells or even HeLa cells.

The calorimetry can also gain significantly from employing a thin-film thermistor instead of a commercially purchased thermistor. Particularly, as the capillary is minimized, the capacitance of the system is dominated by the relatively large thermistor. Thus, by reducing the thermistor to a thin-film, potentially based on vanadium oxide or niobium nitride whose TCR is in the similar range, the time constant can be minimized and the coupling to the outer shield can be reduced. Thus, the temperature resolution may also improve due to the reduced coupling to the surroundings. Further, in order to make better use of the highly stable middle and inner shields, the fluidic systems can be designed to have larger area of contact with the shields. These engineering improvements can lead to new calorimeters to explore (physiological or molecular) mechanisms at the single cell level.

## Bibliography


1. Incropera, F.P., et al., *Fundamentals of heat and mass transfer.* 2007.

2. Planck, M., *The theory of heat radiation.* 2nd ed. (P. Blakiston's Son & Co., Philadelphia, PA), 1914.

3. Rytov, S., Y. Kravtsov, and V. Tatarskii, *Principles of statistical radiophysics* Vol. 3 (Springer, Berlin, 1989).

4. Polder, D. and M. Vanhove, *Theory of radiative heat transfer between closely spaced bodies.* Phys. Rev. B, 1971. **4**(10): p. 3303-3314.

5. Callen, H.B. and T.A. Welton, *Irreversibility and generalized noise.* Phys. Rev., 1951. **83**(1): p. 34-40.

6. Kubo, R., *The fluctuation-dissipation theorem.* Rep. Prog. Phys., 1966. **29**(255): p. 255.

7. Hargreaves, C.M., *Anomalous Radiative Transfer between Closely-Spaced Bodies.* Physics Letters A, 1969. **A 30**(9): p. 491-492.

8. Domoto, G.A., R.F. Boehm, and C.L. Tien, *Experimental Investigation of Radiative Transfer between Metallic Surfaces at Cryogenic Temperatures.* Journal of Heat Transfer, 1970. **92**(3): p. 412-416.

9. Kittel, A., et al., *Near-field heat transfer in a scanning thermal microscope.* Physical Review Letters, 2005. **95**(22).

10. Hu, L., et al., *Near-field thermal radiation between two closely spaced glass plates exceeding Planck's blackbody radiation law.* Applied Physics Letters, 2008. **92**(13).

11. Narayanaswamy, A., S. Shen, and G. Chen, *Near-field radiative heat transfer between a sphere and a substrate.* Physical Review B, 2008. **78**(11).

12. Rousseau, E., et al., *Radiative heat transfer at the nanoscale.* Nature Photonics, 2009. **3**(9): p. 514-517.

13. Shen, S., A. Narayanaswamy, and G. Chen, *Surface Phonon Polaritons Mediated Energy Transfer between Nanoscale Gaps.* Nano Letters, 2009. **9**(8): p. 2909-2913.

14. Kim, K., et al., *Radiative heat transfer in the extreme near field.* Nature, 2015. **528**(7582): p. 387-391.

15. Song, B., et al., *Enhancement of near-field radiative heat transfer using polar dielectric thin films.* Nat. Nanotechnol., 2015. **10**(3): p. 253-258.

16. St-Gelais, R., et al., *Demonstration of Strong Near-Field Radiative Heat Transfer between Integrated Nanostructures.* Nano Letters, 2014. **14**(12): p. 6971-6975.

17. Lim, M., S.S. Lee, and B.J. Lee, *Near-field thermal radiation between doped silicon plates at nanoscale gaps.* Physical Review B, 2015. **91**(19).

18. Bernardi, M.P., D. Milovich, and M. Francoeur, *Radiative heat transfer exceeding the blackbody limit between macroscale planar surfaces separated by a nanosize vacuum gap.* Nat. Commun., 2016. **7**: p. 12900.

19. Fiorino, A., et al., *Giant Enhancement in Radiative Heat Transfer in Sub-30 nm Gaps of Plane Parallel Surfaces.* Nano Letters, 2018. **18**(6): p. 3711-3715.

20. Song, B., et al., *Radiative heat conductances between dielectric and metallic parallel plates with nanoscale gaps.* Nature Nanotechnology, 2016. **11**(6): p. 509-514.

21. Salihoglu, H., et al., *Near-field thermal radiation between two plates with sub-10 nm vacuum separation.* Nano Lett., 2020. **20**(8): p. 6091-6096.

22. DeSutter, J., L. Tang, and M. Francoeur, *A near-field radiative heat transfer device.* Nature Nanotechnology, 2019. **14**(8): p. 751-755.

23. Ghashami, M., et al., *Precision Measurement of Phonon-Polaritonic Near-Field Energy Transfer between Macroscale Planar Structures Under Large Thermal Gradients.* Physical Review Letters, 2018. **120**(17).

24. Fiorino, A., et al., *A Thermal Diode Based on Nanoscale Thermal Radiation.* Acs Nano, 2018. **12**(6): p. 5774-5779.

25. Song, B., et al., *Near-field radiative thermal transport: From theory to experiment.* Aip Advances, 2015. **5**(5).

26. Lucchesi, C., R. Vaillon, and P.O. Chapuis, *Radiative heat transfer at the nanoscale: experimental trends and challenges.* Nanoscale Horizons, 2021. **6**(3): p. 201-208.

27. Biehs, S.A., et al., *Near-field radiative heat transfer in many-body systems.* Reviews of Modern Physics, 2021. **93**(2).

28. Cuevas, J.C. and F.J. Garcia-Vidal, *Radiative Heat Transfer.* Acs Photonics, 2018. **5**(10): p. 3896-3915.

29. Song, J., et al., *Many-body near-field radiative heat transfer: methods, functionalities and applications.* Rep Prog Phys, 2021.

30. Basu, S., Z.M. Zhang, and C.J. Fu, *Review of near-field thermal radiation and its application to energy conversion.* International Journal of Energy Research, 2009. **33**(13): p. 1203-1232.

31. Salihoglu, H., et al., *Near-Field Thermal Radiation between Two Plates with Sub-10 nm Vacuum Separation.* Nano Letters, 2020. **20**(8): p. 6091-6096.

32. St-Gelais, R., et al., *Near-field radiative heat transfer between parallel structures in the deep subwavelength regime.* Nature Nanotechnology, 2016. **11**(6): p. 515-519.

33. Tang, L., J. DeSutter, and M. Francoeur, *Near-Field Radiative Heat Transfer between Dissimilar Materials Mediated by Coupled Surface Phonon- and Plasmon-Polaritons.* Acs Photonics, 2020. **7**(5): p. 1304-1311.

34. Sabbaghi, P., et al., *Super-Planckian radiative heat transfer between macroscale metallic surfaces due to near-field and thin-film effects.* Journal of Applied Physics, 2020. **128**(2).

35. Lim, M., et al., *Tailoring near-field thermal radiation between metallo-dielectric multilayers using coupled surface plasmon polaritons.* Nature Communications, 2018. **9**.

36. Wang, X.J., S. Basu, and Z.M. Zhang, *Parametric optimization of dielectric functions for maximizing nanoscale radiative transfer.* Journal of Physics D-Applied Physics, 2009. **42**(24).

37. Nefzaoui, E., et al., *Maximal near-field radiative heat transfer between two plates.* European Physical Journal-Applied Physics, 2013. **63**(3).

38. Mulet, J.P., et al., *Enhanced radiative heat transfer at nanometric distances.* Microscale Thermophysical Engineering, 2002. **6**(3): p. 209-222.

39. Zhang, L. and O.D. Miller, *Optimal Materials for Maximum Large-Area Near-Field Radiative Heat Transfer.* Acs Photonics, 2020. **7**(11): p. 3116-3129.

40. Biehs, S.A., M. Tschikin, and P. Ben-Abdallah, *Hyperbolic Metamaterials as an Analog of a Blackbody in the Near Field.* Physical Review Letters, 2012. **109**(10).

41. Liu, X.L., R.Z. Zhang, and Z.M. Zhang, *Near-field radiative heat transfer with doped-silicon nanostructured metamaterials.* International Journal of Heat and Mass Transfer, 2014. **73**: p. 389-398.

42. Fernandez-Hurtado, V., et al., *Enhancing Near-Field Radiative Heat Transfer with Si-based Metasurfaces.* Physical Review Letters, 2017. **118**(20).

43. Liu, X.L. and Z.M. Zhang, *Near-Field Thermal Radiation between Metasurfaces.* Acs Photonics, 2015. **2**(9): p. 1320-1326.

44. Ben-Abdallah, P., et al., *Near-field heat transfer mediated by surface wave hybridization between two films.* Journal of Applied Physics, 2009. **106**(4).

45. Iizuka, H. and S. Fan, *Significant Enhancement of Near-Field Electromagnetic Heat Transfer in a Multilayer Structure through Multiple Surface-States Coupling.* Physical Review Letters, 2018. **120**(6).

46. Francoeur, M., M.P. Menguc, and R. Vaillon, *Near-field radiative heat transfer enhancement via surface phonon polaritons coupling in thin films.* Applied Physics Letters, 2008. **93**(4).

47. Wedlock, B.D., *Thermo-Photo-Voltaic Energy Conversion.* Proceedings of the Ieee, 1963. **51**(5): p. 694-698.

48. Nelson, R.E., *A brief history of thermophotovoltaic development.* Semiconductor Science and Technology, 2003. **18**(5): p. S141-S143.

49. Crowley, C.J., et al., *Thermophotovoltaic converter performance for radioisotope power systems.* Space Technology and Applications International Forum-Staif 2005, 2005. **746**: p. 601-614.

50. Teofilo, V.L., et al., *Thermophotovoltaic energy conversion for space applications.* Space Technology and Applications International Forum - Staif 2006, 2006. **813**(552).

51. Wernsman, B., et al., *Greater than 20% radiant heat conversion efficiency of a thermophotovoltaic radiator/module system using reflective spectral control.* Ieee Transactions on Electron Devices, 2004. **51**(3): p. 512-515.

52. Omair, Z., et al., *Ultraefficient thermophotovoltaic power conversion by band-edge spectral filtering.* Proc. Natl. Acad. Sci. U S A, 2019. **116**(31): p. 15356-15361.

53. Fan, D., et al., *Near-perfect photon utilization in an air-bridge thermophotovoltaic cell.* Nature, 2020. **586**(7828): p. 237-241.

54. Pan, J.L., H.K.H. Choy, and C.G. Fonstad, *Very large radiative transfer over small distances from a black body for thermophotovoltaic applications.* Ieee Transactions on Electron Devices, 2000. **47**(1): p. 241-249.

55. Whale, M.D. and E.G. Cravalho, *Modeling and performance of microscale thermophotovoltaic energy conversion devices.* Ieee Transactions on Energy Conversion, 2002. **17**(1): p. 130-142.

56. Narayanaswamy, A. and G. Chen, *Surface modes for near field thermophotovoltaics.* Appl. Phys. Lett., 2003. **82**(20): p. 3544-3546.

57. Laroche, M., R. Carminati, and J.J. Greffet, *Near-field thermophotovoltaic energy conversion.* J. Appl. Phys., 2006. **100**(6): p. 063704.

58. Park, K., et al., *Performance analysis of near-field thermophotovoltaic devices considering absorption distribution.* J. Quant. Spectrosc. Ra., 2008. **109**(2): p. 305-316.

59. Bright, T.J., L.P. Wang, and Z.M. Zhang, *Performance of near-field thermophotovoltaic cells enhanced with a backside reflector.* J. Heat Trans-T Asme, 2014. **136**(6): p. 062701.

60. Tong, J.K., et al., *Thin-film 'thermal well' emitters and absorbers for high-efficiency thermophotovoltaics.* Sci. Rep., 2015. **5**: p. 10661.

61. Chen, K.F., P. Santhanam, and S.H. Fan, *Suppressing sub-bandgap phonon-polariton heat transfer in near-field thermophotovoltaic devices for waste heat recovery.* Appl. Phys. Lett., 2015. **107**(9): p. 091106.

62. Zhao, B., et al., *High-performance near-field thermophotovoltaics for waste heat recovery.* Nano Energy, 2017. **41**: p. 344-350.

63. Papadakis, G.T., et al., *Broadening near-field emission for performance enhancement in thermophotovoltaics.* Nano Lett., 2020. **20**(3): p. 1654-1661.

64. DiMatteo, R.S., et al., *Enhanced photogeneration of carriers in a semiconductor via coupling across a nonisothermal nanoscale vacuum gap.* Applied Physics Letters, 2001. **79**(12): p. 1894-1896.

65. Fiorino, A., et al., *Nanogap near-field thermophotovoltaics.* Nat. Nanotechnol., 2018. **13**(9): p. 806-811.

66. Inoue, T., et al., *One-chip near-field thermophotovoltaic device integrating a thin-film thermal emitter and photovoltaic cell.* Nano Lett., 2019. **19**(6): p. 3948-3952.

67. Bhatt, G.R., et al., *Integrated near-field thermo-photovoltaics for heat recycling.* Nature Communications, 2020. **11**(1).

68. Mittapally, R., et al., *Near-field thermophotovoltaics for efficient heat to electricity conversion at high power density.* Nature Communications, 2021. **12**(1).

69. Lucchesi, C., et al., *Near-Field Thermophotovoltaic Conversion with High Electrical Power Density and Cell Efficiency above 14%.* Nano Letters, 2021. **21**(11): p. 4524-4529.

70. Inoue, T., et al., *Integrated Near-Field Thermophotovoltaic Device Overcoming Blackbody Limit.* Acs Photonics, 2021. **8**(8): p. 2466-2472.

71. Fiorino, A., et al., *Nanogap near-field thermophotovoltaics.* Nature Nanotechnology, 2018. **13**(9): p. 806-811.

72. Zhu, L.X., et al., *Near-field photonic cooling through control of the chemical potential of photons.* Nature, 2019. **566**(7743): p. 239-244.

73. Ben-Abdallah, P. and S.A. Biehs, *Contactless heat flux control with photonic devices.* Aip Advances, 2015. **5**(5).

74. Otey, C.R., W.T. Lau, and S.H. Fan, *Thermal Rectification through Vacuum.* Physical Review Letters, 2010. **104**(15).

75. Jones, A.C., et al., *The thermal near-field: Coherence, spectroscopy, heat-transfer, and optical forces.* Progress in Surface Science, 2013. **88**(4): p. 349-392.

76. Ganjeh, Y., et al., *A platform to parallelize planar surfaces and control their spatial separation with nanometer resolution.* Review of Scientific Instruments, 2012. **83**(10).

77. Sadat, S., E. Meyhofer, and P. Reddy, *High resolution resistive thermometry for micro/nanoscale measurements.* Review of Scientific Instruments, 2012. **83**(8).

78. Song, B., et al., *Enhancement of near-field radiative heat transfer using polar dielectric thin films.* Nature Nanotechnology, 2015. **10**(3): p. 253-258.

79. Palik, E.D., *Handbook of optical constants of solids.* Academic Press: San Diego, 1998.

80. Basu, S., B.J. Lee, and Z.M. Zhang, *Near-Field Radiation Calculated With an Improved Dielectric Function Model for Doped Silicon.* Journal of Heat Transfer-Transactions of the Asme, 2010. **132**(2).

81. Henry, A., R. Prasher, and A. Majumdar, *Five thermal energy grand challenges for decarbonization.* Nat. Energy, 2020. **5**(9): p. 635-637.

82. Sakakibara, R., et al., *Practical emitters for thermophotovoltaics: a review.* J. Photon Energy, 2019. **9**(3): p. 032713.

83. Burger, T., et al., *Present efficiencies and future opportunities in thermophotovoltaics.* Joule, 2020. **4**(8): p. 1660-1680.

84. Pendry, J.B., *Radiative exchange of heat between nanostructures.* J. Phys-Condens. Mat., 1999. **11**(35): p. 6621-6633.

85. Ilic, O., et al., *Overcoming the black body limit in plasmonic and graphene near-field thermophotovoltaic systems.* Opt. Express, 2012. **20**(10): p. A366-A384.

86. Messina, R. and P. Ben-Abdallah, *Graphene-based photovoltaic cells for near-field thermal energy conversion.* Sci. Rep., 2013. **3**: p. 1383.

87. Svetovoy, V.B. and G. Palasantzas, *Graphene-on-Silicon Near-Field Thermophotovoltaic Cell.* Phys. Rev. Appl., 2014. **2**(3): p. 034006.

88. Hsu, W.C., et al., *Entropic and near-field improvements of thermoradiative cells.* Sci. Rep., 2016. **6**: p. 34837.

89. Karalis, A. and J.D. Joannopoulos, *'Squeezing' near-field thermal emission for ultra-efficient high-power thermophotovoltaic conversion.* Sci. Rep., 2016. **6**: p. 28472.

90. St-Gelais, R., et al., *Hot carrier-based near-field thermophotovoltaic energy conversion.* Acs Nano, 2017. **11**(3): p. 3001-3009.

91. Ganjeh, Y., et al., *A platform to parallelize planar surfaces and control their spatial separation with nanometer resolution.* Review of Scientific Instruments, 2012. **83**(10): p. 105101.

92. Whittaker, D.M. and I.S. Culshaw, *Scattering-matrix treatment of patterned multilayer photonic structures.* Physical Review B, 1999. **60**: p. 2610.

93. Yeh, P., *Optical Waves in Layered Media*. Wiley series in pure and applied optics. 1988, New York: Wiley. x, 406 p.

94. Francoeur, M., M.P. Menguc, and R. Vaillon, *Solution of near-field thermal radiation in one-dimensional layered media using dyadic Green's functions and the scattering matrix method.* Journal of Quantitative Spectroscopy & Radiative Transfer, 2009. **110**(18): p. 2002-2018.

95. Zhu, L. and S. Fan, *Near-complete violation of detailed balance in thermal radiation.* Physical Review B, 2014. **90**: p. 220301.

96. St-Gelais, R., et al., *Near-field radiative heat transfer between parallel structures in the deep subwavelength regime.* Nature Nanotechnology, 2016. **11**(6): p. 515-519.

97. Stoyanov, N.D., et al., *Super low power consumption middle infrared LED-PD optopairs for chemical sensing.* Optical Components and Materials Xi, 2014. **8982**: p. 89821A.

98. Modest, M.F., *Radiative Heat Transfer*. 3rd ed. 2013, Oxford, UK: Academic Press.

99. Lander, J.J. and J. Morrison, *Low voltage electron diffraction study of oxidation and reduction of silicon.* J. Appl. Phys., 1962. **33**(6): p. 2089.

100. Ganjeh, Y., et al., *A platform to parallelize planar surfaces and control their spatial separation with nanometer resolution.* Rev. Sci. Instrum., 2012. **83**(10): p. 105101.

101. Zhu, L., et al., *Near-field photonic cooling through control of the chemical potential of photons.* Nature, 2019. **566**(7743): p. 239-244.

102. Reihani, A., et al., *Quantifying the temperature of heated microdevices using scanning thermal probes.* Appl. Phys. Lett. , 2021. **118**: p. 163102.

103. Whittaker, D.M. and I.S. Culshaw, *Scattering-matrix treatment of patterned multilayer photonic structures.* Phys. Rev. B, 1999. **60**(4): p. 2610-2618.

104. Glassbrenner, C.J. and G.A. Slack, *Thermal conductivity of silicon + germanium from 3 degrees K to melting point.* Phys. Rev., 1964. **134**(4a): p. 1058-1069.

105. Gysin, U., et al., *Temperature dependence of the force sensitivity of silicon cantilevers.* Phys. Rev. B, 2004. **69**(4).

106. Chapman, P.W., et al., *Electrical properties of heavily doped silicon.* J. Appl. Phys., 1963. **34**(11): p. 3291.

107. Chui, B.W., et al., *Intrinsic-carrier thermal runaway in silicon microcantilevers.* Microscale Therm. Eng., 1999. **3**(3): p. 217-228.

108. Adachi, S., *Physical properties of III-V semiconductor compounds : InP, InAs, GaAs, GaP, InGaAs, and InGaAsP. (Wiley, New York, 1992).*

109. *I. P.-T. Institute, NSM archive - Physical properties of semiconductors, 1998; The Ioffe Physical-Technical Institute of the Russian Academy of Sciences, 1998.* http://www.ioffe.ru/SVA/NSM/Semicond.html.

110. Madelung, O., *Semiconductors : data handbook, Edn. 3rd. (Springer, Berlin, 2004).*

111. Pearsall, T.P., *GaInAsP alloy semiconductors. (Wiley, New York, 1982).*

112. Bugajski, M. and W. Lewandowski, *Concentration-dependent absorption and photoluminescence of n-type Inp.* J. Appl. Phys., 1985. **57**(2): p. 521-530.

113. Anderson, D.A., et al., *Compensation in heavily doped n-type Inp and Gaas.* J. Appl. Phys., 1985. **58**(8): p. 3059-3067.

114. Wiley, J.D., *Semiconductors and semimetals, Vol. 10. (eds. R.K. Willardson & A.C. Beer) 91-174 (Elsevier, 1975).*

115. Fu, C.J. and Z.M. Zhang, *Nanoscale radiation heat transfer for silicon at different doping levels.* Int. J. Heat Mass Tran., 2006. **49**(9-10): p. 1703-1718.

116. Adachi, S., *Optical constants of crystalline and amorphous semiconductors: numerical data and graphical information. (Springer US, 1999).*

117. Sinnott, R.K., *Coulson & Richardson's Chemical Engineering (7th ed.), Volume 1b: Heat and Mass Transfer: Fundamentals and Applications.* 2018: p. 3-264.

118. Rinnerbauer, V., et al., *High-temperature stability and selective thermal emission of polycrystalline tantalum photonic crystals.* Opt. Express, 2013. **21**(9): p. 11482-11491.

119. Zhao, B., et al., *Thermophotovoltaic emitters based on a two-dimensional grating/thin-film nanostructure.* Int. J. Heat Mass Tran., 2013. **67**: p. 637-645.

120. Inoue, T., T. Asano, and S. Noda, *Spectral control of near-field thermal radiation via photonic band engineering of two-dimensional photonic crystal slabs.* Opt. Express, 2018. **26**(24): p. 32074-32082.

121. Woolf, D.N., et al., *High-efficiency thermophotovoltaic energy conversion enabled by a metamaterial selective emitter.* Optica, 2018. **5**(2): p. 213-218.

122. Baranov, D.G., et al., *Nanophotonic engineering of far-field thermal emitters.* Nat. Mater., 2019. **18**(9): p. 920-930.

123. Burger, T., et al., *Thin-film architectures with high spectral selectivity for thermophotovoltaic cells.* Acs Photonics, 2018. **5**(7): p. 2748-2754.

124. Hur, S., et al., *Sub-nanowatt resolution direct calorimetry for probing real-time metabolic activity of individual C. elegans worms.* Nature Communications, 2020. **11**(1).

125. Lamprecht, I., *Calorimetry and thermodynamics of living systems.* Thermochimica Acta, 2003. **405**(1): p. 1-13.

126. Wadso, L. and F.G. Galindo, *Isothermal calorimetry for biological applications in food science and technology.* Food Control, 2009. **20**(10): p. 956-961.

127. Maskow, T. and S. Paufler, *What does calorimetry and thermodynamics of living cells tell us?* Methods, 2015. **76**: p. 3-10.

128. DeBerardinis, R.J. and C.B. Thompson, *Cellular Metabolism and Disease: What Do Metabolic Outliers Teach Us?* Cell, 2012. **148**(6): p. 1132-1144.

129. Barzilai, N., et al., *The Critical Role of Metabolic Pathways in Aging.* Diabetes, 2012. **61**(6): p. 1315-1322.

130. Finkel, T., *The metabolic regulation of aging.* Nature Medicine, 2015. **21**(12): p. 1416-1423.

131. Cairns, R.A., I.S. Harris, and T.W. Mak, *Regulation of cancer cell metabolism.* Nature Reviews Cancer, 2011. **11**(2): p. 85-95.

132. Braeckman, B.P., K. Houthoofd, and J.R. Vanfleteren, *Assessing metabolic activity in aging Caenorhabditis elegans: concepts and controversies.* Aging Cell, 2002. **1**(2): p. 82-88.

133. Van Voorhies, W.A., *Metabolism and aging in the nematode Caenorhabditis elegans.* Free Radical Biology and Medicine, 2002. **33**(5): p. 587-596.

134. Houthoofd, K., et al., *DAF-2 pathway mutations and food restriction in aging Caenorhabditis elegans differentially affect metabolism.* Neurobiology of Aging, 2005. **26**(5): p. 689-696.

135. Corsi, A.K., B. Wightman, and M. Chalfie, *A Transparent Window into Biology: A Primer on Caenorhabditis elegans.* Genetics, 2015. **200**(2): p. 387-407.

136. Kaletta, T. and M.O. Hengartner, *Finding function in novel targets: C-elegans as a model organism.* Nature Reviews Drug Discovery, 2006. **5**(5): p. 387-398.

137. Krijgsveld, J., et al., *Metabolic labeling of C-elegans and D-melanogaster for quantitative proteomics.* Nature Biotechnology, 2003. **21**(8): p. 927-931.

138. Houthoofd, K., et al., *Metabolism, physiology and stress defense in three aging Ins/IGF-1 mutants of the nematode Caenorhabditis elegans.* Aging Cell, 2005. **4**(2): p. 87-95.

139. Guarente, L. and C. Kenyon, *Genetic pathways that regulate ageing in model organisms.* Nature, 2000. **408**(6809): p. 255-262.

140. Lapierre, L.R. and M. Hansen, *Lessons from C. elegans: signaling pathways for longevity.* Trends in Endocrinology and Metabolism, 2012. **23**(12): p. 637-644.

141. Uno, M. and E. Nishida, *Lifespan-regulating genes in C. elegans.* Npj Aging and Mechanisms of Disease, 2016. **2**.

142. Kenyon, C., et al., *A C-Elegans Mutant That Lives Twice as Long as Wild-Type.* Nature, 1993. **366**(6454): p. 461-464.

143. Krenger, R., T. Lehnert, and M.A.M. Gijs, *Dynamic microfluidic nanocalorimetry system for measuring Caenorhabditis elegans metabolic heat.* Lab on a Chip, 2018. **18**(11): p. 1641-1651.

144. Inomata, N., M. Toda, and T. Ono, *Highly sensitive thermometer using a vacuum-packed Si resonator in a microfluidic chip for the thermal measurement of single cells.* Lab on a Chip, 2016. **16**(18): p. 3597-3603.

145. Lee, W., et al., *High-sensitivity microfluidic calorimeters for biological and chemical applications.* Proceedings of the National Academy of Sciences of the United States of America, 2009. **106**(36): p. 15225-15230.

146. Tan, S., et al., *Pico-Kelvin thermometry and temperature stabilization using a resonant optical cavity.* Optics Express, 2017. **25**(4): p. 3578-3593.

147. Unni, P.K.M., M.K. Gunasekaran, and A. Kumar, *+/- 30 mu K temperature controller from 25 to 103 degrees C: Study and analysis.* Review of Scientific Instruments, 2003. **74**(1): p. 231-242.

148. Sadat, S., E. Meyhofer, and P. Reddy, *Resistance thermometry-based picowatt-resolution heat-flow calorimeter.* Applied Physics Letters, 2013. **102**(16).

149. Hulme, S.E., et al., *A microfabricated array of clamps for immobilizing and imaging C-elegans.* Lab on a Chip, 2007. **7**(11): p. 1515-1523.

150. Decuyper, C. and J.R. Vanfleteren, *Oxygen-Consumption during Development and Aging of the Nematode Caenorhabditis-Elegans.* Comparative Biochemistry and Physiology a-Physiology, 1982. **73**(2): p. 283-289.

151. Laranjeiro, R., et al., *Single swim sessions in C-elegans induce key features of mammalian exercise.* Bmc Biology, 2017. **15**.

152. West, G.B. and J.H. Brown, *The origin of allometric scaling laws in biology from genomes to ecosystems: towards a quantitative unifying theory of biological structure and organization.* Journal of Experimental Biology, 2005. **208**(9): p. 1575-1592.

153. West, G.B., W.H. Woodruff, and J.H. Brown, *Allometric scaling of metabolic rate from molecules and mitochondria to cells and mammals.* Proceedings of the National Academy of Sciences of the United States of America, 2002. **99**: p. 2473-2478.

154. Klekowski, R.Z., E. Paplinska, and L. Wasilewska, *Oxygen-Consumption by Soil-Inhabiting Nematodes.* Nematologica, 1972. **18**(3): p. 391-403.

155. Fiorino, A., et al., *Parallelized, real-time, metabolic-rate measurements from individual Drosophila.* Scientific Reports, 2018. **8**.

156. Skogestad, S. and C. Grimholt, *The SIMC Method for Smooth PID Controller Tuning.* Pid Control in the Third Millennium: Lessons Learned and New Approaches, 2012: p. 147-175.

157. Moore, B.T., J.M. Jordan, and L.R. Baugh, *WormSizer: High-throughput Analysis of Nematode Size and Shape.* Plos One, 2013. **8**(2).

158. Reina, A., et al., *Shifts in the Distribution of Mass Densities Is a Signature of Caloric Restriction in Caenorhabditis elegans.* Plos One, 2013. **8**(7).

159. Brenner, S., *The genetics of Caenorhabditis elegans.* Genetics, 1974. **77**(1): p. 71-94.